PROCEDURES FOR THE IDENTIFICATION OF COHERENT STRUCTURES IN OSCILLATORY AND PULSATING FLOWS OVER A WAVY BOTTOM

Marc Gasser i Rubinat

A thesis submitted to the faculty of the University of North Carolina at Chapel Hill in partial fulfillment of the requirements for the Master Degree in the Department of Marine Sciences.

Chapel Hill
2007

Approved by

Harvey Seim

Thomas Shay

Alberto Scotti

ABSTRACT

Marc Gasser i Rubinat: PROCEDURES FOR THE IDENTIFICATION OF COHERENT STRUCTURES IN OSCILLATORY AND PULSATING FLOWS OVER A WAVY BOTTOM
(Under the direction of Alberto Scotti)

Oscillatory flows over a wavy bottom play an important role in sediment dynamics, coastal circulation and bottom - water column biogeochemical interactions. The most important process that controls the energy and mass flux in such flows is the generation, advection and dissipation of coherent structures. This thesis gives a working definition of a coherent structure in an instantaneous and averaged flow and compares several identification methods using velocity and pressure fields obtained from computer simulations using a Large Eddy Simulation(LES) numerical scheme. The effectiveness of each identification method is assessed for several flows with different Reynolds number and relevant physical properties of each flow, obtained from the study of such coherent structures, are described.

DEDICATION

This Thesis is dedicated to my parents and my sister (Aquesta Tesi esta dedicada als meus pares i a la meva germana).

ACKNOWLEDGEMENTS

I'd like to thank my fellow graduate students for their extraordinary help and support during the past five years (in no particular order): Andrew Steen, Karen Lloyd, Catherine Edwards, Valerie Winkelman, Laurie Strebble, Tanya Bean, Mark Lever, Greg Dusek, Dr. Melissa Southwell, Elaine Monbureau, Dr. Laura Llapham, Sarah Lee and Holly Nance.

I'd also like to thank Chris Galloway, Jesse Cleary, Sherif Ghobrial and Nadera Malika-Salaam.

Many, many thanks to Mary Campbell.

I'd also like to thank Dr. John Bane and Dr. Conrad Neumann.

Many thanks to Dr. José Luis Pelegrí Llopart.

I am deeply indebted to two very extraordinary persons: Sandi Chapman and Dr. Alfredo López de Aretxabaleta Aguayo.

Last but not least, many thanks to my Thesis' Committee members: Harvey Seim, Thomas Shay and very specially Alberto Scotti.

TABLE OF CONTENTS

LIST OF TABLES

Table

LIST OF FIGURES

CHAPTER 0: INTRODUCTION

In the context of geophysical fluid dynamics, oscillatory flows in a boundary layer have important implications in many ocean processes, such as sediment erosion, transport and deposition, biogeochemical fluxes through the water-sediment interface, bedform morphogenesis and creation of microbiotopes for benthic organisms. The flow dynamics due to the interaction between a wave field and a mean, steady current over a wavy bottom is controlled in great part by the creation, advection and dissipation of coherent structures, flow regions were important physical quantities such as velocity or density have correlation scales larger than the smallest eddies. These coherent structures have a direct impact in processes such as sediment pick up rates due to the generation of strongly localized (in time and space) flow subdomains with high values of velocity perturbations, vorticity and Turbulent Kinetic Energy (TKE).

The purpose of this thesis is to asses the effectiveness of several methods for the identification of such structures in velocity and pressure fields computed using a Large Eddy Simulation (LES) numerical scheme of a pressure driven oscillatory flow over a wavy bottom in a relatively wide range of Reynolds number. I also will describe relevant physical characteristics of these flows elucidated using the spatial and temporal distribution of such structures, and show that they can be used to distinguish between several flow regimes as a function of the Reynolds number.

Chapter one deals with the description of the Large Eddy Simulation (LES) numerical scheme used in the simulations. Chapter two describes the postprocessing subroutines developed by the author and used to transform the output files into data readable by a Computer Fluid Dynamics (CFD) Visualization package called TECPLOT©. Chapter three deals with a brief overview of coherent structures in boundary layer flows and their importance in the Turbulent Kinetic Energy (TKE) generation, advection and dissipation and in mass transport mechanisms. I introduce the concept of a vortex in both

instantaneous and averaged velocity and pressure fields and the methods used to identify coherent structures in Chapter four. In Chapter five I describe the results of the application of these methods to three flows with different Reynolds number. Finally, Chapter six gives a short summary of the most important results and conclusions of this Thesis.

CHAPTER 1: COMPUTATIONAL SETUP

SECTION 1.1: OVERVIEW

In order to study the properties of oscillatory and pulsating flows over a wavy bottom several numerical experiments were performed with different values for the Reynolds number. Of these experiments, three were selected for a detailed analysis using the postprocessing subroutines described below (case Reynolds Number Re=42, Re=150 and Re=210). This Chapter describes the numerical scheme used in the simulations and the flow domain.

SECTION 1.2: DESCRIPTION OF THE NUMERICAL SCHEME AND THE FLOW DOMAIN

A Large Eddy Simulation (LES) numerical scheme was used to calculate the flow properties for this study. LES has been used successfully before for the elucidation of coherent structures, in oceanographic and engineering flows, and there is abundant literature regarding its advantages over other types of numerical schemes (Direct Numerical Simulation - DNS, Unsteady Reynolds Averaged Navier Stokes - URANS, etcetera; see Tseng 2004, Balaras 2001, Piomelli 2000 and 2001, Chang 2004 and undated, Henn 1999, Fede undated, Tseng 2004). LES solves the filtered Navier-Stokes equations:

1.1 $\bar{u}_{i,t}+(\bar{u}_i\bar{u}_j)_{,j}=-\bar{P}_i+\nu\bar{u}_{i,ij}-\tau_{ij,j}$ (overbar indicates an adequate average and comma denotes derivative; ν is the kinematic viscosity) ; and the continuity equation

1.2 $\bar{u}_{i,i}=0$; the Subgrid Scale Stress (SGSS) is defined as

1.3 $\tau_{ij}=\overline{(u_i u_j)}-\bar{u}_i\bar{u}_j$

The SGSS is modeled using a Dynamic Eddy Viscosity Model (Scotti pers. comm.). Eqs. 1.1-1.3 are solved using an Adams-Bashford fractional step method; advective and diffusive terms are treated

explicitly. All spatial derivatives are approximated using second-order central differences. For further details see Chang (undated).

Using the geophysical convention for the reference system, the domain is 0.1 m long (x_1, longitudinal axis), 0.1 m wide (x_2, cross-channel or transversal axis) and 0.055 m high (x_3, vertical axis). The grid used in our simulations is an Arakawa-C (staggered) type with 288 (longitudinal direction) x 64 (cross-channel direction) x 128 (vertical direction) cells. The cell size is constant in the horizontal plane but changes along the vertical to increase the grid resolution towards the upper and lower boundaries (see figure 1.1). Boundary conditions are periodic in the longitudinal and cross-channel directions; at the bottom we enforce a no-slip condition along an immersed boundary defined by a sinusoidal function:

1.4 $$z_{wall} = \alpha_{wall} * [1 + \cos(\frac{2 * \pi * x}{\lambda_{wall}})]$$ z_{wall} being the bottom height,

α_{wall} the ripple's amplitude and λ_{wall} its wavelength.

At the upper surface the flow satisfies a no-slip condition along a plane wall. Although this disposition does not resemble exactly the natural conditions in the ocean (in a wave-driven flow the upper boundary is a free-surface instead of a rigid wall) it was chosen in order to compare the results of the simulations with experiments performed in a flume. Far enough from the upper boundary the properties of the flow do not differ significantly from those of a flow under a free surface for the set of parameters chosen for our simulations (but see further comments about this assumption in Chapter 5).

The flow is driven by an periodic pressure gradient:

1.5 $$p(x,t) = \nabla p_0 + \nabla p_1 e^{(-i \omega_p t)}$$; ∇p_0 and ∇p_1 being respectively the magnitude of the steady and unsteady components of the pressure gradient and $\boldsymbol{T} = 2\frac{\pi}{\omega_p}$ its period. The Reynolds number is defined using an average velocity:

1.6 $$R_e = \frac{U_0 * l_s}{\nu} = \frac{U_0 * \sqrt{(\nu T)}}{\nu}$$; U_0 is

1.7 $$U_0 = \frac{\pi}{T} * \int_0^{\frac{T}{2}} U(t) \partial t$$

and l_s is the thickness of the laminar oscillatory boundary layer (Stokes 1901). The relevant parameters for the different experiments are summarized in Table 1.

CHAPTER 2: DESCRIPTION OF THE POST-PROCESSING SUBROUTINES

SECTION 2.1 : OVERVIEW

The aim of this thesis is to study and identify coherent structures in oscillating and pulsating flows over a wavy bottom using a visualization package named TECPLOT©. Unfortunately, the files generated by the LES code can not be read directly by TECPLOT© so an intermediate step is necessary, namely, the format conversion from the original data from the simulations to a file that can be understood by the visualization program.

The simulation code generates a set of variables (in our case, the complete velocity and pressure fields) from which other quantities useful for the identification of coherent structures can be calculated. Although TECPLOT© has the capability to compute secondary or derived variables from this set, this capability is limited: certain variables, like the second invariant of the velocity gradient tensor, must be calculated by an external program prior to visualization (see reference TECPLOT© for a detailed description of the visualization package). For reasons of convenience and practicality it is also easier to generate other quantities, like averages and statistics, using external programs instead of TECPLOT©.

This section will describe the set of (crude) FORTRAN 95 subroutines I wrote in order to achieve this double goal (format conversion and secondary variables' generation). The choice of programming language was decided based on the desire to complement a similar set written by Dr. Pascal Fede in 2004. In retrospective, this was an unfortunate decision; using a higher-order programming language (like MATLAB©) could have made achieving our goals more efficiently and easy.

SECTION 2.2 : DESCRIPTION OF THE SUBROUTINES

A typical output of the LES code consists in a group of files that constitute a temporal series depicting the flow evolution over a certain time period (t_1,t_2). The number of files M is:

2.1 $M = f_s \cdot c$ f_s being the sampling frequency (in our case, 8 samples per period) and c the number of cycles (for clarity sake, I will define a cycle as the time interval between the initial phase $\Phi_0 = 0$ and the final phase $\Phi_0 + T$, T being the characteristic forcing period). Thus, each consecutive file

2.2 FILE_NUMBER = 1, 2, 3, ..., 7, 8, ..., M-1, M ; corresponds with a time TLEVEL

$TLEVEL = t_0+\Phi_0, t_0+\Phi_1, t_0+\Phi_2, ..., t_0+\Phi_7, t_0+T, ..., t_0+ (c-1)T + \Phi_7, t_0+ (c-1)T + T$

$TLEVEL = t_0, t_0+\Phi_1, t_0+\Phi_2, ..., t_0+\Phi_7, t_0+T, ..., t_0+ (c-1)T + \Phi_7, t_0+ c.T$

$$\phi_0 = 0 \,;\, \phi_1 = \frac{T}{f_s} \,;\, \phi_2 = \frac{2T}{f_s} \,;\, \ldots \,;\, \phi_7 = \frac{7T}{f_s}$$

For this study I have chosen c = 10 cycles, M = 80 files. Each file contains the full (3D) instantaneous velocity [pressure] field for a given time (TLEVEL). The velocity [pressure] fields are written in the format (using FORTRAN-like pseudocode):

```
do k=1,NZ
   do n=1,3 [n=1,1]
      do j=1,NY
         do i=1,NX
            u_n(i,j,k,TLEVEL) [ p_n(i,j,k,TLEVEL)]
         end do
      end do
    end do
end do
```

NX, NY, NZ being the number of cells in the longitudinal, cross-channel and vertical direction respectively and n the number of components for each variable (3 for the velocity vector, 1 for pressure).

After running a simulation the postprocessing subroutines read these files and calculate the variables listed in Table 2. The first variable computed by the subroutines is the instantaneous cross-channel average velocity [pressure], defined as:

2.3 $$\overline{u}_{i,inst}(x_1, x_3, t) = \frac{1}{NY}\sum_{1}^{NY} u_i(x_1, x_2, x_3, t)$$ (the equation for pressure is homologous)

Notice that the instantaneous cross-channel average for a given time is calculated using the velocity [pressure] at that particular time (there is no further averaging either in time or phase). The instantaneous perturbation velocity [pressure] is then calculated:

2.4 $$u'_{i,inst}(x_1, x_2, x_3, t) = u_{i,inst}(x_1, x_2, x_3, t) - \overline{u}_{i,inst}(x_1, x_3, t)$$

By definition, the cross-channel average of this variable is zero. All the other variables (Turbulent Kinetic Energy – TKE -, vorticity, pressure gradient, etcetera) are subsequently computed using the perturbation velocity [pressure]. All the derivatives are calculated using a second-order centered differences scheme.

It is also possible to obtain phase-averaged quantities, which are useful in assessing the mean flow characteristics during a "typical" cycle. Thus we define a phase-averaged variable (for example, phase-averaged pressure) as:

2.5
$$\overline{p}(\boldsymbol{x}, \phi_k) = p(\boldsymbol{x}, t=\phi_k) + p(\boldsymbol{x}, t=\phi_k + T) + p(\boldsymbol{x}, t=\phi_k + 2\mathrm{T}) + ... + p(\boldsymbol{x}, t=\phi_k + (c-1)T) + p(\boldsymbol{x}, t=\phi_k + c.T)$$

$$\overline{p}(\boldsymbol{x}, \phi_k) = \sum_{m=0}^{c-1} p(\boldsymbol{x}, \phi_k + m.T)$$ **x =** $x_1, x_2 x_3$, Φ being the phase and c the number of cycles.

Once the variables are calculated the postprocessing code outputs three sets of files: one containing the full 3-D variables' field (usually named "RE#_3DFIELD_**N**.DAT", **N** being a consecutive number); a second containing the average of each variable in the cross-channel direction (usually named "RE#_2DFIELD_**N**.DAT") and a third file containing the average of each variable in the flow domain (excluding the space occupied by the ripples):

2.6 $$\overline{var} = \frac{1}{L_1}\frac{1}{L_2}\sum_{i=1}^{NX}\sum_{j=1}^{NY}\left(\frac{1}{L_3}\sum_{k=k_{bottom}}^{NZ} var * \Delta x_1 \Delta x_2 \Delta x_3\right)$$ *var* being any variable and L_1,

L_2, $L_3(x_1)$, the length, width and depth of the channel ("TKE_AND_VEL_VS_PHASE.DAT").All the files are written in a TECPLOT© compatible format (again, expressed as FORTRAN pseudo-code):

TECPLOT HEADER (Contains information for TECPLOT©)

```
do k=1,NZ
      do j=1,NY
         do i=1,NX
         xn (n=1:3), list of variables
         end do
      end do
 end do
```

(Full 3-D output)

TECPLOT HEADER (Contains information for TECPLOT©)

```
do k=1,NZ
         do i=1,NX
         xn (n=1,3) , list of variables
         end do
 end do
```

(Output averaged in the cross-channel direction)

The value of the Cartesian coordinates x_i is addimensionalized using the domain length.

Once the raw files have been processed, a program called PREPLOT© is used to transform the ASCII files (extension *.dat or *.DAT) generated by the FORTRAN subroutines into binary files (extension *.plt), which have the advantage of occupying less space. This is done automatically by executing a UNIX script called *scr_preplot* also generated by the subroutines (once transformed the ASCII files into TECPLOT© files, *scr_preplot* erases the files with extension *.dat .It is advisable to save the ASCII files before executing *scr_preplot*).

The actual plots can be created either manually (a tedious process if involves more than a few files, although some times unavoidable) or using a batch processing tool called a "macro".

Thus, a typical post-processing sequence would be:

- Decide if we want a time series or a phase average from our original output files
- Compile and run the post-processing code
- Check the ASCII files for errors and save the *.dat files
- Run the script *scr_preplot*
- Run the macros that generate the desired plots

CHAPTER 3: DEFINITION OF COHERENT STRUCTURES

This Chapter provides a brief introduction to the definition and description of coherent structures in boundary layer flows. This topic has been the subject of much attention and a fair number of literature due to its importance in the context of turbulent flows, so in the interest of brevity I will give just a general idea of the most important concepts and remit the interested reader to the relevant references for the necessary details.

For the purpose of this study I will define a coherent structure as a flow region over which one or more fundamental variables (velocity, density, energy, etcetera) has a significant correlation with itself or with other variables over a range of space and/or time significantly larger than the smallest local scales of the flow (Robinson 1991). Although this definition does not require any kind of vortical motion, in practice most coherent structures do posses a certain degree of rotation.

Coherent structures have been observed in a large variety of experiments and simulations of geophysical and engineering flows (Carlier 2005, Tufo 1999, Blondeaux 2004, Cantwell 1981, Chang undated, Marchioli 2006, Nakagawa 2003, Robinson 1991, Scotti 2001, Tseng 2004). Their importance lays in several factors:

- In many flows, they control the generation and dissipation of turbulent kinetic energy. The early models of TKE transfer in turbulent flows assume a direct energy transfer from the larger scales (large, energy containing, eddies)to the smallest wavelengths (Kolmogorov scales). The formation of coherent structures introduces an additional step, transferring energy from small scales (infinitesimal perturbations) to the intermediate scales characteristic of such structures (Robinson 1991, Natrajan 2006)

- The magnitude of the perturbations from the mean and their generation in a turbulent flow is

not constant with time, but changes in a quasiperiodic fashion. This so called intermittency problem has been related to the generation and evolution of coherent structures (Robinson 1991).

- In a more practical way, coherent structures introduce inhomogeneities in the spatial and temporal distribution of Reynolds stresses and perturbation velocity correlations. It has been suggested that this variability has a direct impact in the geochemical fluxes in the interface between sediment and water column (and between air and water in the ocean surface). Bottom stress controls the sediment uptake in sandy environments; vortical structures can increase the time spent by sand grains in the water column, with the corresponding change in erosive, transport and deposition fluxes (an important consideration in studies of coastal and beach environments, with engineering applications such as beach nourishment, channel dredging, navigational hazards, etcetera) (Dronkers 2005).

Coherent structures are generated by instabilities in the turbulent flow (either primary or secondary) such as shear instabilities, Görtler instabilities (Reed 1989, Swearingen 1987), perturbations of wakes and separation layers (Delery 2001), etcetera. Such structures usually assume the shape of rolls or filaments, which tend to interact between themselves in complex ways. Some examples of structures commonly observed in sheared flows are:

- Sweeps and bursts: sweeps are structures that carry fluid with high momentum downwards from the outer zone to the viscous/buffer region ($u'_1>0$, $u'_3<0$), while bursts transfer low-momentum fluid upwards from the bottom ($u'_1<0$, $u'_3>0$). They act as an enhanced momentum and mass diffusion coefficient.

- Low velocity streaks are longitudinally oriented, cigar-shaped structures possessing a lower velocity than their surrounding fluid. They seem to be related to flow patterns in the inner side of counter-rotating vortices, although several other mechanisms have been suggested (Chernyshenko 2005, Jimenez 1988).

- Horseshoes, arches, hairpins and lambda vortices are filament-like structures generated by a secondary instability in cross-channel rolls. They are lifted from the bottom due to the interaction between their own vorticity and the vertical velocity gradient in the mean flow; the same gradient creates a stretching that can break the hairpin into separate filaments (sometimes called canes) which

then dissipate into the background flow (see figure 3.1 ; Robinson 1991).

CHAPTER 4: VORTEX IDENTIFICATION METHODS

SECTION 4.1: OVERVIEW

This chapter will provide a description of several vortex identification methods that can be used in the elucidation of coherent structures in oscillatory flows over ripples. It is not intended by any means as an exhaustive enumeration but just as a review of the multiple approaches that can be used in order to tackle this problem, and a discussion of their advantages and disadvantages. Only a few of those procedures were actually used by the author in the study of the LES simulations, but I think it is useful to provide the reader with at least an introduction to the methodologies considered, and their advantages and disadvantages, in order to better understand why and when those criteria can be applied with confidence.

Section 4.2 provides the reader with a working definition of vortices in the context of instantaneous and averaged fields. Section 4.3 is an enumeration of the different available methods. Section 4.4 describes the application of the velocity field and the streamlines to the problem of vortex identification. Section 4.5 describes winding angle and quadrant methods. Section 4.6 deals with vorticity, helicity density and relative helicity. Section 4.7 is a summary of the pressure minimum criterion and, finally, the Q criterion will be dealt with in Section 4.8.

SECTION 4.2: DEFINITION OF VORTICES AND COHERENT STRUCTURES IN INSTANTANEOUS AND TIME-AVERAGED FIELDS

The concept of vorticity and vortex is very useful in the context of turbulent motion. The properties of turbulent shear flows are dominated by the behavior of spatially coherent vortical motions called coherent structures and it has been hypothesized that turbulence itself can be adequately described in

a framework of interconnected vortex filaments (Jeong 1995). Unfortunately, one major obstacle for the understanding of turbulent processes is the lack of an accepted definition of what constitutes a vortex although there is a certain consensus about the important properties that the concept should include. These are the following:

- From a kinematic point of view, in a vortex material particles of the fluid rotate around a common center or core (Jeong 1995).

- The structure has net vorticity (thus excluding potential – irrotational - vortices); the definition of a vortex should be Galilean invariant, meaning that it remains unchanged under transformations of the form:

4.1 $\boldsymbol{y} = \boldsymbol{Q}\boldsymbol{x} + \boldsymbol{a}\,t$ where **Q** is an orthogonal tensor and **a** is a constant velocity vector (Jeong 1995 ; Haller 2005 in his attempt to improve upon Jeong's definition proposes a stronger condition called objectivity, defined as the invariance under coordinate changes of the form:

4.2 $\boldsymbol{y} = \boldsymbol{Q}(t)\boldsymbol{x} + \boldsymbol{b}(t)$ where **Q**(t) is a time-dependent orthogonal tensor and **b**(t) is a time-dependent translation vector).

- The particle rotation implies the presence of a centrifugal force that must be balanced against either a pressure gradient, a friction force, a change in the flow velocity or a combination of these factors. If the temporal scale of the motion is large and the effects of friction are small enough the core of a vortex can be characterized by a local minimum in the pressure field (Jeong 1995).

Many criteria have been postulated that satisfy one or more of these properties (Banks undated, Dubieff 2000, Guo 2004, Jeong 1995, Jiang undated, Moffat 1992, Stegmaier 2005, Tufo 1999). The applicability of a given criterion to a particular case depends on the approach taken in the identification scheme: either kinematic (with a focus in the description of the motion without considering the forces that act on the fluid particles) or dynamic (which concerns itself with those forces) and, of course, with the specific characteristics of the process. (For a more detailed discussion on the properties of a vortex see Jeong 1995 and Haller 2005).

Until now, we have defined a vortex in the context of an instantaneous velocity field, with the implication

that actual fluid particles rotate around a core. But from a statistical point of view no scientific and reliable inferences about a certain phenomenon can be made from just one experimental realization. Statistical certainty demands a set of experiments, under similar enough conditions and parameters, in order to extract from said set the properties that characterize that particular kind of fluid motion. Thus we define an ensemble average as the mean of a series of realizations of a given flow, undertaken under conditions that do not differ enough as to change significantly the results of such experiments (Kundu 1990).

Ensemble averages are of course a physical utopia that can be extremely hard to achieve in the real world, specially in observational oceanography where the operational and logistic difficulties and the rarity of some phenomena make this scientific ideal many times an unattainable goal. Even in the case of computer simulations running multiple iterations of a single experiment can be very expensive and time consuming. I will consider then, for the purpose of this study, a phase average (defined elsewhere in this document) as a reasonable proxy under the assumption that the flow is ergodic in the sense of Blackman 1959 (namely, that a short sample is representative of the whole process).

The extension of the definition of a vortex from the instantaneous case to the averaged flow is not straightforward and we must proceed with caution. Two ways are open in front of us: the first one is to try to relate the characteristics of the averaged flow to the structures from which they originate as observed in the instantaneous velocity field. Incidentally this is the way Leonardo da Vinci identified coherent structures in a river flow as described by Holmes 1996 and Marani 2003. In his observations of water moving around an obstacle, Leonardo realized that certain discrete vortices are consistently located roughly in the same place and have approximately the same size, and inferred that the motion can be decomposed into a mean component and a series of “undulations” (coherent structures). The disadvantage inherent in this approach is that it defeats the purpose of an average, namely, obtaining a characterization of the flow properties from a sum of its realizations, not from the detailed study of each and single one of a series of snapshots .

The second way is to compute a mean flow (using a spatial average, a time average or a combination

of both) and then define a coherent structure as a subdomain of the averaged flow which partakes from the characteristics ascribed to a vortical structure in the non-averaged case (namely, a region in the domain where the average velocity, pressure, etcetera, correlate at a larger scale than the smallest eddies in the flow). In the context of a vortical description of a turbulent flow then we can expect that the attributes of coherent structures in non-averaged flows (high vorticity, rotation around a core, pressure minima) describe also adequately these structures in the averaged case. Notice that the definition of coherent structures in the averaged case is fundamentally different from that in the non-averaged case. In the latter, vortices are constituted by real fluid particles with a rotational motion while in the former the structures are born from the averaged flow characteristics, implying larger time and space correlation scales. The pitfall in this approach is that we could fall into the danger of identifying as vortices structures born out of the averaging operation which bear distant or no relation with the actual physical processes happening in the flow, or that real, physical vortices will be obscured or even eliminated in the mean variable field. Both approaches have their merits and drawbacks and I will use one or the other depending on the particular problem we are faced with.

In order to provide a clarifying example (although using a spatial, not temporal, average), consider a field of longitudinally-oriented counter-rotating vortices. It is obvious that we can not use, for example, the cross-channel average of the longitudinal component of the vorticity to identify these particular vortices in a channel cross section, although this quantity is a good descriptor in a three-dimensional instantaneous field. In the other hand, intrinsically positive quantities such as vorticity magnitude are immune to this particular kind of problem. Of course, more subtle problems arise in the process of averaging operations, many of which have no obvious solution and compromises must be made.

SECTION 4.3: CRITERIA FOR DETECTION AND QUANTIFICATION OF VORTICAL COHERENT STRUCTURES

As explained above, the lack of an accepted definition of a vortex translates in a multitude of criteria developed to detect and quantify its existence. Thus, the choice of method or methods we will use to

detect coherent structures is closely related to two considerations: first, how much operator input we want or we are able to provide and, second, the intrinsic properties of the given flow. This section will provide a general overview of several methods currently used in the elucidation of coherent structures, namely:

- Methods using the velocity field and streamlines
- Winding angle and quadrant methods
- Vorticity and vorticity magnitude methods
- Helicity density and Relative Helicity
- Pressure minima
- Eigenvalues of the velocity gradient tensor: Q criterion

SECTION 4.4 VELOCITY FIELD AND STREAMLINES METHODS

A simple, kinematic approach to vortex detection is the study of the actual velocity field (either plotting the velocity vector or using streamlines) in order to identify visually the regions where the flow has a circular pattern. This method has a long tradition, especially in the field of experimental hydro- and aero-dynamics, and this is the reason for the existence of an abundant literature on the subject (for a discussion and many illustrations of the use of streamlines and streaklines, see Batchelor 1967 or Dyke 1982). It has the advantage of being fairly intuitive and it can be very useful in moderately complex 2D flows, or if we are concerned with averaged quantities; it is a very effective way of visualizing a recirculation zone. In 3D flows its usefulness is very limited except in the simplest motions. A further disadvantage of this method is that it is not Galilean invariant, as can be readily seen in figure 4.2, a-b.

SECTION 4.5 WINDING ANGLE AND QUADRANT METHODS

These are intrinsically kinematic methods that focus in the circular motion of the fluid particles in a vortex and, as is the case with streamlines, do not fulfill the condition of being Galilean invariant. The first method asks for two conditions to be satisfied:

- The winding angle of the streamlines in a vortical structure must have a value close to 2π.

- The distance between the projection of the initial and the ending points of the streamlines on a 2-D surface normal to the vortex core should be small (Guo 2004).

A related criterion is the quadrant or cross method. This method divides the plane normal to the core into four (or more) sections with the origin located in the vortex center. If the origin is indeed a vortex core, the circular pattern of the streamlines implies that they will cross the quadrants' axes in a certain order.

Notice that these methods are based in the presumption that fluid particles surrounding a vortex core undergo almost one complete revolution in the time scale characteristic of the motion. A vortex with a rotation period longer than the advective time scale of the flow, or that it is being stretched by a shear motion, will not be detected. These methods are also unable to detect structures undergoing pairing or breakdown processes, and have also the disadvantage of depending upon a correct projection of the three-dimensional streamlines into a plane normal to the suspected vortex core (Jeong 1995).

SECTION 4.6: VORTICITY, HELICITY DENSITY AND RELATIVE HELICITY

The definition of a vortex, as stated by Jeong 1995, explicitly demands the existence of net vorticity (excluding potential or irrotational vortices). This is a necessary but not sufficient condition: for example, the boundary layer over an infinite plate (Blasius flow) has net vorticity but no vortices; thus caution must be exerted using vorticity as an indicator for the presence of coherent structures.

Vorticity is defined as the antisymmetric part of the velocity gradient tensor:

4.3 $\omega_i = \varepsilon_{ijk}(u_k)_j$ ε_{ijk} being the permutation operator

ε_{ijk} = 0, if any two of i,j,k are the same

1, if ijk is an even permutation of 1,2,3

-1, if ijk is an odd permutation of 1,2,3 (Aris 1962)

It is a measure of the average rotation rate of a fluid particle (Kundu 1990) and satisfies the condition of

Galilean invariance.

A related flow property is the helicity density which is a pseudo scalar (meaning that it changes sign under parity transformation - a change in the coordinate system defined as a mirror reflection of the axis):

4.4 $h = u_i \omega_i$

It measures how much the fluid swirls or corkscrews in a helicoidal fashion. If we integrate the helicity density over a domain D in a three dimensional Euclidean space we obtain the helicity:

4.5 $H = \int_D u_i \omega_i dV$

An important property of helicity is that it is a conserved quantity if the evolution of the flow is governed by the Euler equations (a condition not satisfied by boundary layer flows due to the effects of viscous stress; for more details see Moffatt 1992).

Another related flow property is the relative helicity density defined as:

4.6 $$h_{rel} = \frac{(u_i \omega_i)}{(|\boldsymbol{u}| * |\boldsymbol{\omega}|)}$$

The relative helicity density is the cosine of the angle between the velocity vector and the vorticity. Helicity and relative helicity could be useful in the elucidation of vortices with a strong advective component in the direction parallel to their axis. In the other hand, one disadvantage of both helicity density and relative helicity density is the inability to distinguish between a slow moving flow with strong rotational component and a fast moving fluid with weak rotation.

The fact that relative helicity density provides only the angle between a vortex and the flow but does not measure its strength also works against its use for identification purposes, as it can be seen in Figure 4.5 b and Figure 4.6 b. The relative helicity density field is unable to distinguish between the relatively strong, slowly advected, vortices at the bottom and the weaker vortices in the upper, faster zone of the domain. Thus in this particular case its usefulness as a vortex idertification tool it is quite limited.

A problem that arises with vorticity and vorticity-related quantities as pointed out in Jeong 1995 and Haller 2005 is that in many cases background vorticity obscures the presence of smaller scale vortices in a flow, a concern which strongly applies in our case. A possible way of removing this undesired background is to define a de-meaned velocity field u'_i (and analogously a de-meaned pressure field p') by substracting the cross-channel velocity (pressure) average from the original field:

4.7 $u'_i = u_i - \overline{u_i}$; $\overline{u_i}$ defined as $\overline{u_i}(x_1, x_3, t) = \frac{1}{L_2} \int_{x_2=y_0}^{L_2} u(x_i, t)\, \partial x_2$

4.8 $p' = p - \overline{p}$; $\overline{p}$ defined as $\overline{p}(x_1, x_3, t) = \frac{1}{L_2} \int_{x_2=y_0}^{L_2} p(x_i, t)\, \partial x_2$ L_2 being the channel width. The effects of this operation are depicted in Figures 4.3, 4.4, 4.5 and 4.6 for the case of a shear flow over a wavy bottom with constant speed. The first two plots show the three components of the vorticity and the vorticity magnitude, while the following plots show the helicity density and relative helicity density fields for the same flow.

With reference to the vorticity, the biggest differences arise in the cross-channel component and the vorticity magnitude. The delicate filaments noticeable in the de-meaned fields are obscured in the original flow by the signal from the strong vertical velocity shear. Less affected is the vertical component although the simple de-meaning is able to extract more detail than the original data. Finally, the longitudinal component shows few (if any) differences.

A similar behavior is observed in the second set of figures. The number of structures shown in the de-meaned helicity field is greater than in the original data and their shape is more elongated. Finally, although the change is difficult to perceive, a similar tendency is observed in the relative helicity field.

SECTION 4.7 LOCAL PRESSURE MINIMA

Assuming a cyclostrophic equilibrium, in a rotational or swirling motion the centrifugal force due to the curvature of the streamlines must be balanced by a pressure gradient. The vortex axis or core then will

be characterized by a pressure minimum surrounded by a region with a relatively strong pressure gradient which can be used as identification methods. This minimum can exist in all three directions or only in a plane normal to the vortex axis (as for example is the case of the Burgers vortex) (Jeong 1995). Thus we can define the pressure gradient magnitude along the three spatial axes:

4.9 $$|\nabla \boldsymbol{p}| = \sqrt{\sum_{i=1}^{3} (\nabla p)_i^2}$$ or we can define the pressure gradient only in a plane normal to the longitudinal direction x_1:

4.10 $$|\nabla \boldsymbol{p}|_{cross} = \sqrt{\sum_{i=2}^{3} (\nabla p)_i^2}$$ which I will call cross-channel pressure gradient magnitude.

Of course a strict cyclostrophyc equilibrium is only possible in a steady, inviscid planar flow (incidentally, not the case of pulsating boundary layer flows over ripples, which violates all of the three restrictions) and the effectiveness of this elucidation method will be inversely proportional to the degree the flow departs from these three conditions.

We must also take into account the fact that vortices can exist as a result of processes not involving pressure effects whatsoever. A classical example is the von Kármán viscous pump in which a vortex is generated by a rotating disc immersed in a fluid as a result of a balance between viscous and centrifugal forces, the pressure variation in the radial direction being identically zero.

An example of the results using this method is shown in figure 4.2 e-f. Pressure contours are plotted as black lines in the background of plots c-f.

SECTION 4.8: Q CRITERION

This criterion is named after the second invariant of the velocity gradient tensor:

4.9 $$\boldsymbol{Q} = \frac{1}{2}(\Omega_{ij}\Omega_{ij} - S_{ij}S_{ij})$$

where $\Omega_{ij} = \frac{(u_{i,j} - u_{j,i})}{2}$ and $S_{ij} = \frac{(u_{i,j} + u_{j,i})}{2}$ are respectively its antisymmetric and symmetric parts. Thus in regions where the rotation rate, given by Ω_{ij}, overcomes the strain rate, given by S_{ij}, $\boldsymbol{Q}$ has a positive value. The relation between $\boldsymbol{Q}$, vorticity magnitude and pressure is:

4.10 $$\boldsymbol{Q} = \frac{1}{4}(|\boldsymbol{\omega}|^2 - 2S_{ij}S_{ij}) = \frac{1}{(2\rho)}p_{,ii}$$

The value of $\boldsymbol{Q}$ is then proportional to the Laplacian of pressure. Although in practice it is usually the case, notice that if inside a given domain $\boldsymbol{Q}$ is positive that does not necessarily imply a local minimum for pressure inside the domain (as a consequence of the minimum principle, the lowest pressure values could be located in the border); there is no exact correspondence between the $\boldsymbol{Q}$ criterion and the pressure criterion (for a more detailed discussion see Dubieff 2000, Jeong 1995). The $\boldsymbol{Q}$ criterion is Galilean invariant but some caveats must be considered before using this method to identify vortices. First and more important we must decide what value to use as a threshold. If the value is too small, any location where even a feeble amount of rotation can overcome and even smaller strain will be considered a potential vortex and the spurious signals could obscure the physically relevant structures; in the other hand, if the value is too restrictive we risk missing those same relevant structures.

Another problem is that $\boldsymbol{Q}$ is not an absolute measure of the vortex strength, but of the strength in relation to the flow strain. Thus a strong vortical structure undergoing stretching can give a signal equivalent to a weaker vortex that does not suffer deformation. This particular drawback can be at least

partially overcome if we know roughly where the regions with strong shear are located, although in rapidly evolving flows this can prove a difficult task.

CHAPTER 5: ELUCIDATION OF COHERENT STRUCTURES IN PULSATING AND OSCILLATORY FLOWS

SECTION 5.1: VERTICAL GRADIENT SIGNAL IN A BOUNDARY LAYER FLOW

As explained above (see Chapter 3), if we are interested in the smaller scales of the process as opposed to the mean background flow it is desirable to separate this long wavelength signal from the original field. Considering the system geometry and the fact that our flow is characterized by a strong vertical shear a natural way to accomplish this is to substract the cross-channel mean from the three-dimensional velocity (pressure) field and define a new perturbation variable:

5.1 $$v_i(x_1, x_2, x_3, t) = v'_i(x_1, x_2, x_3, t) + \bar{v}_i(x_1, x_3, t)$$

$$p(x_1, x_2, x_3, t) = p'(x_1, x_2, x_3, t) + \bar{p}(x_1, x_3, t)$$ where the bar denotes a variable averaged in the cross-channel (x_2) direction and the prime a de-averaged velocity. But which cross-channel average?. Two immediate choices are available: either the phase average of the cross-channel mean:

5.2 $$\bar{v}_i(x_1, x_3, \phi_k) = \sum_{n=0}^{c-1} \left(\frac{1}{L_2} \right) \int_{x_2=0}^{L_2} v_i(x_1, x_2, x_3, t_0 + \phi_k + nT) \partial x_2$$

(and an analogous expression for pressure), Φ_k being the phase, c the number of cycles, L_2 the channel width and T the period; *k* in this formula does not relate to the index in the vertical direction. Notice that this average is a function of the phase but not of time. Or the second choice, the instantaneous cross-channel mean:

5.3 $$\bar{v}_i(x_1, x_3, t) = \left(\frac{1}{L_2} \right) \int_{x_2=0}^{L_2} v_i(x_1, x_2, x_3, t) \partial x_2$$ which is a function of time.

Under our ergodicity assumption, both averages give equivalent results. If the flow is not ergodic, we can define a (small) scale $v(x_i, t) - \bar{v}(x_1, x_3, \phi_k) = O(\Psi_s)$ and a (large) scale

$v(x_i,t)-\bar{v}(x_{1,}x_3)=O(\Psi_l)$ (same with pressure); then the second average will give the variability of the processes at small scale Ψ_s while the first average will give the variability of the interactions between the processes at small and large scale.

Due to the fact that the results obtained using the instantaneous cross-channel average have a simpler physical interpretation than those using the phase average of the cross-channel mean I have decided to use always the first average to calculate the value of the perturbation velocity and pressure for the purposes of this study.

SECTION 5.2 : THE EFFECT OF SPATIAL AND TEMPORAL RESOLUTION IN THE IDENTIFICATION OF COHERENT STRUCTURES

The characteristic time scale of turbulent fluctuations in a steady flow over a flat bottom is a function of the flow characteristics such as TKE, energy dissipation rate ε and local velocity gradient (Chen 2003). In an oscillatory flow, additional time and space scales appear as the oscillation period T and the ripples' characteristic length scale λ which affect the evolution and spatial distribution of such structures.

Let us assume that the smallest dimension in a vortex is given by a certain wavelength λ_c , and that we can define a characteristic time scale T_c (which can be understood either as an advective or local period, borrowing terminology from the Navier-Stokes equations). Clearly, in order to detect the vortical signal the grid resolution must be greater than the length scale λ_c :

5.4 $\lambda_c > \lambda_{crit} = 2\Delta l_{grid}$ where l_{grid} is the maximum cell size and λ_{crit} represents the threshold value; and in a similar way:

5.5 $f_s > f_{crit} = \frac{1}{(2T_c)}$ f_s being our sampling frequency (Blackman 1959)

In practice, some of the mathematical operations in the postprocessing code act as a *de facto* low pass filter in space, so it is advisable to use an even smaller λ_{crit} (say by a factor of 2 or 4).

The difficulty in an unsteady case lays thus not only in verifying this condition for the intrinsic time and space scales of the structures, but we must also take into account that their generation, advection and dissipation is constricted by the external time and space scales of the mean flow. This problem will be discussed in more detail for each particular case.

SECTION 5.3: TEST CASES FOR THE ELUCIDATION OF COHERENT STRUCTURES

Although the topic of this thesis is vortex identification procedures, it is helpful to acquire at least a basic knowledge of the evolution of the flows where these schemes are being applied. As described in more detail in Chapter 3, all of these methods work under assumptions related to the characteristics of the structures under investigation; the effectiveness of the criteria is a function of the motion unsteadiness, mean flow deviation from planarity, spatial and temporal distribution of high shear zones, etcetera. Knowing when and where the flow departs from these assumptions is helpful in the assessment of the applicability of every method to a particular problem and allow us to predict, not only what works and what does not, but why, when and where a scheme works or does not.

The three flows considered are pressure-driven boundary layer flows in a channel over a wavy bottom. The flow parameters are described elsewhere in this document (see Chapter 1 and table 1). Both cases R_e=42 and R_e=210 are pulsating flows with a period of T_{42} = 1/3 s and T_{210} = 8 s respectively (pulsating meaning that the average of the longitudinal velocity u_1 over the flow domain, although changing with time, is always positive) while the case R_e=150 is an oscillating flow with a period T_{150} = 1 s (oscillating implies a reversal of the averaged longitudinal velocity). The cases discussed here were chosen in order to assess the detection of structures in flows with different Reynolds number.

SECTION 5.4 : FLOW DESCRIPTION, CASE REYNOLDS 42

The evolution of the phase-averaged longitudinal velocity u_i and the similarly averaged TKE for case R_e = 42 (Re 42 for short) is depicted in Figures 5.1-5.2 . The velocity variation is a sinusoidal curve with

amplitude 0.086 m s^{-1} and period T_{42} = 1/3 s; it reaches its peak at phase t=0 s and its minimum value at t=0.17 s. Velocity has been adimensionalized using the friction velocity:

5.1 $U^+ = \frac{v}{u_f}$ u_f being the friction velocity $u_f = \sqrt{\left(\frac{\tau_0}{\rho}\right)}$ and τ_0 the shear stress at the bottom. Similarly, the vertical dimension is given in terms of wall units:

5.2 $y^+ = u_f \frac{x_3}{\nu}$ ν being the kinematic viscosity (Kundu 1990).

As shown in Figure 5.1-5.2 the vertical shear in the outer region of the boundary layer (roughly from y^+=30 to y^+= 100) remains approximately constant with time. The shear in the viscous and buffer layers * is not constant: its (positive) value decreases from the maximum at phase t=0 s (which corresponds with the velocity maximum) to t=0.083 s. At some point between t=0.083 s and 0.125 s past the middle point in the deceleration stage the shear changes its sign and increases its magnitude until reaching a maximum at t=0.17 s. A further sign reversal (this time from negative to positive) happens between t=0.21 s and 0.25 s at the beginning of the acceleration stage, shortly after the velocity minimum; afterwards the shear grows again to achieve its peak at phase t=0 s.

The phase- and cross-channel-averaged longitudinal velocity field U_1 is depicted in Figure 5.3. Notice how mass conservation lifts the isotachs (equal velocity contours) over the troughs. The velocity variations in the outer region (upper half of the domain) are of the order of 0.15 ms^{-1} which is half the magnitude of the velocity change in regions near the bottom ($\Delta U_1 \sim 0.3 ms^{-1}$), specifically those on top of the crests. The downstream side of the crests is also a zone with high vertical shear from the phase t=0.29 s to t=0.042 s, while strong vertical gradients are apparent along most part of the ripples from t=0.125 to t=0.17 s; at t=0.208 s these are concentrated on the crests.

Directing our attention to the phase- and cross-channel-averaged pressure and streamlines field, we can infer from figure 5.4 the existence of two stages in the flow evolution from a kinematic point of

* Due to the way the average has been defined and the boundary geometry, we can not talk strictly about a viscous sublayer and a buffer zone in the vertical velocity profiles. In that context I will employ those terms as a description of the regions in the profile that resemble the viscous sublayer and the buffer zone in the corresponding profiles for a boundary layer flow over a flat surface.

view. The first stage spans from phase t=0.250 s to t=0 s (the end of the acceleration phase as shown in figure 5.1), roughly 40% of the flow period, and is characterized by the fact that the streamlines follow the bottom profile. The second stage lasts from t=0.042 s to t=0.21 s. At the beginning of this second stage the flow deceleration induces a recirculation zone in the downstream side of the ripples (t=0.042-0.083). Just before the velocity minimum the recirculation vortex deattaches from the bottom and a second vortex is created above the troughs. The lifting process reaches its maximum height at t=0.167 s and a strong recirculation flow develops immediately above the bottom; after that, the mean flow acceleration "pushes down" the vortices until at t=0.25 s those have completely disappeared.The effect of the mean flow vortices is a local increase of the vertical shear in certain zones of the ripples, specially on the recirculation zone and in the region near the crests from t=0.125 s to t=0.208 s. This shear generation will be noticed in the second invariant of the velocity gradient field (see further comments below). These vortices are accompanied by saddle points (critical points that are stable in one direction and unstable in the other) which indicate regions where the flow suffers stretching and compression, processes that can hinder the detection of coherent structures.

Another important flow characteristic which I would like to address is the evolution of the phase-averaged TKE, as depicted in figure 5.1, c-d. The variation of the TKE in this flow is very small (less than 2%) and it is concentrated mostly in the lower part of the domain, around the maximum ripple elevation (in non-dimensional height units, y^+=15.88). There is a phase displacement of $\Delta\Phi=1.25\pi$ radians between the velocity and the TKE (meaning that the TKE reaches its maximum about 0.04 s after the velocity minimum and the TKE minimum occurs an equal time delay after the velocity peak). The phase- and cross-channel-averaged TKE spatial distribution for each phase is shown in figure 5.5. We can distinguish two regions roughly corresponding with generation and dissipation processes, although the separation is not complete. The first is the upper part of the ripples, which is mainly a generation region. Creation of TKE starts at t=0.042 s (beginning of the deceleration stage) at the upstream side of the ripples; by t=0.125 s there are two maxima on the crests, one a bit downstream and a second located just below the crest vortex. The regions merge at t=0.17 s just before the TKE maximum; after t=0.208 s the TKE decreases (as shown in figure 5.1) although the structures on the

crests seem to expand in space. Notice that the generation and growth of the TKE patch located on the crests spans almost a complete period. After t=0.293 s the patch is advected by the background flow and moves rightwards towards the troughs. At first glance it seems to engulf a preexistent “blob” located at the upstream side of the ripples (t=0.042 s) and then dissipate until at t=0.25 s (again, almost a complete period after the beginning of the dissipation phase) only a weak patch of fossil TKE remains. But this evolution is not consistent with the rapid increase shown in Figure 5.1 from t=0.0833-0.125 s, which is difficult to ascribe to the crest structures. The answer lies in the longitudinal velocity variability field (U_1MS, not shown), which shows a generation episode from t=0.042 s to t=0.083 s located at the ripples' troughs, slightly above the recirculation zone.

SECTION 5.5 : IDENTIFICATION OF COHERENT STRUCTURES, CASE REYNOLDS 42

In this section I will describe the structures identified using the pressure field, cross-channel pressure gradient magnitude (cross pressure gradient for short), pressure gradient magnitude, vorticity magnitude and Q criterion. Due to the slowly evolving nature of this particular flow I will only discuss the observations for phase t=0, 0.083, 0.167 and 0.25 s. Instead of depicting the pressure field in a separate plot I have decided to show the contour lines as the background for all the other variables, with the added advantage of making comparisons between criteria more easy.

As shown in Figure 5.6-5.9 and specially in Figure 5.4 the large scale variations in the phase- and cross-channel-averaged pressure correspond roughly with coarse changes in the phase-averaged mean velocity field (lower pressure on crests and higher in troughs related to respectively faster and slower mean flow, with lateral excursions in the contours due to the oscillations in time). A closer look at the contours (more evident in Figure 4.6) reveals that the pressure field does delineate, albeit in a slanted form, departures from the background flow. Thus the recirculation zones (t=0.083 s, compare to the streamlines plot, Figure 5.4) show as indentations of the isobars; and the shear zone above the crests with its associated strong streamline curvature is clearly evident in Figure 5.6.

The phase- and cross-channel-averaged cross pressure gradient and pressure gradient magnitude fields confirm the information given by the pressure field and point towards the existence of new structures. As shown in Figures 5.6 and 5.7, the recirculation zone signal (t=0.083 s) is associated with maximum values of these variables evident in both plots (see also Figure 111) and the maxima observed on the crests at t=0.17 s can also be related to the patterns observed in the mean flow (strong streamline curvature and deceleration-acceleration of the counterflow); notice also the correspondence between the indentations and loops in the pressure field and the pressure gradient contours. But three new structures arise at t=0, 0.083 and 0.25 s which can not be related to the mean flow as described by the streamlines.

At t=0 s we observe peaks in the distribution of both quantities (although weaker in the case of the cross pressure gradient magnitude) at the downstream side of the ripples and in one of the crests. At t=0.083 s a new structure arises over the troughs (although barely discernible in the cross pressure signal) and again at t=0.25 s a strong signal is evident on the crests seemingly uncorrelated to the background flow. Notice that these structures do relate to deformations of the averaged pressure field.

The phase- and cross-channel-averaged vorticity magnitude and Q fields (Figure 5.8 and 5.9) confirm and qualify the picture obtained by the other criteria, but also point to the existence of a richer structure field. The examination of the vorticity magnitude contours (Figure 5.8) indicates that the structures described by the pressure criteria have a strong rotational component, but it also shows that its spatial distribution does not completely correlate with the aforementioned vortices. At phases t=0, 0.083 and 0.17 s the vorticity spans a substantial portion of the ripples downstream region, although the first two examples could be partially explained by the formation of the recirculation zone.

The Q field explains part of this discrepancy. The regions with high vorticity and low pressure gradient show also low Q values, which indicates the existence of high shear values (thus negating the precondition of cyclostrophy). Notice also that, although we have a close match between the pressure criteria and Q, Q values delineate the trough structures with much greater clarity than pressure

gradients do. From the fact that the trough vortices also show (relatively) high values of vorticity, we can infer that this is due to the existence of high shear which impedes the pressure field from achieving a condition of equilibrium.

An observation with reference to the relation between the phase- and cross-channel-averaged TKE and vortex detection criteria must be made. Until now, no consideration has been given to the dynamical processes that generate and destroy vortical coherent structures; as shown above, it is perfectly possible to design a purely kinematic vortex detection criterion. But numerous experiments and simulations correlate the existence of these structures with elevated values of TKE, and it is almost certain that vortices do play an important role in the creation, transport and dissipation of TKE. In our case, a comparison between the TKE contours (Figure 5.5) and Q values (Figure 5.9) shows that there is indeed a strong correspondence between the two; specially in the case of the trough regions (which are mainly dissipative zones), where high TKE correlates with elevated vorticity and low shear. The relation is a bit more complex on the crests (notice that the relatively high values of TKE upstream of the ripples at t=0.083 s do not show in the Q field; neither high Q values downstream the ripples show in the TKE contours); this can be due to the fact that at this stage of the flow TKE is being created by a strong shear without an adjacent generation of vorticity (but do notice that this is almost the only exception in the whole period; at any other time we can readily relate all TKE with corresponding Q structures).

The relation between Q values and TKE is also quite evident after looking at Figure 5.10, which shows the evolution of both variables with phase (the evolution of the other variables also shows a certain dependence with TKE, but none of them tracks the energy as closely as Q). The Q method thus has the advantage of serving not only as a vortex identification criterion but also as a good predictor of the evolution in time and distribution in space of the TKE.

In summary: the temporal evolution of case Re_42 shows a laminar-like stage and a period characterized by the formation of recirculation zones and vortices in the mean flow. All the criteria

considered detect, to a certain degree, the presence of vortical structures due to perturbations in the velocity and pressure field which can be sometimes related in space and time (but not necessarily in a bond of cause-effect) to the flow patterns as described by the streamlines. The Q criterion describes clearly and consistently a set of fluid parcels with vortex-like properties (high vorticity values, pressure gradient), which also correspond almost in a bijective, one to one, way to the regions with high TKE (which in no respect must be taken as an affirmation of cause-effect but more in the terms of a possibly common origin). The three other criteria considered (cross pressure gradient magnitude, pressure gradient magnitude, vorticity) identify, less successfully, those same structures in this particular case, although none seems to convey the amount of information given by the Q method. Discrepancies between the methods do exist but can be taken into account and explained by violations of the assumptions under which these methods work.

SECTION 5.6 : FLOW DESCRIPTION, CASE RE 150

The evolution of the phase-averaged longitudinal velocity is shown in figure 5.10. The oscillations' amplitude is 0.258 m s^{-1} and its period is 1 s. Notice that during 40% of the period velocity is negative (flow from right to left). The velocity profiles (figure 5.10 and 5.11) show the two flow reversals: the first between t=0.125-0.250 s (the flow changes from positive to negative) and the second between t=0.625-0.750 s. The vertical shear changes sign accordingly; at the lower part of the domain remains positive about 50% of the time. Shear variations in the outer region are relatively small and from y^+=30 to 70 it is actually fairly constant.

The flow evolution as described by the streamlines (figure 5.12) allows the definition of two stages. What I will call the “normal” stage (flow from left to right) spans from t=0.75 to 0.25 s. In this stage, the initial acceleration phase generates a recirculation zone at t=0 s which spans half the wavelength at t=0.125 s. Just before the flow reversal, this zone has grown into a full-fledged pair of vortices with height about two and a half times the ripples'. Due to the vortices presence there is a high vertical shear in the downstream side of the ripples and stretching in the upstream side. The flow reversal induces the

dissolution of the vortices at t=0.375 s; but once the flow decelerates again at t=0.625 s a second, much briefer, recirculation zone is generated. This recirculation disappears at t=0.75 s, the beginning of the normal phase (but notice the high vertical shear indicated by the aggregation of the streamlines in the upstream side of the ripples).

The longitudinal velocity field (not shown) corroborates the existence of the strongly sheared zone (indicated by the streamlines) in the left side of the ripples at t=0.75 s. No counterflow is observed between t=0.25-0.375 s (as opposed to the one in case Re42 at t=0.167 s, which corresponds to a similar phase in the flow evolution, see figure 5.4) although due to the relatively coarse sampling its existence is not impossible.

The TKE evolution reflects the phase duality (see figures 5.10 and 5.13). The energy variability is much bigger than in the former case (about 70%) and does not relate to the variation in velocity in an obvious way. In the normal stage, the beginning of TKE generation does not occur until t=0 s, when a weak signal is observed in the right (downstream)side of the ripples, in the recirculation zone. The TKE increases very rapidly in correspondence with the vortices' growth until reaching its maximum at t=0.250 s (notice the huge jump between t=0-0.125 s in figure 5.10-b. As depicted in figure 5.10-c, the energy created moves upwards with time until the peak reaches its maximum height at t=0.375 s while at the same time the profile is being smoothed. Flow inversion initiates a process of strong TKE advection and diffusion; the vortices containing the most part of the energy are displaced leftwards a total distance of roughly $1^1/_3$ wavelengths from t=0.25 s to 0.625 s (which marks approximately the end of this dissipation stage; see the associated decrease in figure 5.10).

A second, weaker, TKE generation episode happens during the reversed flow stage, starting at t=0.5 s until t=0.75 s. The energy is now being created in the upstream side of the ripples (still the right side due to the flow inversion and the side opposite to the recirculation zone, which points towards a creation mechanism different than that in the first stage) but the peak travels to the left side in just one phase. The amount of TKE generated in this stage is small enough that no signal remains at t=0 s (the

elongated contour observed at this phase corresponds probably to energy created in situ, not advected, although the last possibility can not be excluded by possible distance traveled arguments).

SECTION 5.7 : IDENTIFICATION OF COHERENT STRUCTURES, CASE REYNOLDS 150

This section will describe the coherent structures identified using the phase- and cross-channel-averaged pressure field, cross pressure gradient, pressure gradient magnitude, vorticity and Q criterion (figures 5.14-5.17).

The pressure field is depicted in figures 5.12 and 5.14-5.17. The first impression when looking at the streamlines is that the vortical structures in the mean flow induce much more pronounced pressure minima than in the case Re 42 (compare the signal associated to the vortices in figure 5.4, t=0.125-0.208 s with roughly the same flow stage in figure 5.12, t=0.25 s, and also the low values in the strongest recirculation zone at t=0.125 s, same figure) which of course could be explained either by a stronger circulation (due to the increase in Re) or by a longer available period to achieve equilibrium (see below). The contour lines (figures 5.14-5.17) show that the pressure field detects all the important flow structures (the three recirculation zones at phase t=0, 0.125 and 0.625 s; the vortices at t=0.25 s and the streamlines curvature in the upstream side of the ripples at t=0.75 s).

The pressure gradient magnitude (figure 5.15) renders a more complete picture; while in general it correlates strongly with the pressure field, it shows formations that, after being generated at t=0 s are advected by the velocity field and dissipate with time. These formations can not be completely related to the background velocity field and indicate a coherent structure resulting from a perturbation of the mean flow.

Although the vorticity magnitude (figure 5.16) confirms that these formations possess indeed a high rotation rate, and the maxima correlate precisely with the information given by the other criteria, the spatial extent of the structures outlined by the vorticity field is much greater than that as described by the pressure and Q values. Compare for example the pressure gradient magnitude field and the

vorticity field at phase t=0.5 s (figures 5.15 and 5.16). In the bulging formations at the right of the ripples, at a height of roughly 0.02 m the vorticity still reaches a value 20% of its maximum range while it is less than 10% in the case of the pressure gradient. This indicates that the separation between the structure signal and that corresponding to the background flow is sharper in the case of the pressure field than in the vorticity. Thus, the latter is less precise in the elucidation of vortices than the former. A further problem arises by the "contamination" of the vorticity signal by the background shear. This is particularly evident in phases t=0-0.125 s which show a layer of relatively high vorticity following the bottom superimposed over the structures. In the case of t=0 s, that actually prevents the elucidation of the vortex associated to the recirculation zone downstream the ripple. The best explanation for the existence of this layer and the ones at phase t=0.5-0.625 s is the generation of vorticity as an effect of the strong vertical shear immediately over the boundary.

The Q field (figure 5.17) supports this interpretation for the elevated vorticity in the bottom layer and indicates that there is indeed a strong shear at the bottom. The results from this method also match very closely the ones obtained with the pressure gradient criteria. The size of the structures detected by this criterion is the smallest of all considered and there is a sharp separation between them and the background signal (for example, at t=0.25 s the Q values at the periphery of the vortices – let us say, at a height of 0.01 m – are less than 10% of the maximum range, while the pressure gradient is still 50% and the vorticity is around 40-60%; compare figures 5.14, 5.16 and 5.17).

The position, size and evolution of fluid parcels with high TKE follow with great precision the Q contours (and of course the pressure gradient's and vorticity's with the caveats expressed above). The creation and dissipation of energy are strongly correlated with the appearance and destruction of coherent structures as identified by the diverse methods.

Summarizing, the application of the four criteria to this particular flow results in the identification of a set of coherent structures; their location, size and evolution parallels that of the TKE contours, which indicates that these structures are linked to the flow energy dynamics and possess high TKE. The Q criteria provides the clearest identification of these formations, the pressure gradient methods being a

close second. The information provided by the vorticity contours is contaminated by the existence of a highly sheared layer of fluid above the bottom, but it is consistent with the other methods and confirms that these structures have a high rotation rate.

SECTION 5.8 : FLOW DESCRIPTION, CASE RE 210

The evolution of the phase-averaged mean velocity is shown in figure 5.18. The oscillations have a period of 8 s and an amplitude of 0.125 ms^{-1}. Although the mean velocity is never negative, there is a strong counterflow at phase t=0. Figures 5.18-a, 5.19 show the evolution of the phase-averaged velocity profile. In the viscous and buffer layers, the shear changes its sign (from positive to negative) between the phases t=2-3 s and again (from negative to positive) between 4-5 s. In the logarithmic zone there are significant variations in the shear magnitude but not in its sign. The vertical span of this zone also changes with time: it is minimum at phase 0 s (approximately 5 wall units, y^+), increases two seconds afterwards to 15 wall units, decreases before the flow reversal and then increases again to 15 wall units (t=6-7 s). The deviation of the velocity profiles from the law of the wall is the highest among the cases considered so far. Notice the effects of the upper boundary in the profile at a height as low as 10 wall units at phase 0 s.

Comparing the phase- and cross-channel-averaged velocity contours (figure 5.20) with the corresponding plot for Re 42 (figure 5.3) and Re 150 (not shown) we observe that the horizontal variations in the mean background flow due to the effect of the ripples is relatively small (notice the relatively horizontal gradation of the velocity, specially in phases t=7-1 s), in opposition to cases Re 42 – 150. Thus the background vertical shear in this flow is relatively elevated and uniform in the x_1 direction, as opposed to localized in space in the anterior experiments. As mentioned before, although there is no flow reversal the counterflow achieves a high vertical span (approximately 0.025 m in phase t=4 s); observed velocity values are low (around 0.04 ms^{-1} maximum, again in phase t=4 s) which does not exclude the existence of a stronger countercurrent between phases t=2-4 s due to the vortex lifting process (see commentary on the streamlines below).

The evolution of the streamlines does not depart substantially from the general pattern seen in lower Reynolds number flows. The background flow shows vortical circulation (either recirculation zones or vortices) during 90% of the period. The acceleration phase is characterized by the formation of a recirculation zone about one second after its beginning (t=5-6 s); this zone intensifies and grows until at phase t=2 s it occupies more than $^3/_4$ of the area below the ripples maximum height. Immediately after that the vortices (which now are about 0.01 m tall and as long as the ripples' wavelength) are lifted from the bottom (t=3 s); this effectively separates the upper half of the domain from the lower, with the creation of a counterflow layer about 0.05 m thick over the bottom. This countercurrent has a low velocity (~0.02 ms^{-1}) although it is possible that in the initial stages of the separation the flow was stronger. The vortices reach their maximum height (~0.024 m) during the velocity minimum, although their circulation seems feebler than in the anterior phase and their shape is less well defined. With the beginning of the acceleration stage the vortices disappear and the background flow acquires a short-lived laminar-like quality (t=5 s).

Figure 5.18-d shows the change of phase-averaged TKE with time; the variation is significant (about 72% of its maximum value). The energy peak happens about one and a half seconds after the velocity maximum, while the phase difference between velocity and TKE lowest values is two seconds. Figure 5.23 shows the evolution of the phase- and cross-channel-averaged TKE contours, which is very different from the observed in the case Re 42 and Re 150. The generation of TKE begins at phase t=6 s in the downstream side of the ripples during the acceleration stage, after the creation of the recirculation zone. The fan-shaped high energy flow region expands until at t=0 s reaches its maximum extension, covering an area almost equal to that of the domain below the crests. Shortly afterwards, at the beginning of the deceleration stage, the highly energetic core contracts until it disappears at t=2 s. From phase t=7 to 4 s a process of vertical diffusion of TKE can be observed (see also figure 5.18-c, where the smoothing and vertical displacement of the TKE peak are very noticeable).

The major contributions to the fan-shaped high energy region in phases 7-1 s come from the longitudinal velocity and the vertical velocity variabilities, while the cross-channel velocity signal is very

low (figures not shown). The latter reaches its maximum values during the same period as the TKE but in the upstream side of the ripples (the contribution can be detected in the energy signal as a small zone of relatively high values at t=0 s).

SECTION 5.9 : IDENTIFICATION OF COHERENT STRUCTURES, CASE REYNOLDS 210

The phase- and cross-channel-averaged cross pressure gradient, vorticity magnitude and Q fields are shown in figures 5.24-5.26. The pressure field is shown with the streamlines in figure 5.21 and as black contour lines in the background of figures 5.24-5.26.

The most salient characteristic of the pressure field as shown in figure 5.21 is that the pressure difference between the recirculation zones and the vortices and the background flow is very small compared with the variations due to the mean flow. The presence of the recirculation zones seems to displace the pressure maxima from its position in the troughs to a more downstream location, but this is as far as the pressure field goes to acknowledge their existence. Thus the case Re 210 resembles more the lowest Reynolds number experiment, Re 42, than the intermediate, Re 150, where at least the strongest structures were unequivocally associated with negative pressure values (compare figures 5.4, 5.12 and 5.21). In contrast, the contour lines (figures 5.24-5.26) allow us to infer the presence of some structures; while the vortex pair in t=3-4 s remains inconspicuous (the isobars in the lower part of the domain do relate to the presence of a vortex, but those in the upper half are inconclusive), the deformations of the contours associated with the main flow could be correlated with the recirculation zones at t=6-1 s (and with a bit of imagination even t=2 s).

The cross pressure gradient and the pressure gradient magnitude fields are almost identical so I will show just the former (figure 5.24). The plot shows a structure that originates at t=6 s (the signal is very weak but discernible), grows rapidly into a fan-shaped blob that occupies the domain below the ripples' height (t=0 s) and then dissipates (t=2 s, although some remains can still be seen at t=3 s). The cross pressure contours correlate almost exactly with the pressure deviations from the background.

Figure 5.25 shows the vorticity magnitude field. Although the general pattern is similar to that of the pressure gradient, some interesting differences must be noted. In the first place, the vorticity signal is stronger at t=6 s than the corresponding pressure or Q fields. It shows a clearly defined structure spanning the whole trough, laying over the recirculation zone. One second later, the vorticity has expanded to occupy the complete ripples' wavelength. The lower and upper limits of the vorticity peak are respectively the recirculation zone and a line connecting the ripples' crests (the pressure gradient upper limit, in contrast, seems more affected by the wavy bottom). Vorticity reaches its maximum intensity and extension at t=0 s, and then decays a bit more slowly than the pressure. Notice also that the highest vorticity values are located near the downstream side of the ripples, while the corresponding pressure gradient peaks are towards the center-right side of the trough.

Figure 5.26 depicts the evolution of the Q contours, which clarifies and complements the information provided by the other methods. In general lines, Q values agree with the pressure, pressure gradient and vorticity contours, although small discrepancies exist. For example, while the pressure gradient signal in phase t=7 s (figure 5.24) is confined to the center-right part of the trough, the high vorticity region spans from crest to crest (figure 5.25). Generally low Q values in a pattern coincidental with the pressure gradient point that this difference is due to the existence of a high shear region downstream the ripples. Comparison between the vorticity and Q contours indicates that, at t=0 s, this shear zone has either disappeared or been overcome by the vortex rotation strength. Overall, the comparison between Q and vorticity plots points towards the existence of a strong shear in the lower half of the domain, specially the layer overlying the bottom, which explains why the Q signal is relatively weak during the whole period.

Looking at the relation between the TKE and the vortex identification criteria we can observe that the structures elucidated by the different methods follow closely the energy evolution (compare figures 5.24-5.26). Figure 5.18-d shows that both Q and the vorticity magnitude relate to the variation of TKE with time.

Summing up, all four identification methods show the existence of flow regions with high vorticity and pressure gradient values. As measured by the Q criterion, the rotation rate overcomes the shear in these particular flow subdomains and subsequently they fulfill al the requirements to be coherent structures. These coherent structures possess high TKE, and the energy evolution of the system is closely mirrored by their variation in time.

SECTION 5.10: THREE-DIMENSIONAL DISTRIBUTION OF COHERENT STRUCTURES

This section deals with the description of the structures' three-dimensional distribution using the cross pressure gradient, pressure gradient magnitude, vorticity magnitude and Q isosurfaces. I will compare the results using flow snapshots and phase averages for the three cases (Re 42, Re 150, Re 210) in order to relate the observations using the instantaneous field to the mean quantities.

The Q method seems to describe in better detail the structures field for case Re 42 (see further comments below); thus, in order to study their evolution, a time series of the Q isosurfaces for a complete cycle (case Re 42, non-phase-averaged) is shown in figure 5.27. Although at first glance confusing (notice the high number of filaments spread over the bottom of the domain through the whole cycle), it is possible to discern the development of individual structures if we separate the flow domain in two different stages. The generation and growth stage happens primarily at the crests and spans almost one complete cycle. During this stage an elongated blob is generated at the downstream side of the ripples during the deceleration phase (t=0.0833-0.167 s). This relatively homogeneous formation is displaced upwards towards the crest and then grows in the shape of short filaments aligned parallel to the cross-channel direction (t=0.208-0.250 s). During the acceleration phase (t=0.250-0 s) the blob is advected by the background flow towards the troughs and suffers an stretching in the longitudinal direction. This announces the beginning of a second stage, characterized by the advection and decay of the structures created during the first one. This second stage spans also almost a complete cycle (from t=0.292 to t=0.208 s). We can observe how the structures become more elongated in the x axis and move rightwards a distance about one ripple wavelength until the become less and less well

defined (compare the filaments over the troughs at t=0.0833 s with the irregular blobs at t=0.208 s) and dissipate. This dynamics is consistent with the flow evolution described by the two-dimensional plots in section 5.5.

Figure 5.28 shows a comparison between the different criteria used for vortex elucidation. Although all the methods describe a similar general distribution the details vary widely. As explained in Jeong 1995, the intrinsic length scale of pressure variations in a vortex is larger than, say, vorticity's; thus the pressure field (either cross pressure or pressure gradient magnitude) is unable to show the smaller filaments clearly defined by the Q isosurfaces. The vorticity field shows lengthscales intermediate between those described by pressure and Q; but Q isosurfaces show structures over the troughs with relatively low vorticity and does not show high vorticity regions near the crests, presumably due to high shear values.

The agreement between different methods is better for case Re 150; all the criteria describe a cross channel vortex, relatively uniform in the y direction, the evolution of which is adequately described by the two-dimensional plots (see figures 5.12-5.17) with the exception of phases t=0-0.125 s. Figure 5.29 shows the vorticity, cross pressure gradient and Q fields corresponding to t=0.125 s for both the averaged and non-averaged case. While the vortex associated with the recirculation zone (compare with figures 5.12) is depicted similarly by the three methods, the longitudinal filaments are not, with the implication of possibly different generation mechanisms. The vorticity magnitude isosurfaces imply that elongated structures are generated in the upstream side of the ripples and then coalesce into the cross-channel vortex located in the recirculation zone. The Q field seems to indicate that these same filaments originate in the downstream side of the ripples, inside the recirculation zone, and are then advected over the trough and towards the upstream side by the mean flow.

A similar conundrum occurs in the case Re 210. I have pictured the evolution of the vortex field in figure 5.30, from phase t=7 to 1 s, using the non-averaged field. Again, notice that in the vorticity field the filaments seem to originate from the crests while the Q isosurfaces show no evidence of that origin.

Figure 5.31 shows a comparison between the vorticity, pressure gradient and Q isosurfaces (using both averaged and non-averaged variables); only vorticity (in both mean and instantaneous plots) depicts the crests filaments. It must be taken into account that the TKE distribution (figure 5.23) is consistent with a mechanism generating energy at the crests, thus supporting the vorticity hypothesis.

CHAPTER 6: SUMMARY AND CONCLUSIONS

Oscillatory and pulsating boundary layer flows over sand ripples due to surface gravity waves have a major impact in many processes of geophysical and biogeochemical interest: erosion, transport and deposition of sediments in coastal environments, chemical fluxes through the water-sediment interface, ripples' migration, generation of microbiotopes for marine organisms, to name just a few. Thus an improved knowledge of the processes that occur in that environment is of great importance, especially taking into account the high economic and social value of coastal zones where such phenomena occur.

The ability of several methods (pressure, pressure gradient magnitude, cross pressure gradient, vorticity magnitude and Q criterion) to identify and track the evolution of coherent structures in such flows has been evaluated using velocity and pressure fields for representative cases obtained from LES. Three different Reynolds numbers have been studied, in an attempt to analyze the adequacy of the elucidation methods in a range of conditions such as forcing period, ratio between the oscillatory and the steady forcing, distribution of the shear stress and mean flow patterns. Although all the methods capture adequately the major flow features in three-dimensional fields (both in the instantaneous and the averaged case), only the Q criterion and, to a certain extent, vorticity magnitude isosurfaces are able to elucidate the finer details of the structures. The observation by Jeong 1995 that the pressure field has a larger intrinsic scale than other variables is corroborated in our case.

The extension of the vortex concept to an averaged quantity proves useful in the elucidation of physically relevant flow structures and its relation to the energy dynamics. The evolution of coherent structures detected by the Q criterion in the instantaneous velocity field in all three cases can be related to the cross-channel averaged sections; again, the Q method seems to provide the most insight into the physical processes involved. Despite the differences in the dynamics between the three flows (in case Re 42, energy generation and dissipation spans two full cycles and coherent structures are distributed

all along the domain; in cases Re 150-210, energy dynamics is much more localized in time and space) there is a positive relation between cross-pressure gradient, pressure gradient magnitude, vorticity magnitude, Q values and TKE in the cross-channel, phase averaged two-dimensional fields. Differences between variables can be explained in terms of flow conditions (high shear, high acceleration regions); the assumptions made (cydostrophy, steady state, planarity), although restrictive, do not have an excessively negative impact in the elucidation of structures.

The study of the generation and distribution of coherent structures also allows us to distinguish between flow regimes as a function of the Reynolds number. The case Re 42 differs essentially from the case Re 150 and Re 210. In the former, the structures' generation and dissipation process spans two complete cycles while in the latter it is much shorter in time. In Re 42 the coherent structures (and the region with high TKE) occupy a significant fraction of the flow domain, even intruding significantly into the outer layer, while in the case Re 150 and Re 210 are located mainly in the ripple's downstream region. Thus the average mass and energy vertical flow is potentially greater for Re 42, even if the sediment pick up rates and TKE generation are bigger for Re 150 and Re 210 due to a higher Reynolds number.

Future research could focus in assessing the robustness of the elucidation methods with respect to resolution considerations (perhaps even assessing the effect of terrain-following versus non-terrain following grids); the structures' dynamics points to the desirability of having an increased resolution not only in the lower part of the domain, but also up to a height about 1/4 of the ripples' amplitude over the crests. Increased sampling frequency during the critical moments of vortex generation (not necessarily during all the cycle) is a must if we wish to ascertain the mechanisms that create such instabilities. It could also be interesting to relate the quantities observed in the water column to the stresses at the bottom, which demands a more sophisticated treatment in the postprocessing stage of the variables lying over the interface water-sediment.

Table 1: Simulation parameters

File name	Period (s)	Re	$\frac{\tau_{wall}}{\rho}$ (m^2s^{-2})	$U_f=\sqrt{\left(\frac{\tau_{wall}}{\rho}\right)}$ (ms^{-1})	$l_s=\sqrt{\left(\nu\frac{T}{\pi}\right)}$ (m)	Ripples' height (m)	Addimensionsionalized ripples' height
RE 42	1/3	42	$9.61*10^{-4}$	0.031	$3.25*10^{-4}$	0.005	15.38
RE 150	1	150	$4.84*10^{-4}$	0.022	$5.64*10^{-4}$	0.005	8.86
RE 210	8	210	$7.84*10^{-4}$	0.028	$1.60*10^{-3}$	0.005	3.125

Table 2: List of variables calculated by the post-processing code

Variable name	Definition	Mathematical Expression
Perturbation velocity	velocity minus the instantaneous cross-channel average	$u'_i(x_j,t)=u_i(x_j,t)-\overline{u}$
Perturbation pressure	pressure minus the instantaneous cross-channel average	$p'(x_j,t)=p(x_j,t)-\overline{p}$
Pressure gradient	perturbation pressure gradient	$p'(x_j,t)_{,i}$
Cross-channel pressure gradient:	magnitude of the pressure gradient in the radial direction normal to the longitudinal axis	$\nabla p'_c=\sqrt{((u',_2)^2+(u',_3)^2)}$
Pressure gradient magnitude		$\lvert\nabla p'\rvert=\sum_{j=1}^{3}(p',_j)^2$
Q	second invariant of the perturbation velocity gradient tensor	$Q=-\left(\frac{1}{2}\right)u_{i,j}u_{j,i}$
Vorticity	rotation rate	$\omega_i=\epsilon_{ijk}u_{k,j}$
Vorticity magnitude		$\lvert\omega_i\rvert=\sqrt{\left(\sum_{i=1}^{3}\epsilon_{ijk}u_{k,j}\right)^2}$
U_iMS	Mean Square perturbation velocity, the square of the velocity variance	$U_iMS(x_j,t)=\overline{(u_i-\overline{u})^2}$
TKE	Turbulent Kinetic Energy	$TKE=\frac{1}{2}(u_iu_i)^2$
Ripple Mask	is an integer that flags the cells lying below the ripples	1 if $z > z_{wall}$ -1 if $z < z_{wall}$

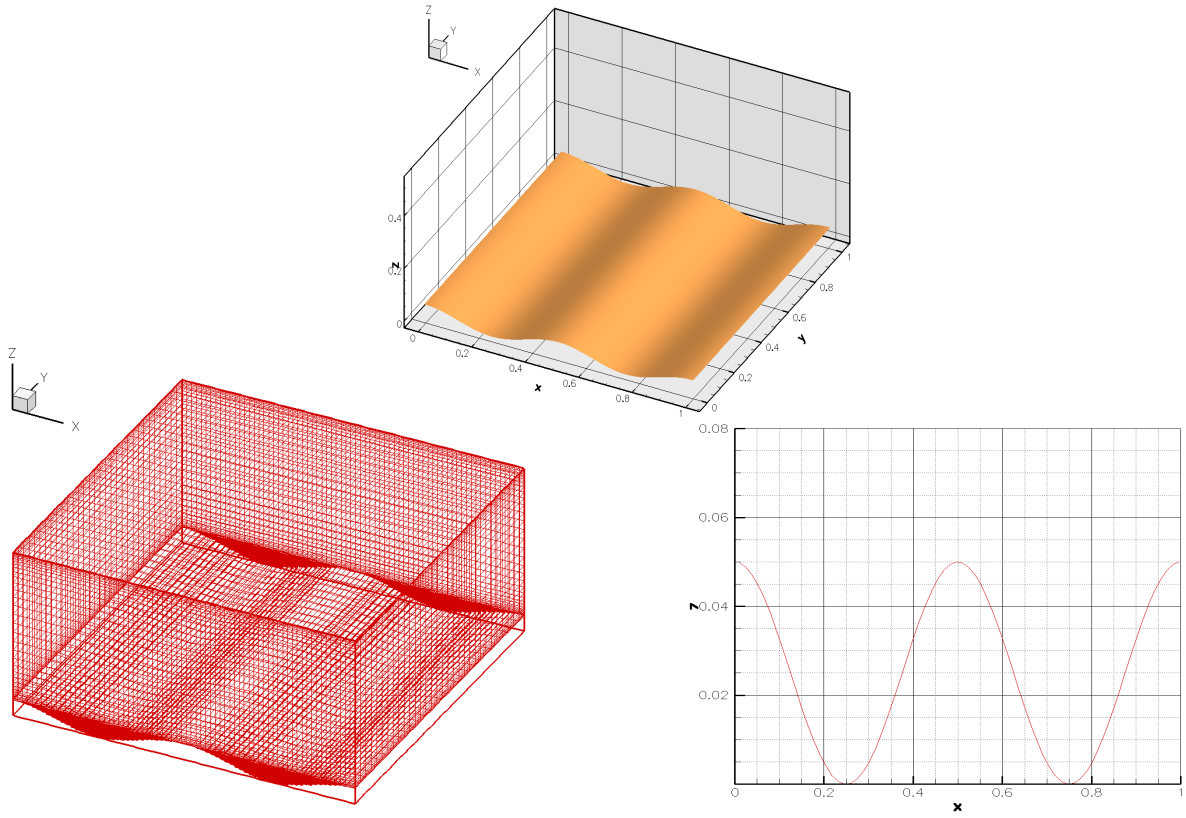

Figure 1.1: Computational domain. a) Shaded plot of the immersed bottom boundary. b) Grid with 288x64x128 cells (not all cells are shown) plus bottom boundary: cells lying under the ripples have been blanked out. Notice the increased vertical resolution in the lower part of the domain, below the ripples' crest height. Differences in vertical resolution between crests and troughs could affect the ability of the simulation to model the evolution of the coherent structures. c) The cross-section of the bottom is a sinusoidal curve defined as:

$$z_{wall} = \alpha_{wall} * \left[1.0 + \cos\left(\frac{2 * \pi * x}{\lambda_{wall}} \right) \right]$$

λ_{wall} being the wavelength (0.05 m) and α_{wall} the amplitude of the ripples (0.005 m; notice vertical exaggeration)

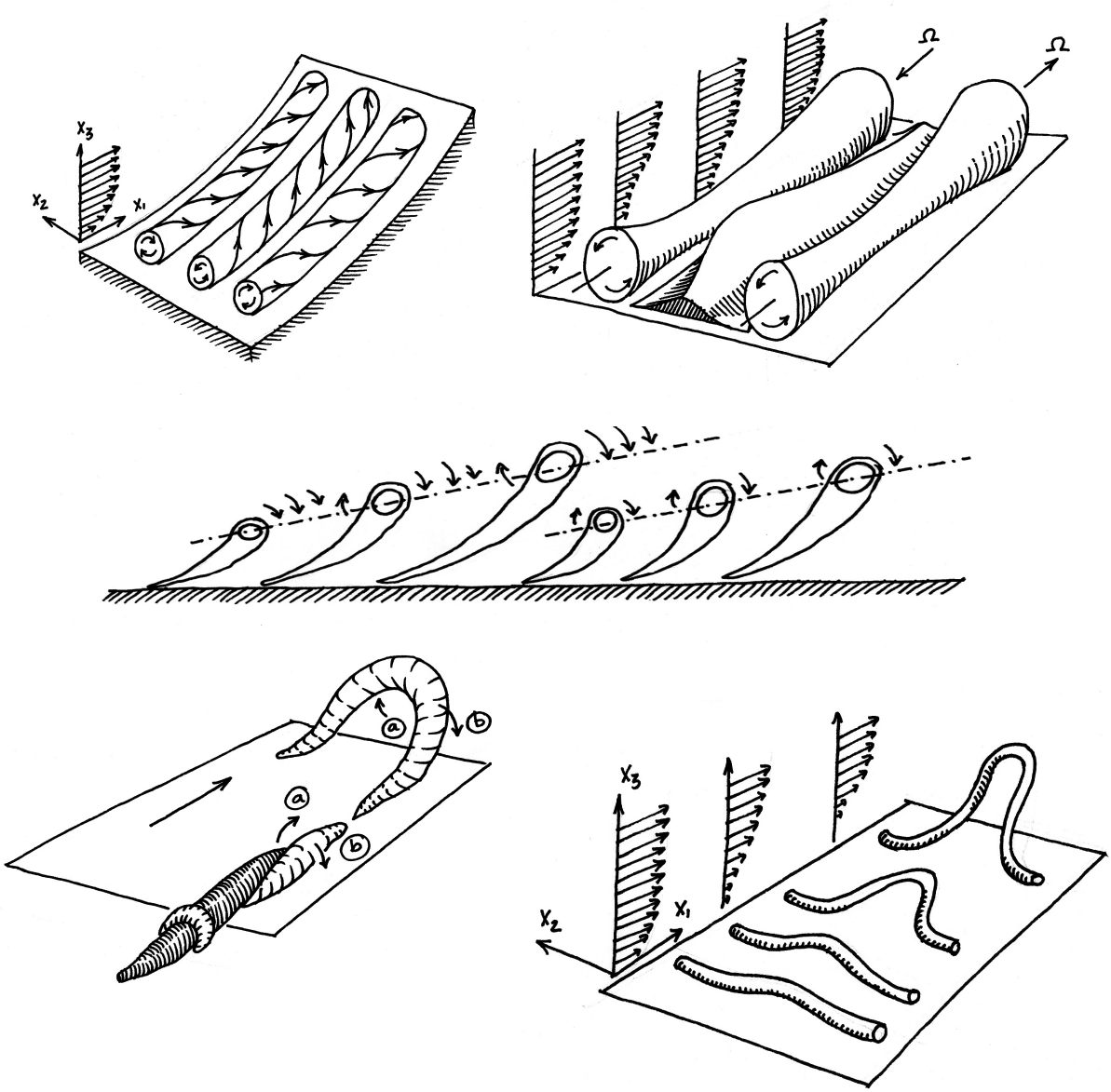

Figure 3.1: Upper left: Counter-rotating vortices generated by Görtler instabilities in a concave bottom; experiments show that such vortices can lift up low momentum fluid from the viscous layer and create low velocity streaks, with a cross-channel wavelength $\nu/u_\tau = 100-200$ (redrawn from Swearingen 1987). Upper right: a detailed view of how counter-rotating vortices draw up low momentum fluid from the viscous layer (redrawn from Carlier 2005). Lower right: conceptual model of the generation and growth of a hairpin vortex. The vortex starts as a cross-channel roll created by the vertical gradient of the longitudinal velocity. A secondary instability generates an indentation in the roll which grows and is lifted by self-induction processes and the interaction between the vortex and the mean flow gradient, which furthermore stretches and elongates the filament until, in a last stage (not shown) the vortex can break up and generate a pair of counter-rotating structures. More frequently, the symmetry of the structure is broken during this last stage and a single roll, sometimes called cane, is created (redrawn from Robinson 1991). Lower left: Generation of high momentum fluid sweeps and low momentum burst by arch structures in the viscous and logarithmic layer. The dark structure in the foreground under the

small arch is a low velocity streak generated by fluid from the viscous layer advected by the longitudinal vortex in the middle (a). The same filament brings down high momentum fluid from the buffer layer (b), a process called a sweep. The arch or horseshoe vortex depicted in the background shows a similar dynamics, lifting low momentum fluid at (a) (burst) and advecting high momentum fluid at (b) (redrawn from Robinson 1991). Center: a cross section of a hairpin vortices packet. Flow is from left to right. Hairpin vortices are generated in groups or packets; interactions between vortices inside the packet transfer TKE from smaller scales to larger wavelengths. When a bigger, older packet overcomes a smaller, younger one, interactions between packets by vorticity induction can twist and deform the vortices in a extremely complicated manner (redrawn from Natrajan 2006).

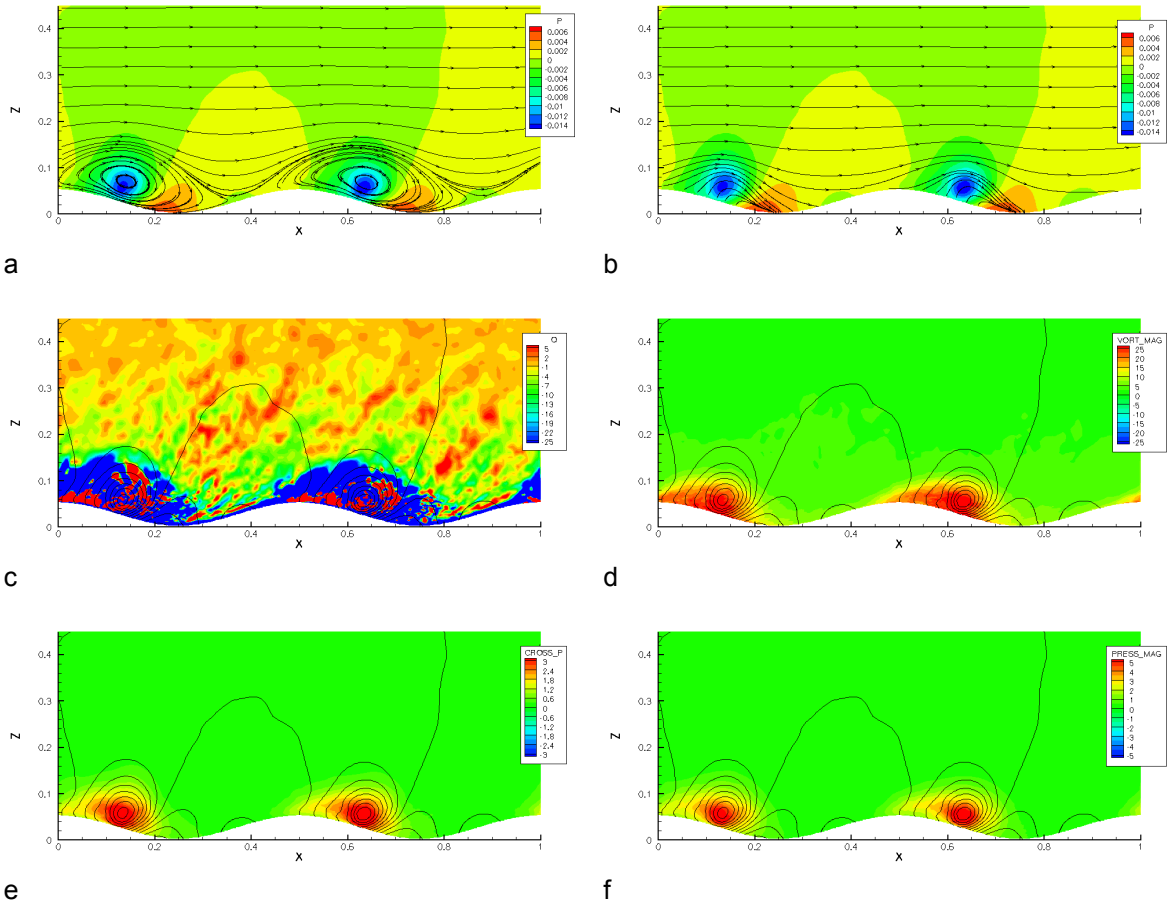

Figure 4.2 : Vortex identification criteria. Case Re_150b, t=0.25 s, phase and cross-channel average (10 cycles). a) Streamlines and pressure contours. b) Streamlines using a reference system moving with the same longitudinal speed as the vortices ($u_{1(vortex)}$=-0.0039 ms^{-1}). Streamlines are not invariant versus a Galilean transformation. c) Q contours (in color; cross-channel mean has been substracted) and pressure contours (lines). Pressure contours are plotted as an aid for comparisons between different graphs. d) Vorticity magnitude contours (cross-channel mean has been substracted). e) Magnitude of the pressure gradient in a plane normal to the longitudinal axis (cross-channel mean has been substracted) . f) Magnitude of the pressure gradient (cross-channel mean has been substracted) .

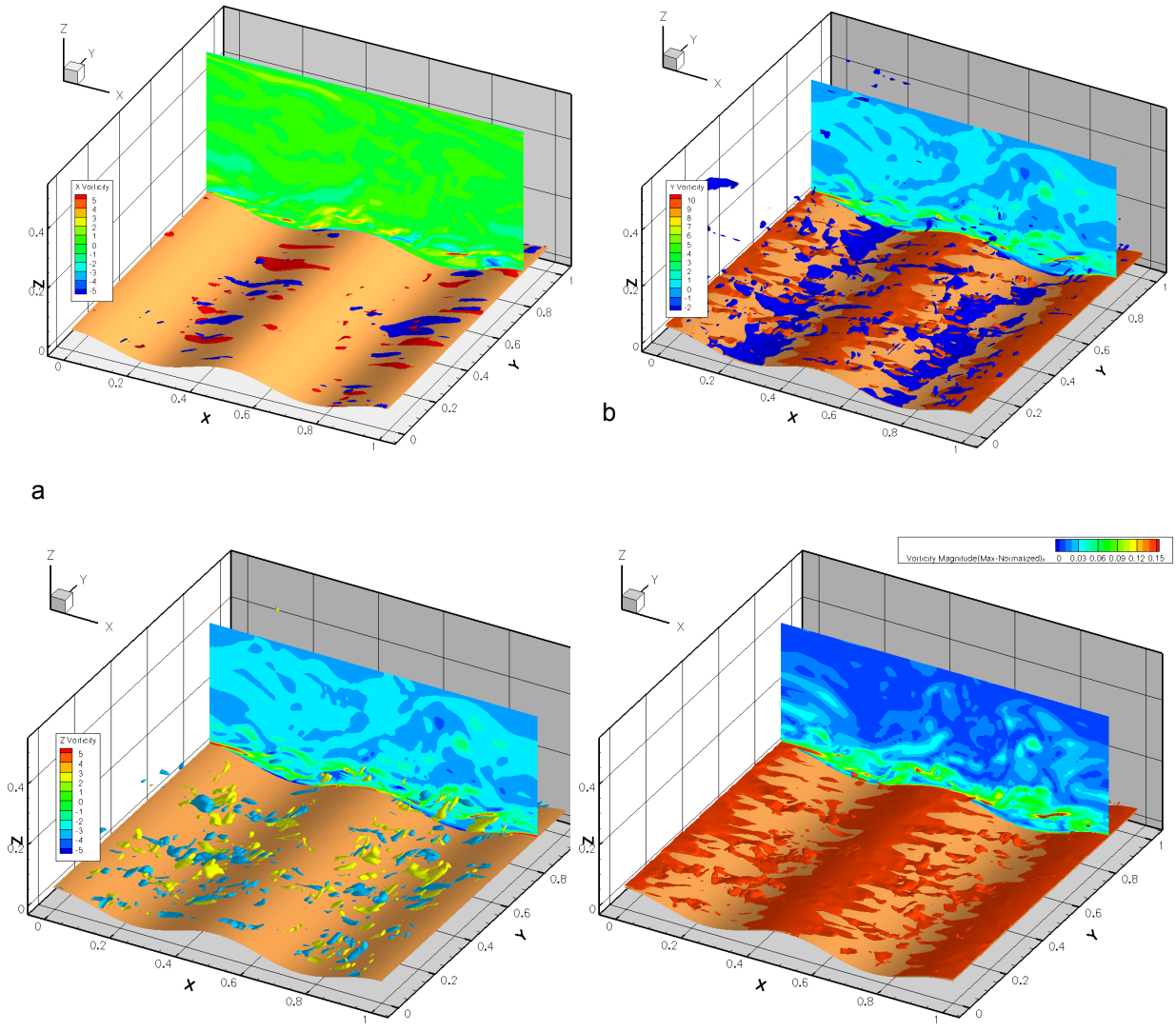

Figure 4.3 : Data set *output_u064*. Instantaneous field; cross-channel mean has not been substracted from the velocity field. a) Longitudinal component: slice at y=0.85 and isosurfaces for $\omega_x = \pm 70\, s^{-1}$ b) Transversal component: slice at y=0.85 and isosurfaces for $\omega_y = 95\, s^{-1}$ and $\omega_y = -25\, s^{-1}$. c) Vertical component: slice at y=0.85 and isosurfaces for $\omega_z = \pm 25\, s^{-1}$ d) Vorticity magnitude: slice at y=0.85 and isosurface for $|\boldsymbol{\omega}| = 15\, s^{-1}$.

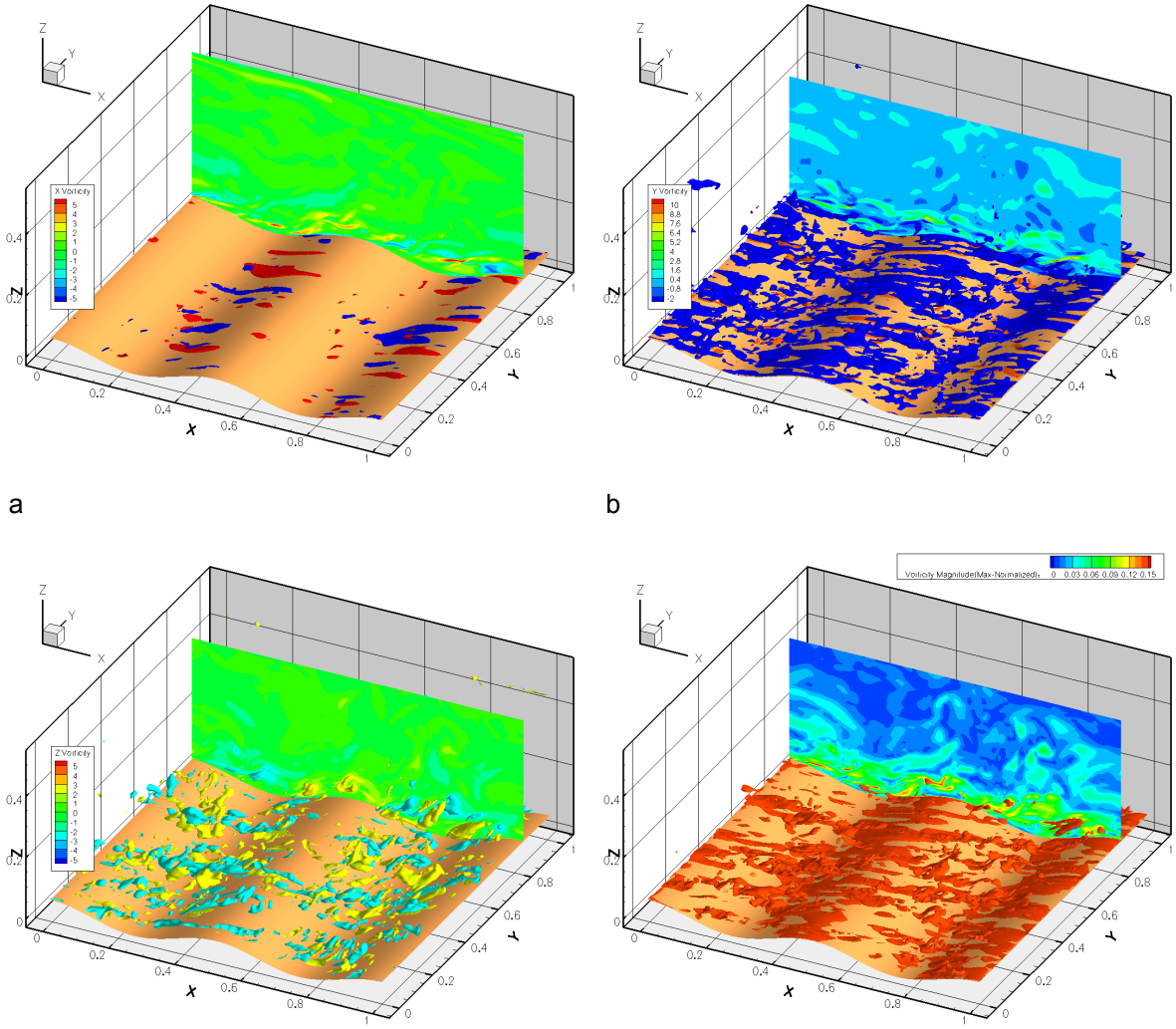

Figure 4.4 : Dataset *output_u064:* Instantaneous field. Cross-channel mean has been substracted from the velocity field; compare with Figure 4.3. a) Longitudinal component: slice at y=0.85 and isosurfaces for $\omega_x = \pm 7\, s^{-1}$ b) Transversal component: slice at y=0.85 and isosurfaces for $\omega_y = 95\, s^{-1}$ and $\omega_y = -25\, s^{-1}$ c) Vertical component: slice at y=0.85 and isosurfaces for $\omega_z = \pm 25\, s^{-1}$ d) Vorticity magnitude: slice at y=0.85 and isosurface for $|\boldsymbol{\omega}| = 15\, s^{-1}$.

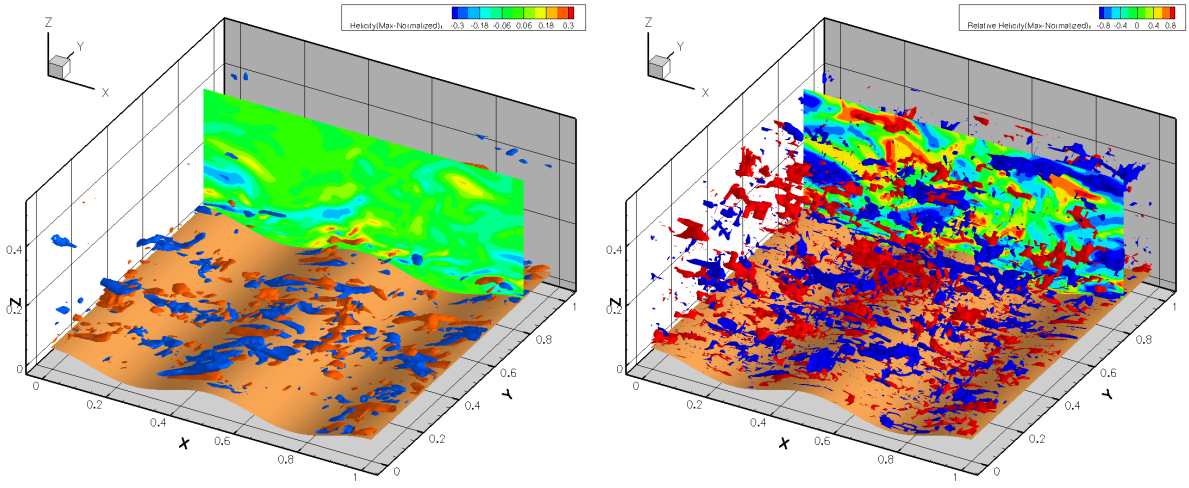

a b

Figure 4.5 : Dataset *output_u064*. Instantaneous field; mean has not been substracted from the variables. a) Helicity density: slice at y=0.85 and isosurfaces for h = 0.95 ms^{-1} and h = -0.95 ms^{-1} b) Relative helicity density: slice at y=0.85 and isosurfaces for h_r = 0.95 and h_r = -0.95.

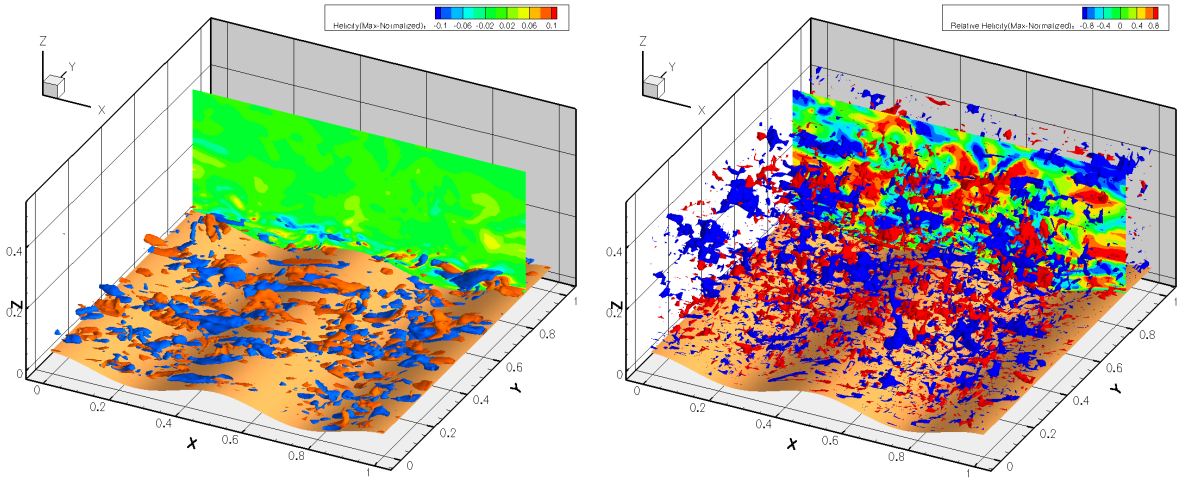

a b

Figure 4.6 : Dataset *output_u064*. Instantaneous field; cross-channel mean has been substracted from the variables. a) Helicity density: slice at y=0.85 and isosurfaces for h = 0.95 ms^{-1} and h = -0.95 ms^{-1} b) Relative helicity density: slice at y=0.85 and isosurfaces for h_r = 0.95 and h_r = -0.95.

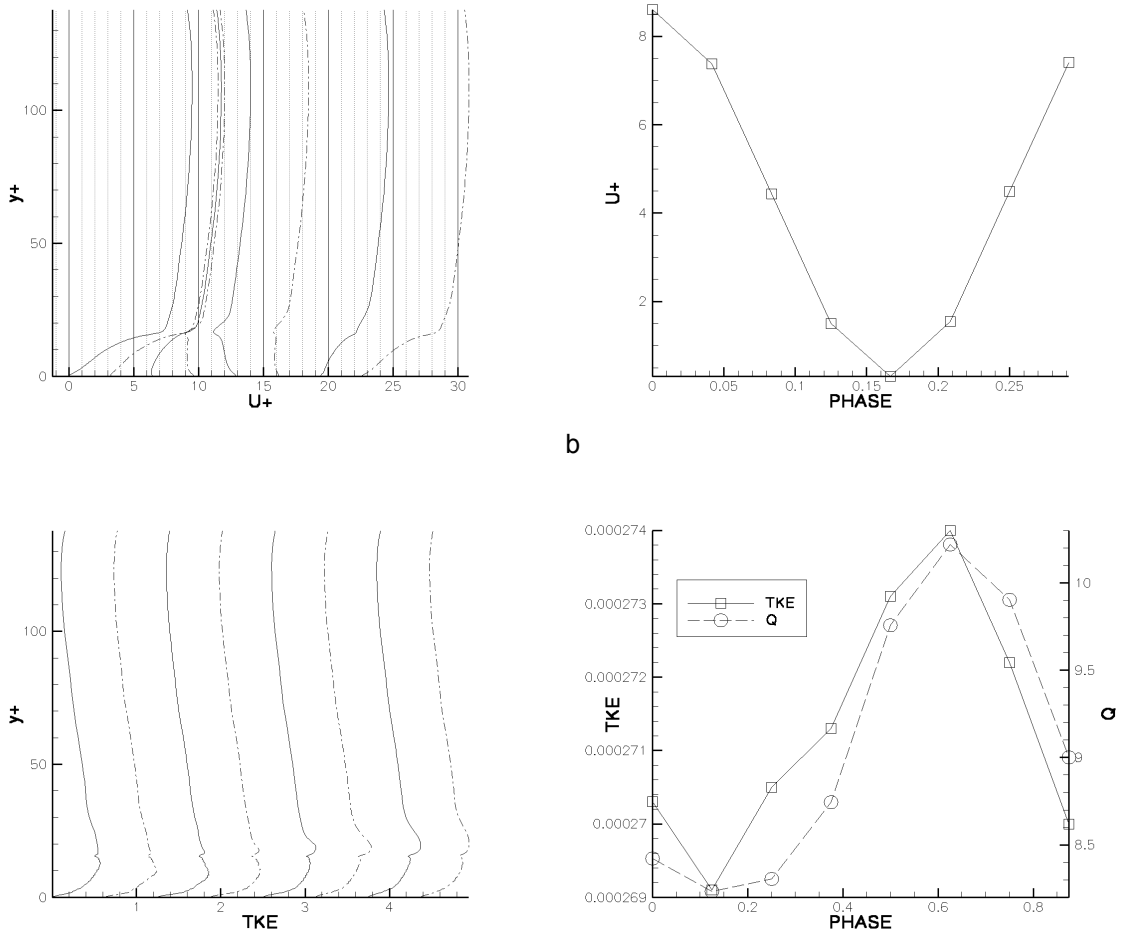

Figure 5.1 : Re_42 (phase average over 10 cycles) a) Evolution of the cross-channel averaged longitudinal velocity versus height. Velocity has been normalized with the friction velocity U_f and height has been normalized with l_s. The leftmost plot corresponds to phase t=0 and each consecutive phase has been displaced to the right an amount $\Delta U^+=3.22$. Alternate line styles (solid line versus dashed line) have no physical relevance and are used to increase legibility. Ripples' maximum height is $y^+=15.38$. Notice the presence of a counterflow starting at phase t=0.125 until t=0.208. This counterflow reaches a maximum height $y^+=40$ at phase t=0.167. b) Volume-averaged longitudinal velocity versus phase. Velocity has been normalized using the friction velocity. The evolution of the averaged longitudinal velocity is symmetrical and the mean flow is always positive (pulsating flow). c) Evolution of the cross-channel-averaged TKE versus height. TKE has been normalized using the square of the friction velocity. Each consecutive phase has been displaced an amount $\Delta TKE=3.12$. For other details refer to commentaries in figure a). The TKE profile remains almost unchanged through the cycle, with a local maximum about the ripples' height at $y^+=15.38$. d) Volume-averaged TKE and Q versus phase. Variations in the TKE are very small throughout the whole cycle (in the order of 2%).The flow achieves a minimum in the TKE at t=0.0417 s, immediately after the velocity maximum. TKE increases almost linearly during the deceleration phase until its maximum at t=0.208 s, 0.04 s after the velocity minimum, and decreases rapidly after that. Notice how closely Q values track TKE variations with time.

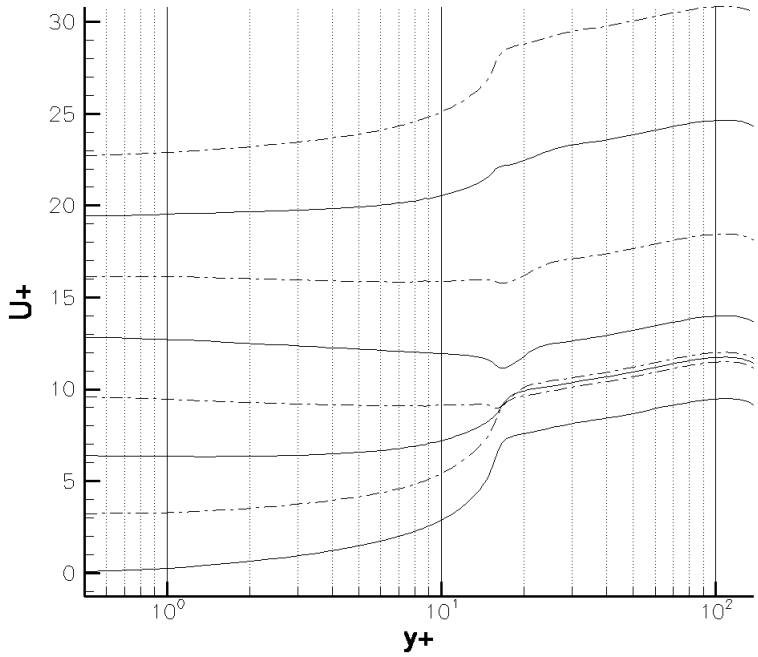

Figure 5.2 : Re_42 (phase average, 10 cycles) Evolution of the cross-channel-averaged longitudinal velocity versus normalized height. Velocity has been normalized using the friction velocity U_f and height using l_s. Notice logarithmic scale for y^+. The lowermost profile corresponds to phase t=0 and each consecutive profile has been displaced upwards an amount $\Delta U^+=3.22$. Differences in line style (solid line versus dashed line) are for the sole purpose of legibility. Visual inspection shows that longitudinal velocity conforms to the law of the wall throughout the whole cycle from $y^+=30$ to $y^+=90$, the strongest deviations happening during the latest phase.

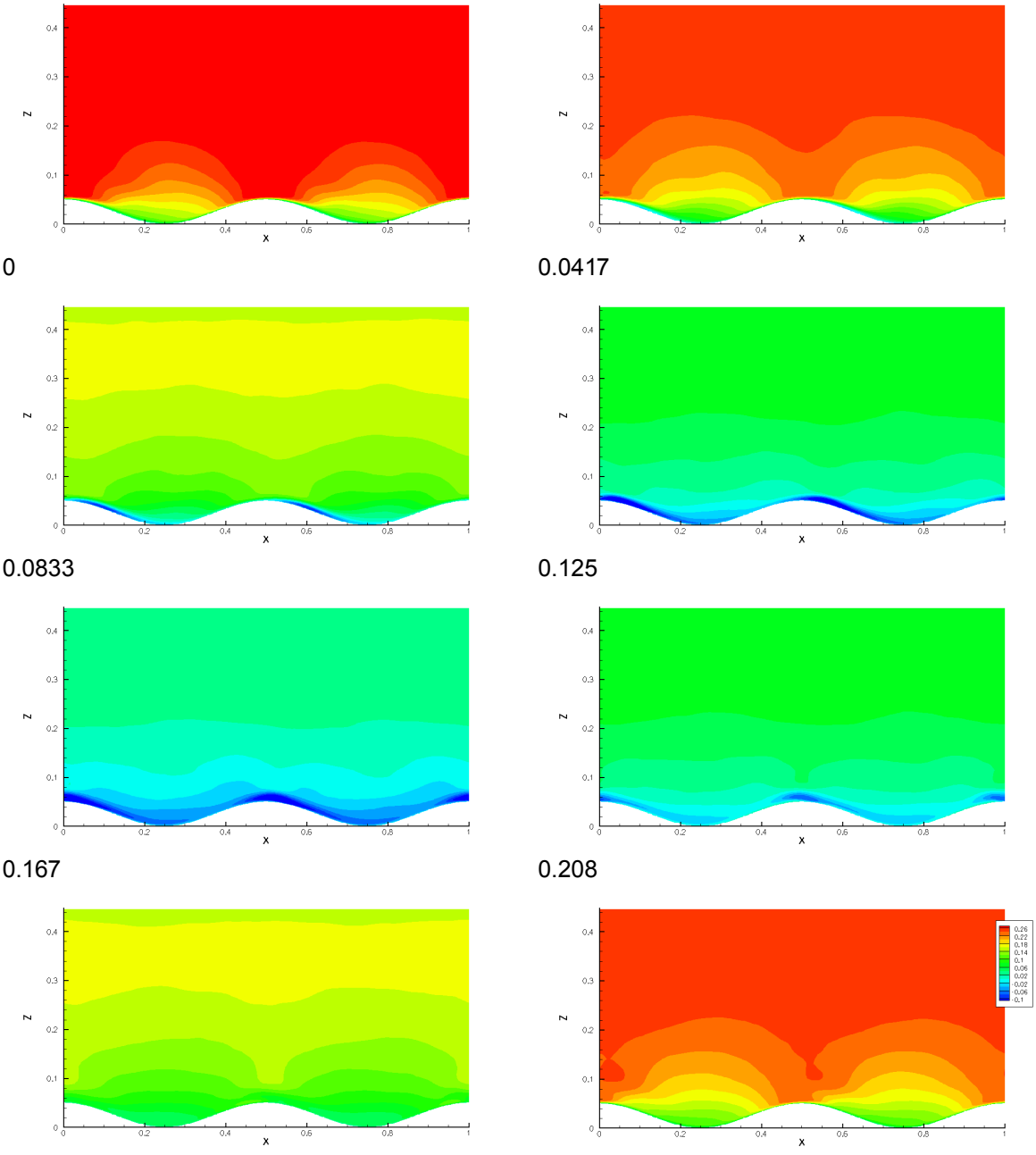

Figure 5.3 : RE_42 U_1 (phase and cross-channel average, 10 cycles; velocity range is from -0.1 ms^{-1} -blue- to 0.26 ms^{-1} -red). Mean flow is always positive (see Figure 4.1); strong negative values at the bottom of the domain from phase t=0.125 to t=0.208 indicate a counterflow region.

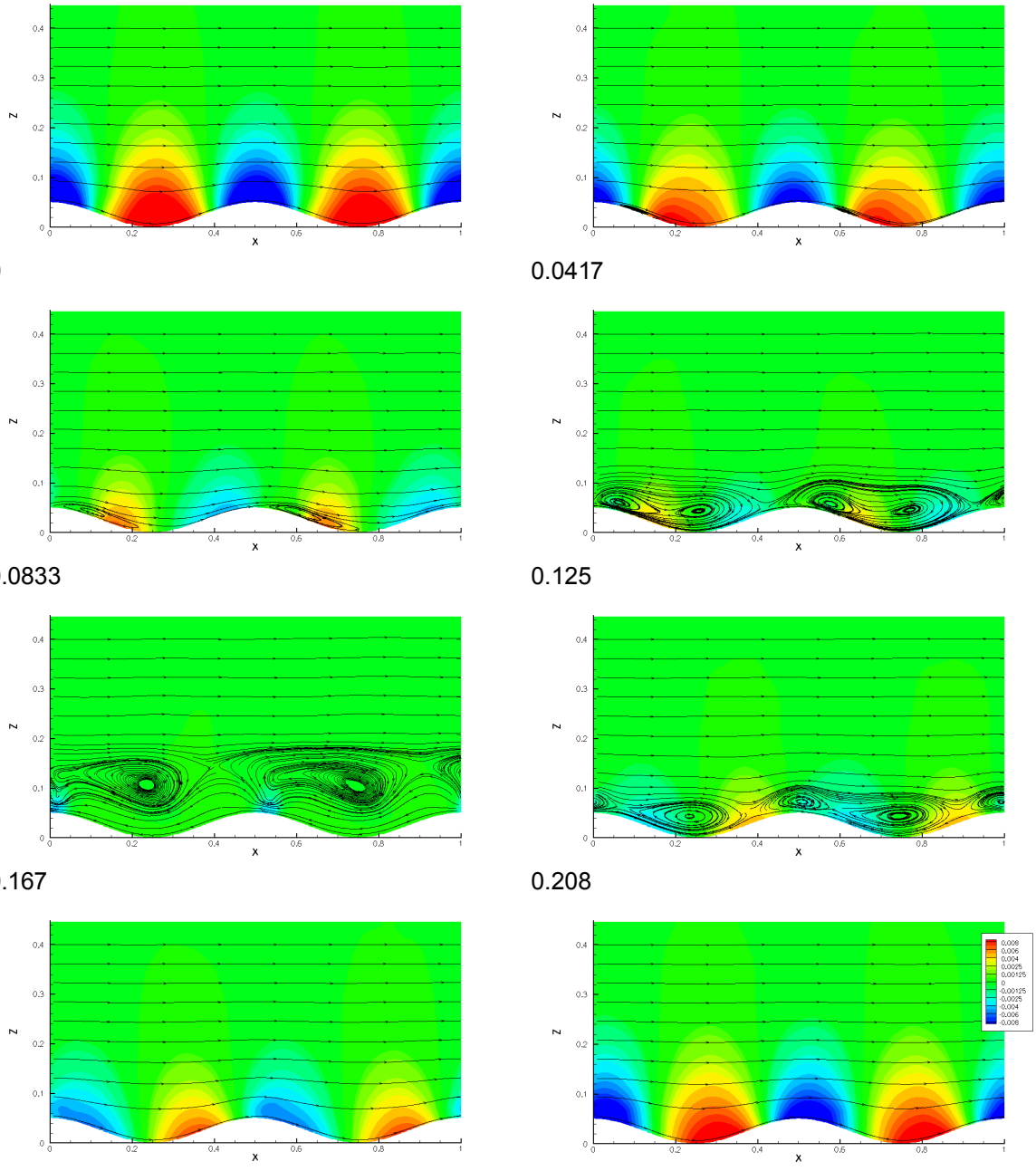

Figure 5.4 : RE_42 Pressure contours plus streamlines (phase and cross-channel average, 10 cycles; pressure range is -0.008 Pa -blue- to 0.008 Pa -red). Based on the streamlines pattern we can divide the flow evolution into two stages: first, from phase t=0.250 s to t=0, the streamlines follow the terrain and remain attached to the bottom. Starting at phase t=0.0417 s, a clockwise (positive) recirculation zone develops in the downstream side of the ripples; the zone grows until at phase t=0.0833 s it spans half the wave length of the ripples. At phase t=0.125 s, during the deceleration stage just before the mean longitudinal average velocity reaches its minimum, a second clockwise vortex is generated

above the ripple's through. Although difficult to distinguish in the plots, the recirculation vortex has then moved upwards to a pressure minimum located near the crests; the vortex system is twice as high as the ripples. At phase t=0.167 s, the vortices have been lifted by the background flow and they occupy almost half of the domain. Notice the strong deflection of the streamlines just downstream the crests due to the pressure minimum located there. At phase t=0.208 s, when the flow starts to accelerate, the vortices begin to reattach to the bottom. The crest vortex is again well defined and returns to the location of the local pressure minimum over the crest. Afterwards, in the middle of the acceleration stage (t=0.250 s), the plot shows that the flow has completely reattached to the bottom.

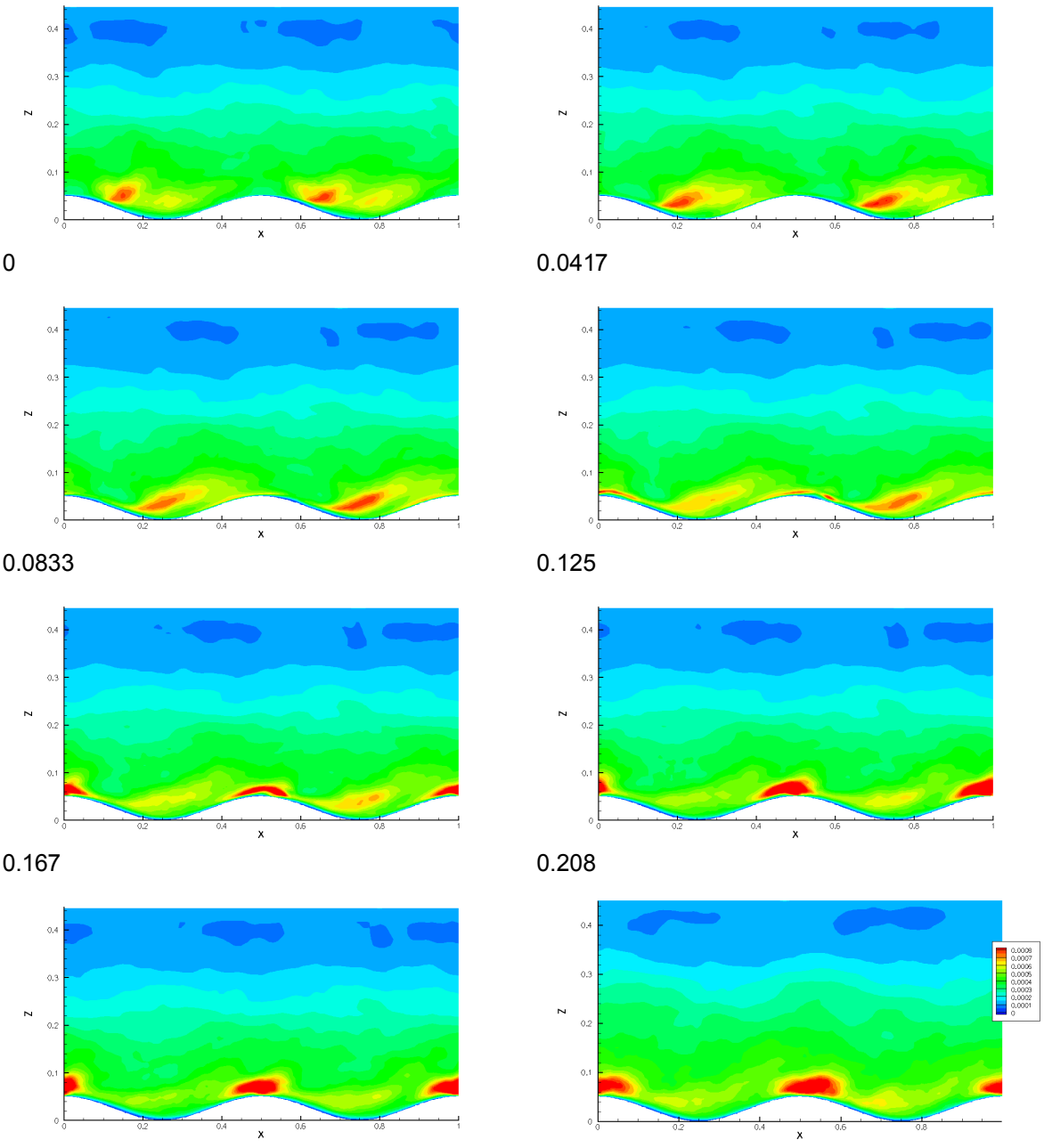

Figure 5.5 : RE_42 TKE evolution (phase and cross-channel average, 10 cycles; values range from 0.0 $m^2 s^{-2}$ -blue- to $8*10^{-4}$ $m^2 s^{-2}$ -red). The evolution of the TKE basically reflects that of its main contributor, the variability of the longitudinal velocity (not shown), although in phases t=0.250-0.293 s the vertical velocity signal (not shown) is discernible. Thus, we can identify two stages: TKE generation phase (from around t=0.0417 s to roughly t=0.208), which happens mainly on top of the crests, and a dissipation stage, which spans almost a complete period.

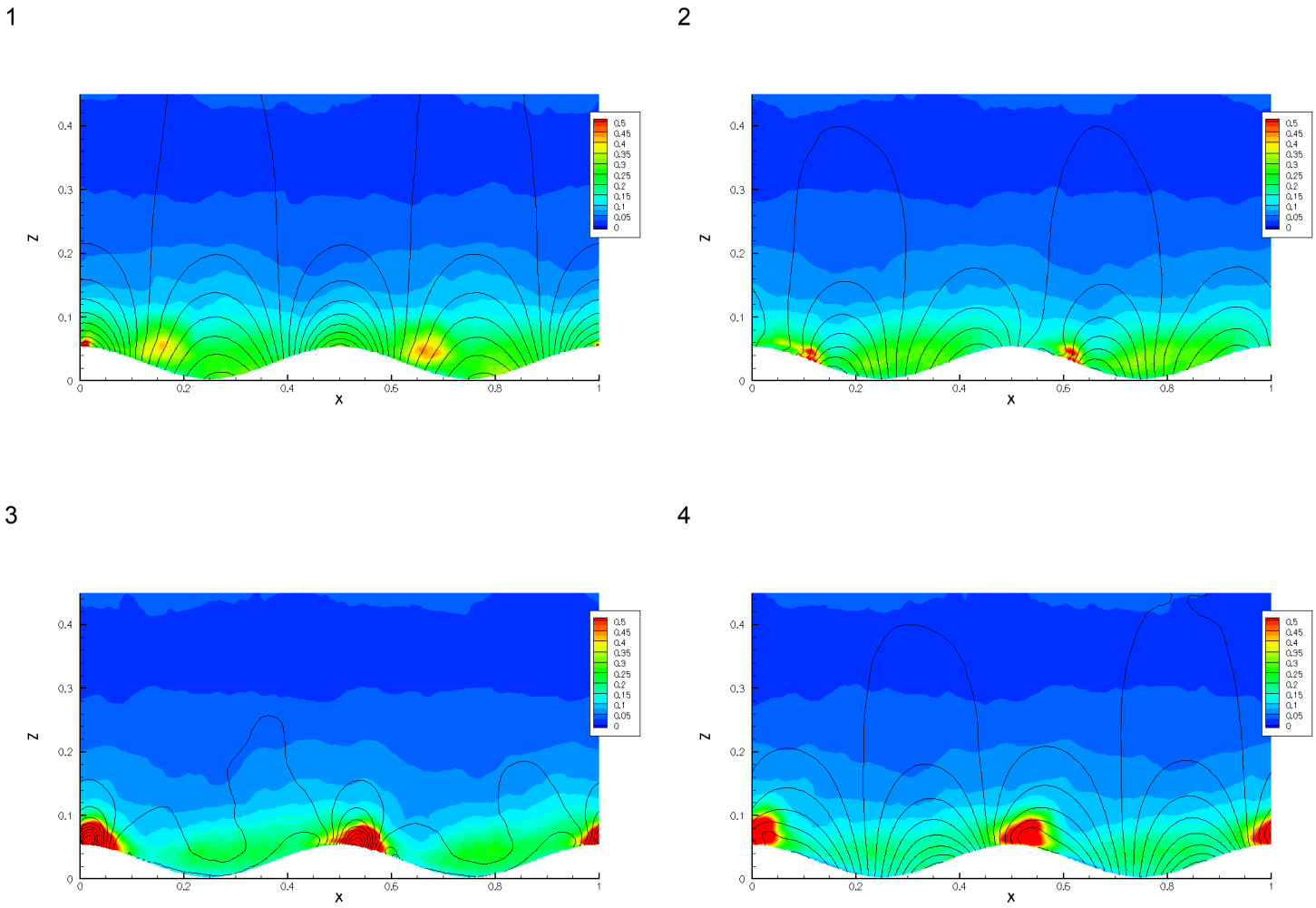

Figure 5.6 : Re42, Cross pressure gradient (phase and cross-channel average over 10 cycles, in color, range is 0 -blue- to 0.5 $Pam^{1.}$ For further details, see text)

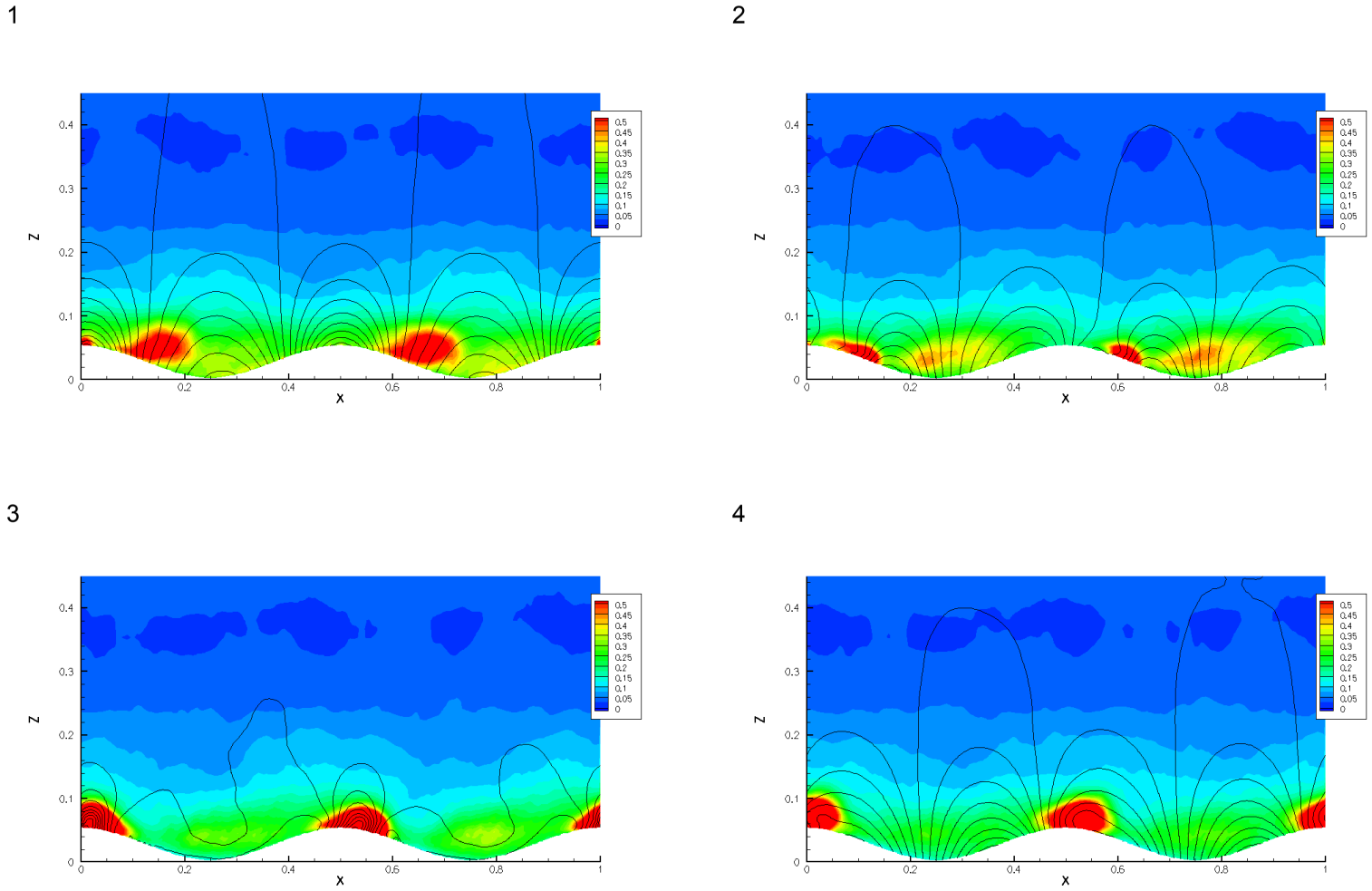

Figure 5.7 : Re42, Pressure gradient magnitude (phase andcross-channel average, in color, range is 0 -blue- to 10 Pam^{-1}. For further details, see text)

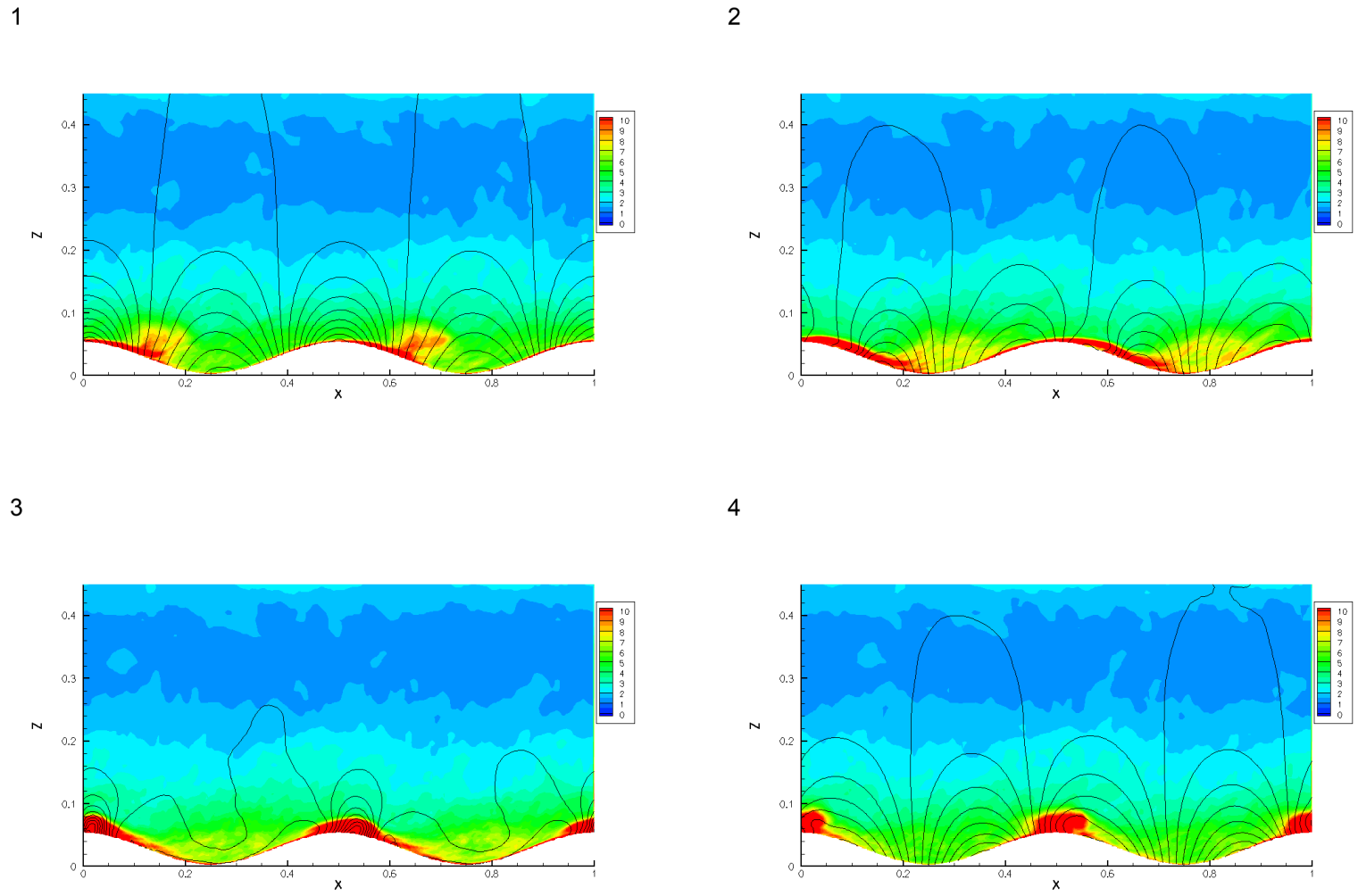

Figure 5.8 : Re42, Vorticity magnitude (phase and cross-channel average, in color, range is 0 -blue- to 10 s^{-1}. For further details, see text)

1

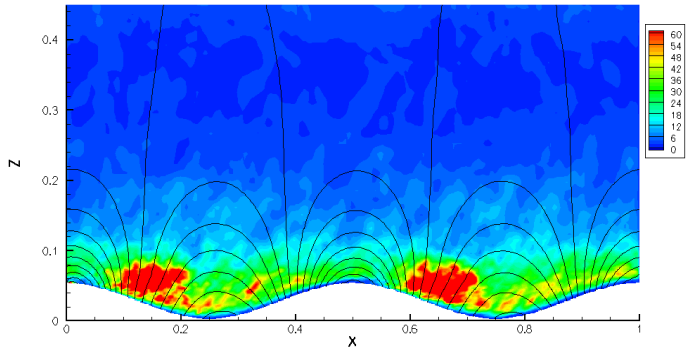

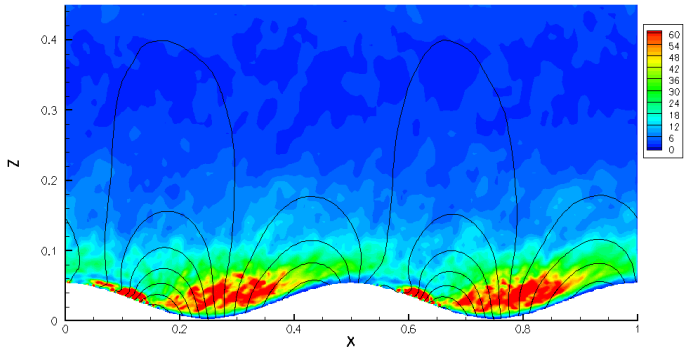

3

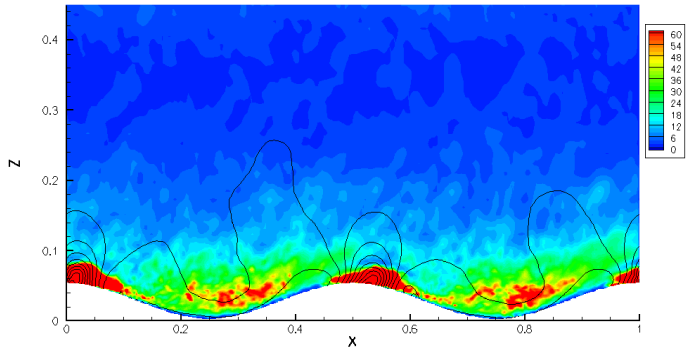

4

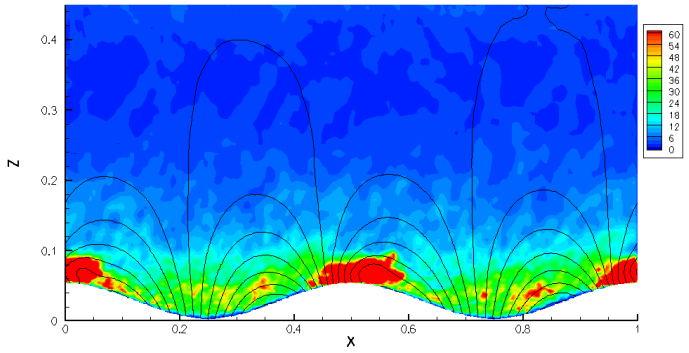

Figure 5.9 : Re42, Q (phase and cross-channel average, in color, range is 0 -blue- to 60 ms^{-1}. For further details, see text)

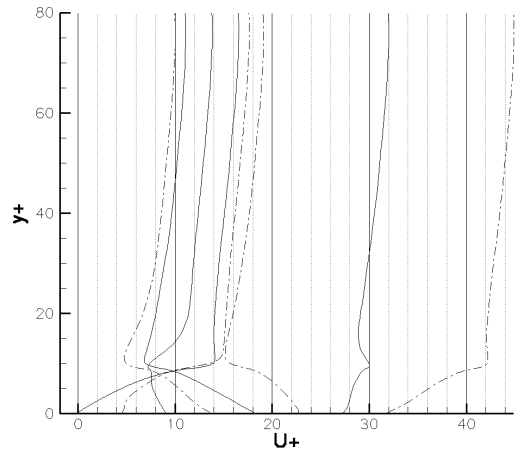

a

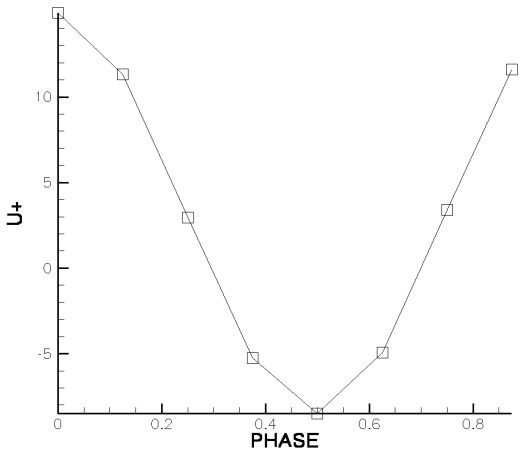

b

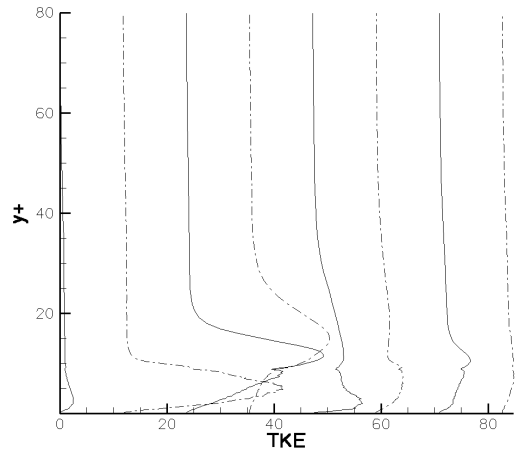

c

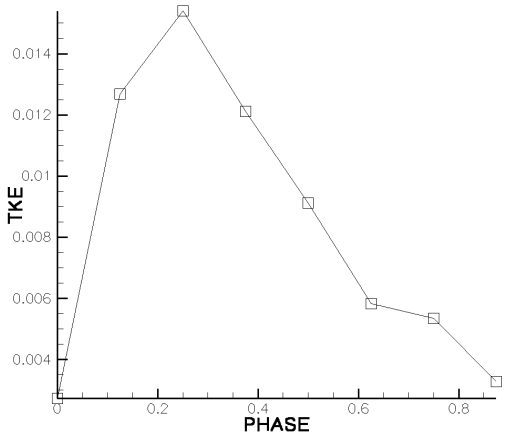

d

Figure 5.10 : Re150 (phase averaged, 10 cycles) a) Cross-channel averaged longitudinal velocity versus height. Velocity has been normalized with the friction velocity U_f and height has been normalized with l_s. The leftmost plot corresponds with phase t=0 and each consecutive phase has been displaced an amount $\Delta U^+=4.5$. Alternate line styles (continuous line versus dashed line) have no physical meaning and are used to increase legibility. b) Volume-averaged longitudinal velocty versus phase. Velocity has been normalized using the friction velocity. c) ross-channel averaged TKE versus height. TKE has been normalized using the square of the friction velocity. Each consecutive phase has been displaced an amount $\Delta TKE=11$. For other details refer to commentaries in figure a). d) Volume averaged TKE versus phase.

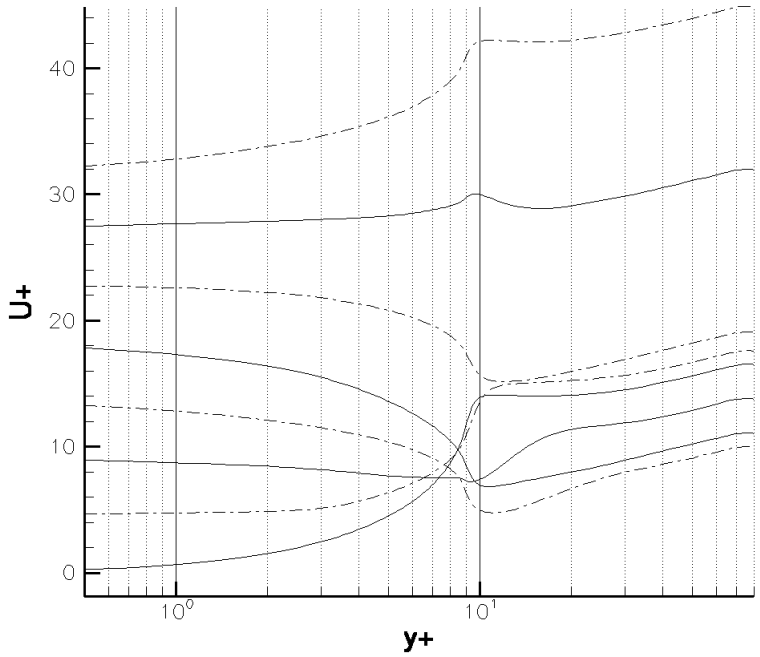

Figure 5.11 : Re150 (phase average, 10 cycles) Evolution of the cross-channel averaged longitudinal velocity versus normalized height. Velocity has been normalized using the friction velocity U_f and height using l_s. Notice logarithmic scale for y^+. The lowermost profile corresponds to phase t=0 and each consecutive profile has been displaced upwards an amount $\Delta U^+=4.5$. Differences in line style (solid line versus dashed line) have no physical relevance and are for the sole purpose of legibility.

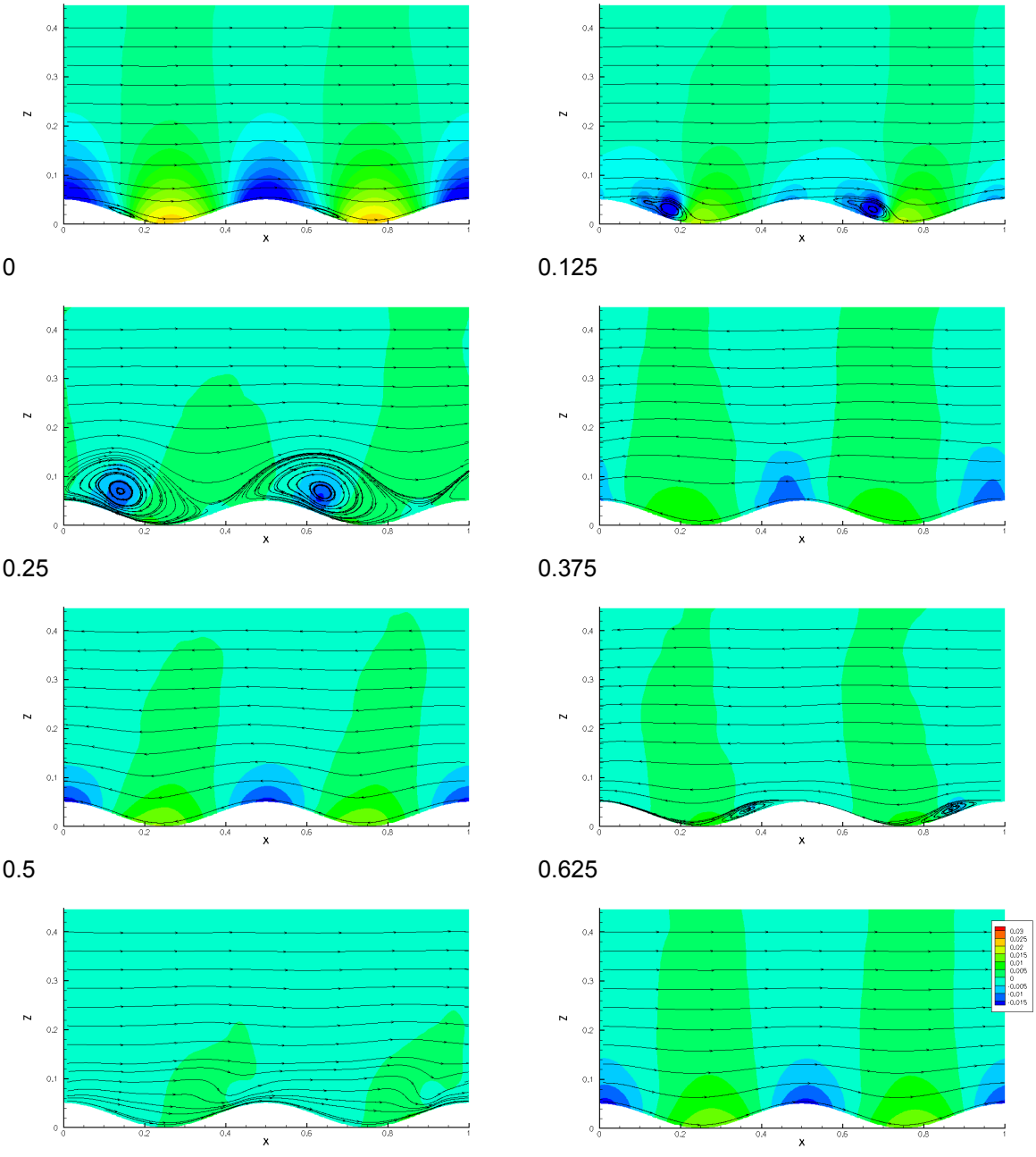

Figure 5.12 : RE_150 pressure and streamlines (phase and cross-channel average over 10 cycles). Notice the correspondence between pressure minima and closed streamlines especially in t= 0.25 s, t= 0.625 s and t= 0.125 s. The streamlines also make clear the extent and evolution of the separation zones. A feeble, small separation zone is located at the downstream (left) side of the ripples at t= 0.625 s (just before the flow inversion) and it spans a bit less than half the wavelength of the undulations. A larger and longer-lasting one is discernible from t= 0 s to t=0.125 s. The separation starts during the velocity and pressure gradient maximum at t=0 s, spanning about a quarter of the length of the ripple. It grows rapidly until, just one time step later at t= 0.125 s, the flow is almost being

deflected higher than the ripple elevation. At that instant the pressure minima have been displaced to the right side of the ripples and the pressure maxima in the troughs have disappeared. This situation is extremely unstable: at t=0.25 s the circulation pattern is completely detached from the boundary and two big vortices have formed. Those vortices are about three times as high as the ripples and occupy almost the complete length of the undulations. The axis of the vortices are almost perfectly centered at the pressure minima.

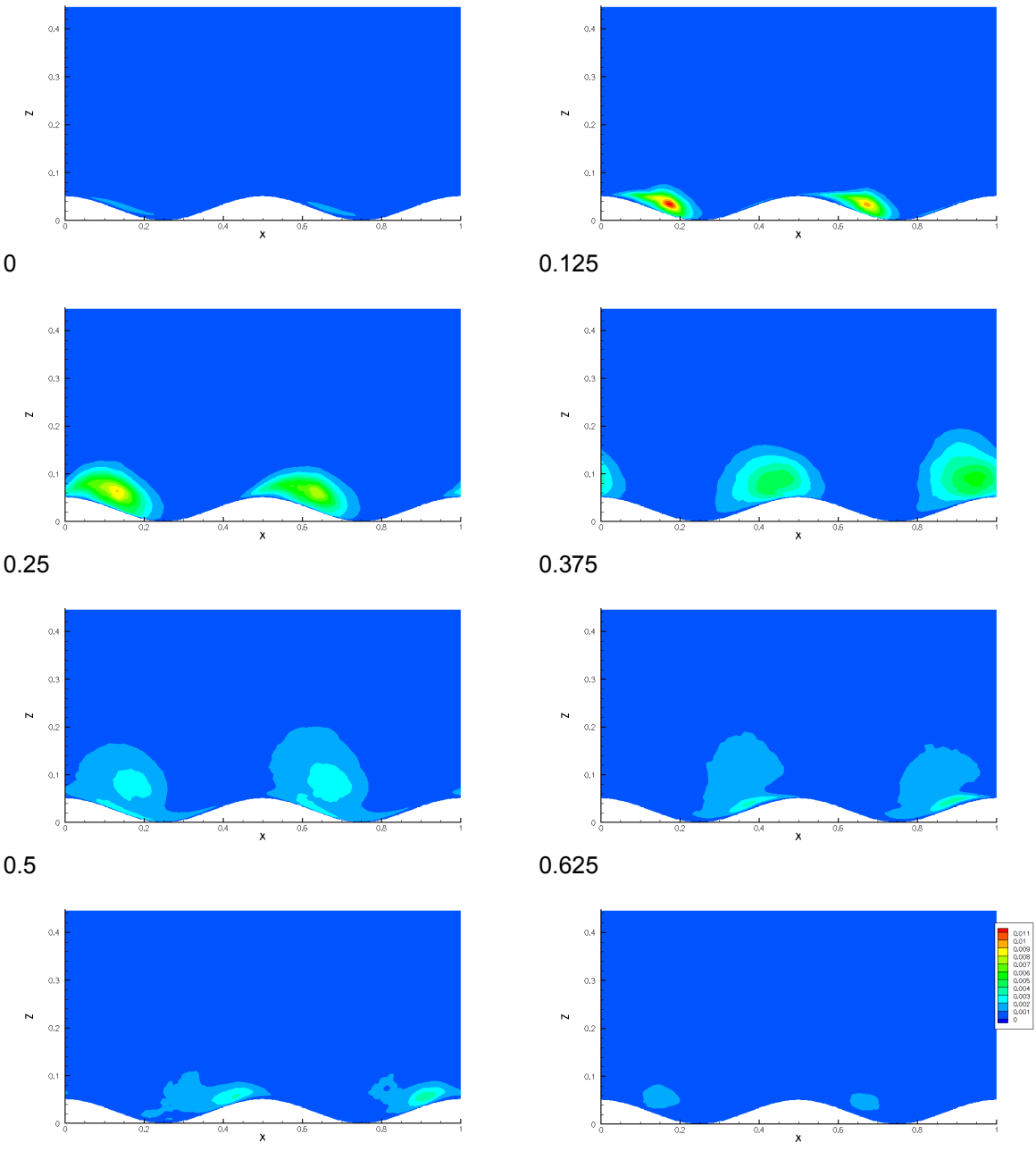

Figure 5.13 : RE_150 TKE; phase and cross-channel average over 10 cycles. Generation of most of the TKE starts at t=0.125 s, shortly after the velocity maximum, inside the recirculation zone. The high kinetic energy region then moves with the vortices at t=0.25 s and dissipates gradually until, at t=0.625 s, only a weak shadow remains. A much weaker generation episode happens between t=0.5 s and t=0.625 s during the second, feebler, separation stage. The maximum of TKE is located at about two thirds of the ripple height during its generation and drifts even higher during the vortex detachment at t= 0.25 s. The upper limit of the high energy "bubble" reaches an elevation about two times the ripple height before complete dissipation. The energy peak coincides with the pressure minimum (t=0.375-0.625 s).

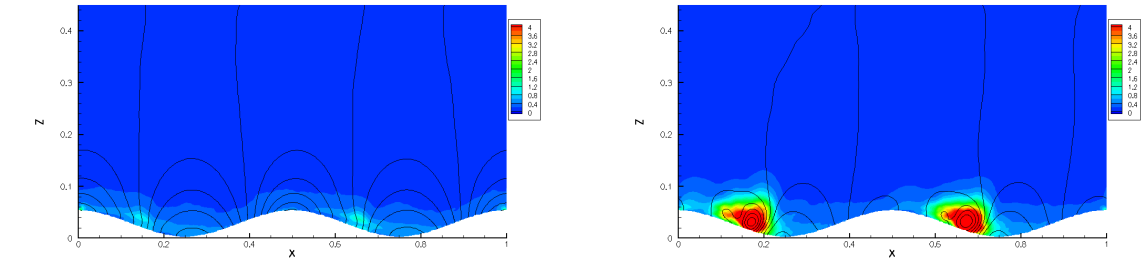

0

0.125

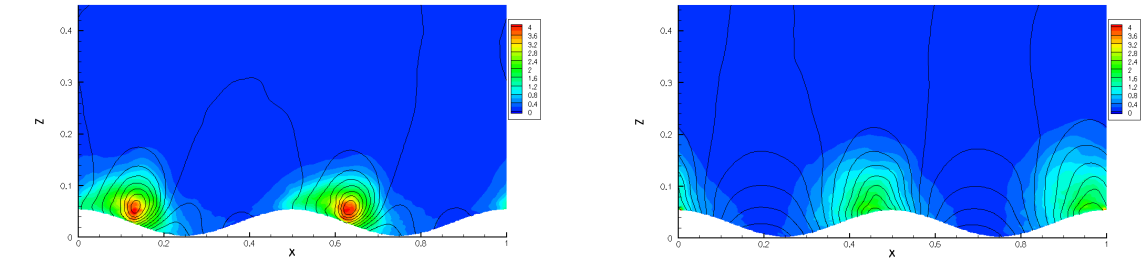

0.250

0.375

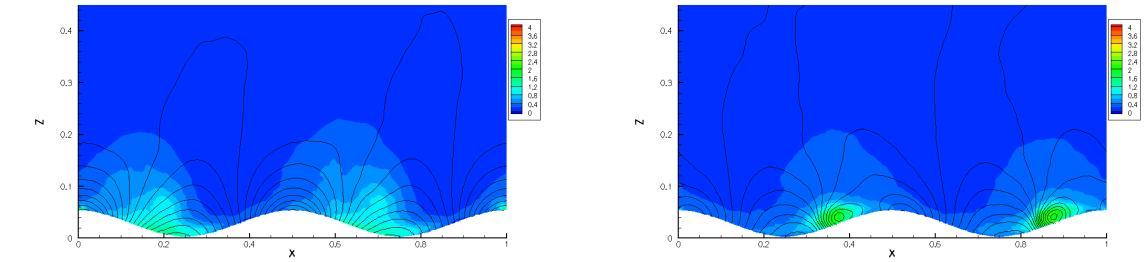

0.500

0.625

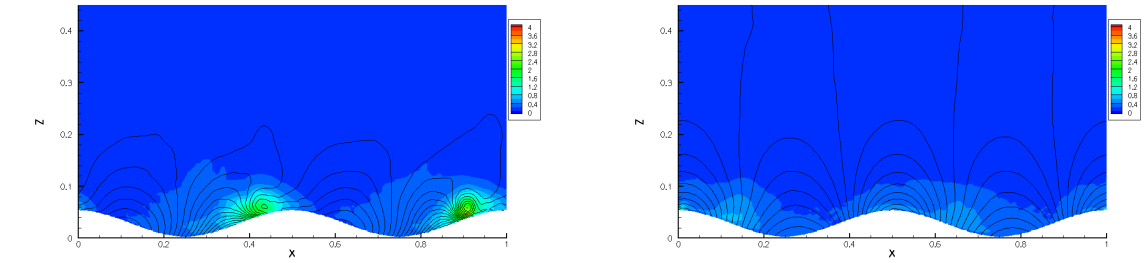

0.750

0.875

Figure 5.14 : Re150, Cross pressure gradient (phase and cross-channel average over 10 cycles, in color, range is 0 to 4 Pam^{-1}). See main text for further details.

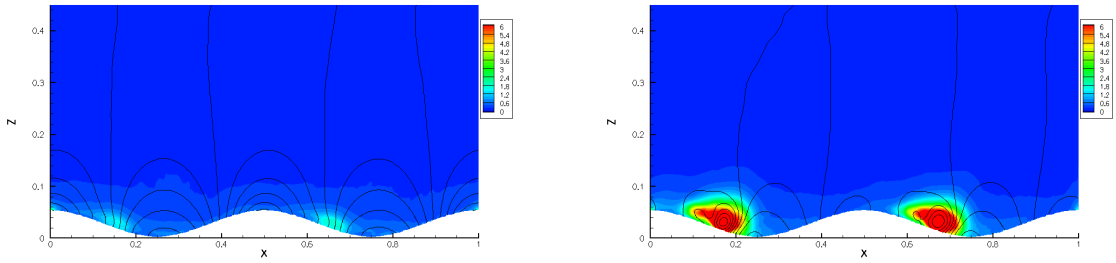

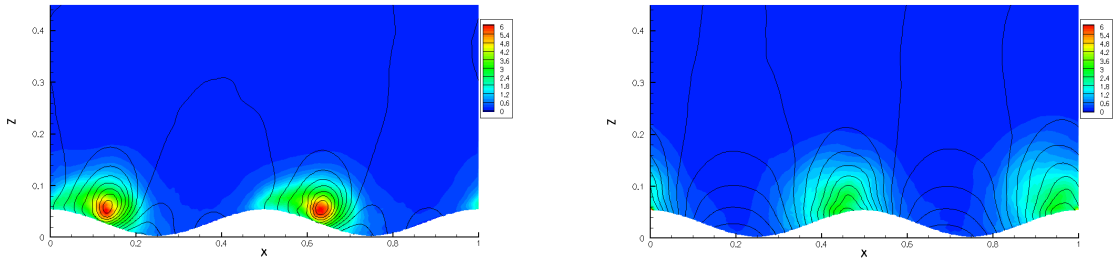

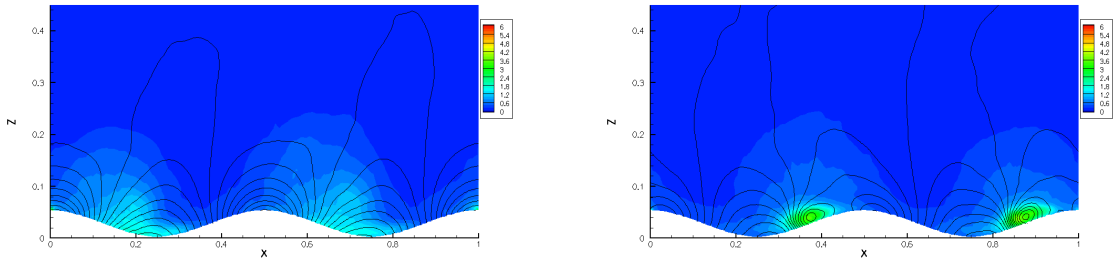

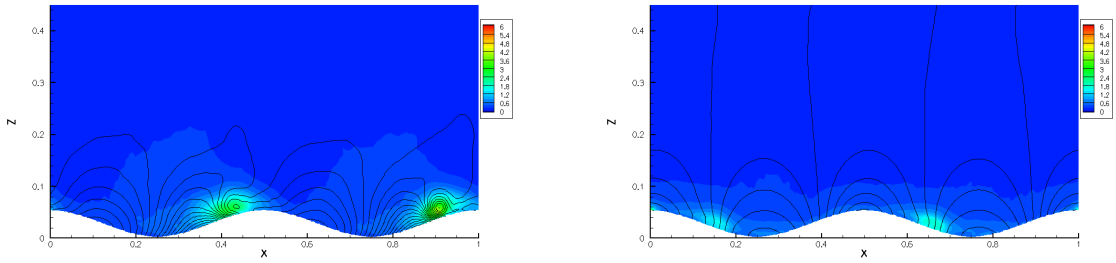

Figure 5.15 : Re150, Pressure gradient magnitude (phase and cross-channel average over 10 cycles, in color, range is 0 to 6 Pam^{-1}). See main text for further details.

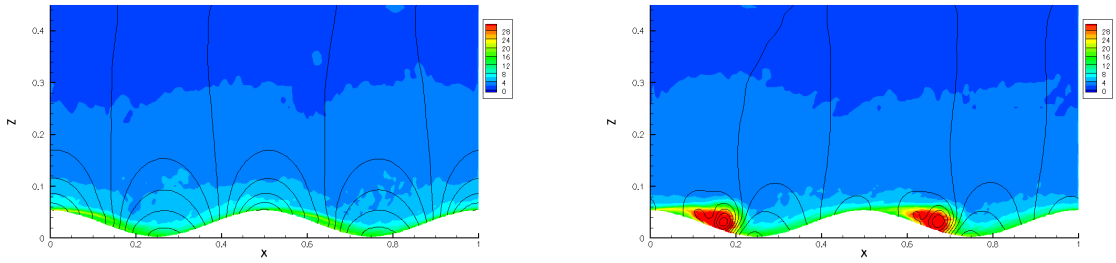

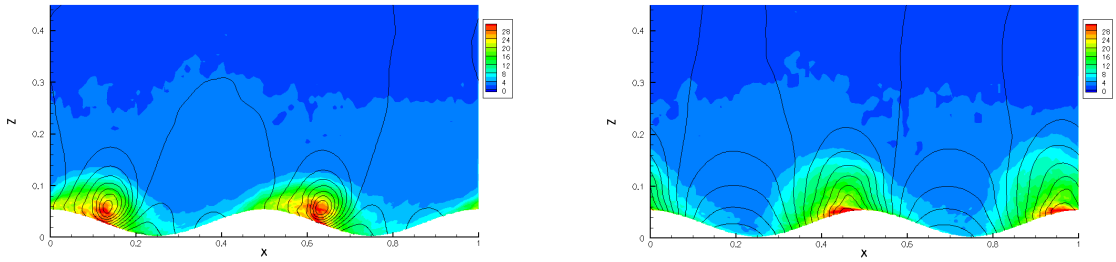

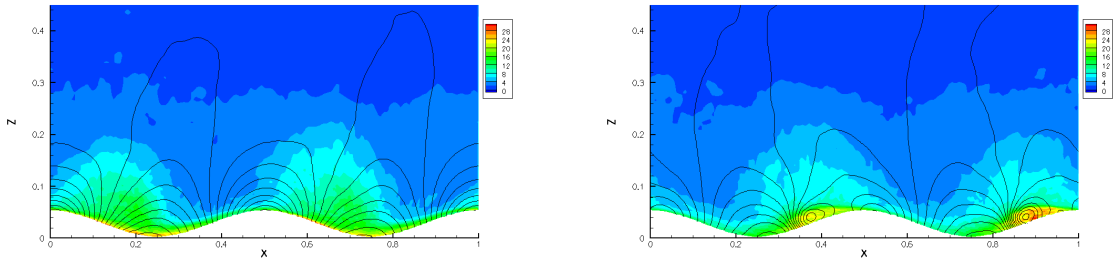

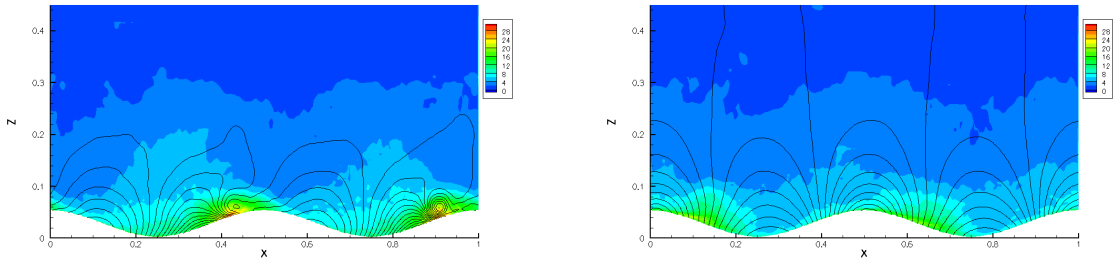

Figure 5.16 : Re150, Vorticity magnitude (phase and cross-channel average over 10 cycles, in color, range is 0 to 30 s^{-1}). See main text for further details.

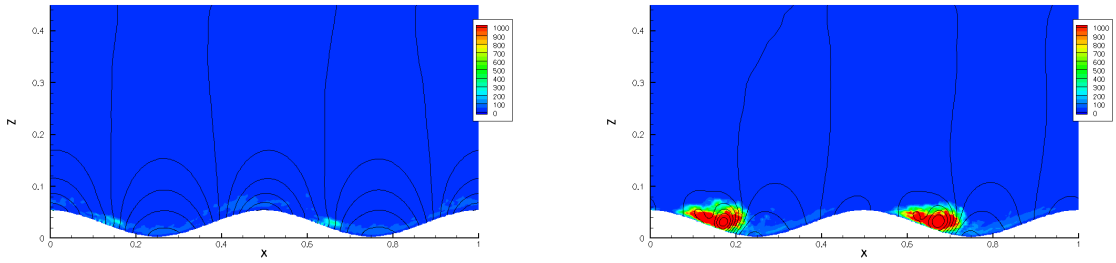

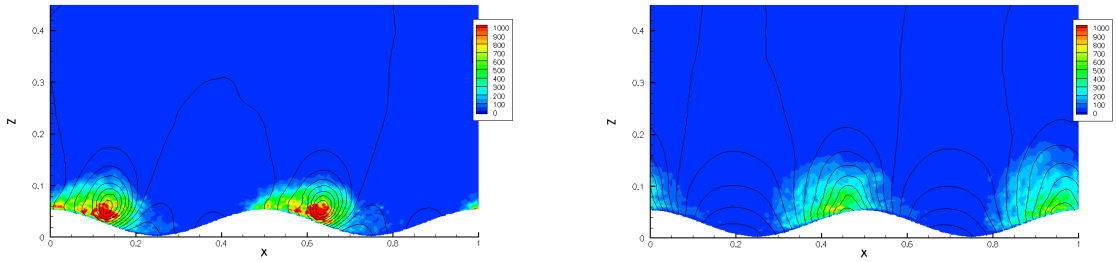

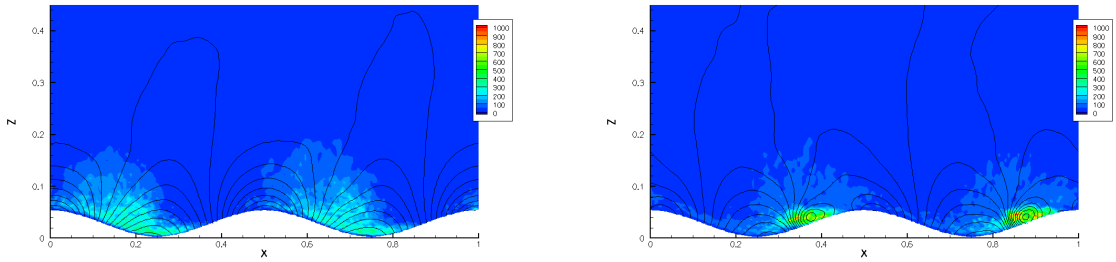

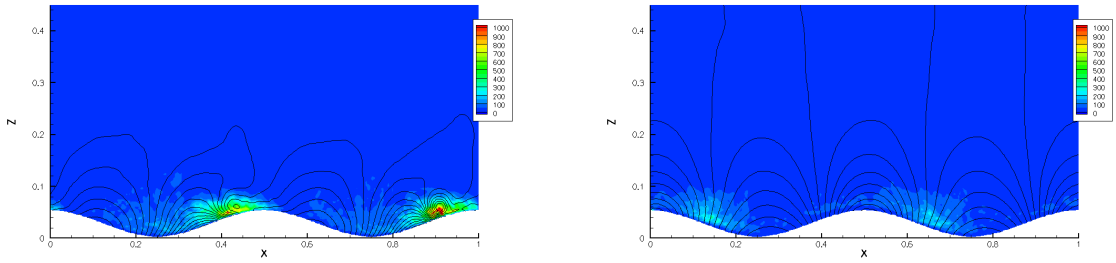

Figure 5.17 : Re150, Q values (phase and cross-channel average over 10 cycles, in color, range is 0 to 1000 s^{-1}). See main text for further details.

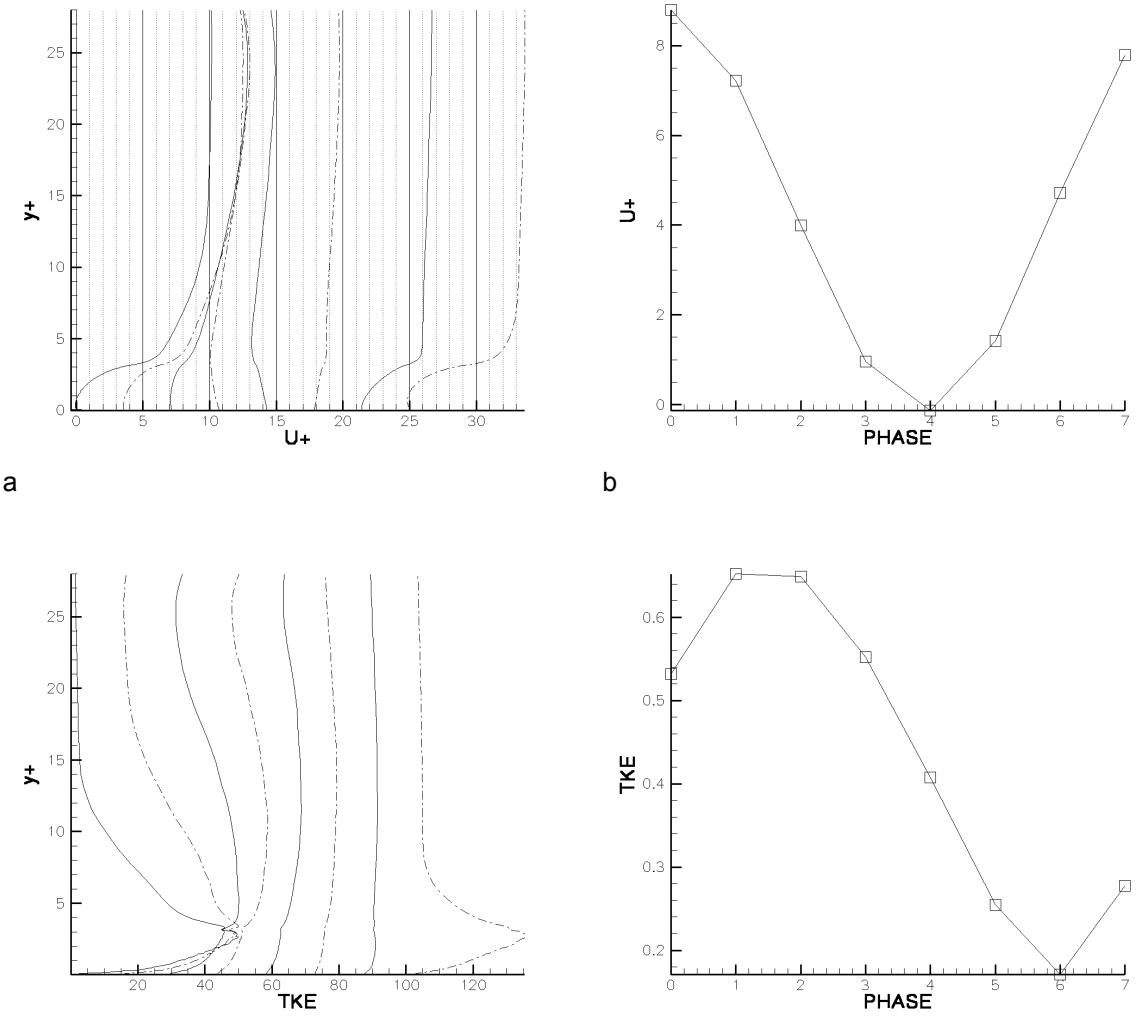

Figure 5.18 : Re210 (phase average, 10 cycles). a) Cross-channel averaged longitudinal velocity versus height. Velocity has been normalized with the friction velocity U_f and height has been normalized with l_s. The leftmost plot corresponds with phase t=0 s and each consecutive phase has been displaced to the right an amount $\Delta U^+=3.57$. Alternate line styles (continuous line versus dashed line) have no physical meaning and are used to increase legibility. b) Volume-averaged longitudinal velocity versus phase. Velocity has been normalized using the friction velocity. Flow reversal happens at t=4 s. c) Cross-channel averaged TKE versus height. TKE has been normalized using the square of the friction velocity. Each consecutive phase has been displaced an amount $\Delta TKE=12.75$. For other details refer to commentaries in figure a). Notice the TKE peak at the ripples' height from phase t=7 s to t= 1 s. d) Volume-averaged TKE versus phase. The TKE peak happens at some point between phase t=1-2 s, coincidental with the beginning of the deceleration stage (see figure b); minimum occurs at t=6 s, in the middle of the acceleration stage.

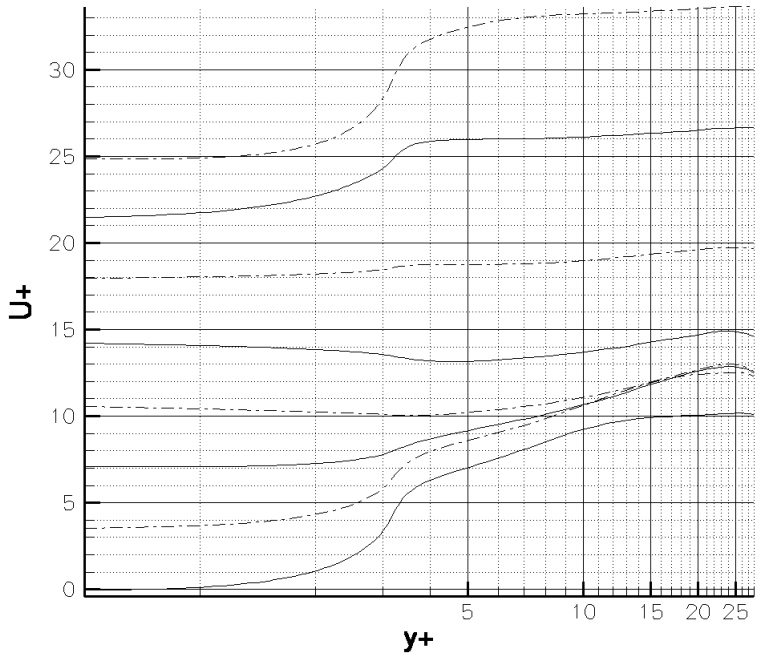

Figure 5.19 : Re210 (phase average, 10 cycles) Evolution of the cross-channel averaged longitudinal velocity versus normalized height. Velocity has been normalized using the friction velocity U_f and height using l_s. Notice logarithmic scale for y^+. The lowermost profile corresponds to phase t=0 and each consecutive profile has been displaced upwards an amount $\Delta U^+=3.6$.

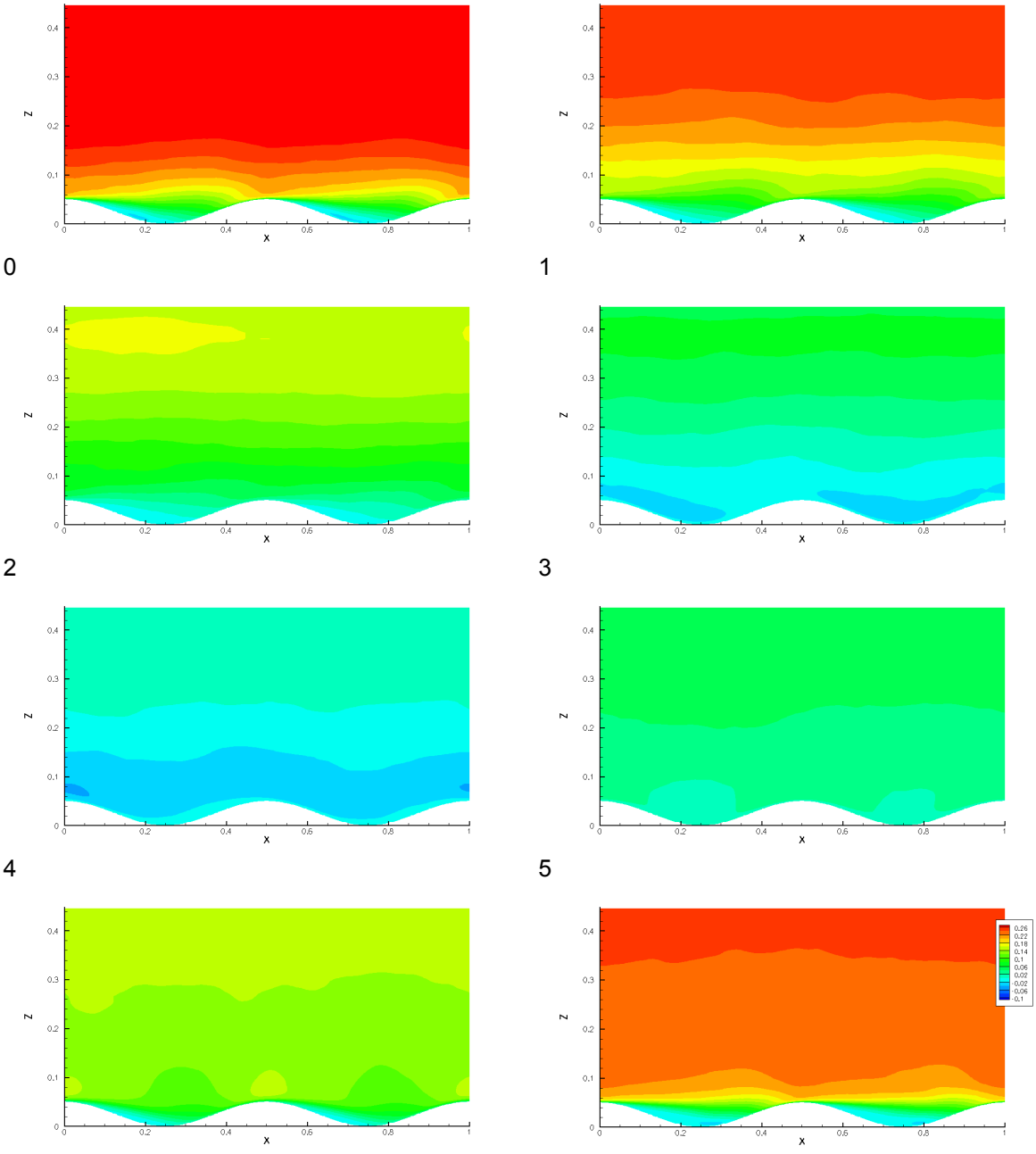

Figure 5.20 : Re_210 Cross-channel averaged U_1 contours (phase average, 10 cycles; velocity range is from -0.1 -blue- to 0.26 -red- ms^{1}). Flow reversal happens at t=4 s; separation is evident and occurs for more than half the cycle, from t=6 to t=2 and also (although almost indistinguishable) for a brief instant in t=4. Notice also that in the acceleration phase (t=7 to t=0) changes in the extent of the recirculation zone are small (as can be more clearly seen in the streamlines plot below).

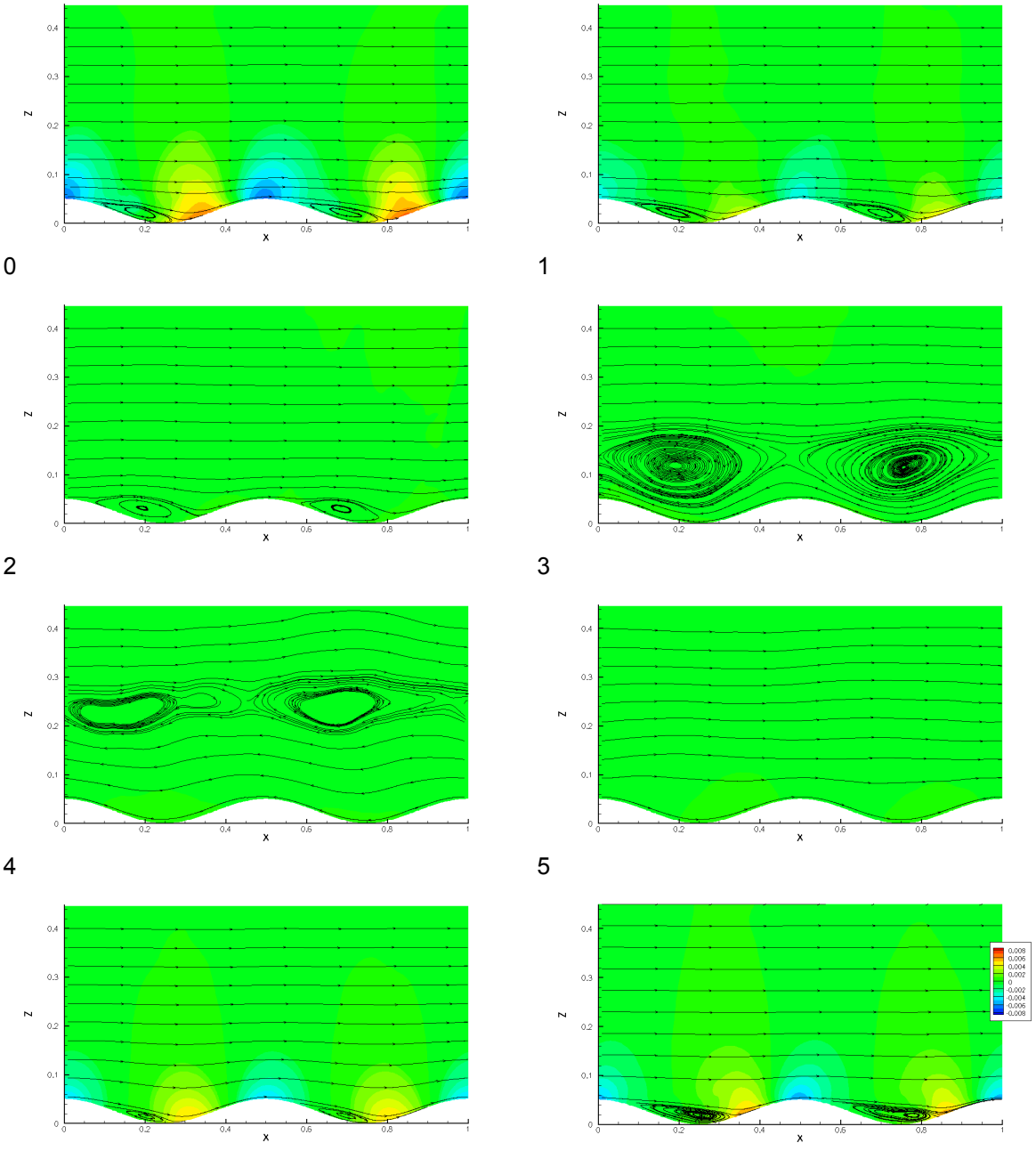

Figure 5.21 : Re_210 pressure contours plus streamlines (phase average, 10 cycles; pressure range is from -0.008 -blue- to 0.008 -red- Pa). The streamlines show two main different stages in the flow. In the separation state, t=6 to t=2, flow is from left to right; there is a clearly defined and strong recirculation zone downstream of the ripples that occupies the largest fraction of the through. The separation zone is generated at t=6 after the flow reversal and growths until achieving a relatively stable state at t=2 during the later stages in the acceleration phase, right before the velocity maximum. The second flow stage happens from t=3 to t=4 and it is characterized by a flow reversal and a major change in the flow topology. The reversal generates two vortices centered above the troughs and the

corresponding saddle points between the vortices almost exactly above the crests. The vortices form a boundary between the upper zone with positive longitudinal velocity and the lower countercurrent. Also, barely discernible at t=4 is the first indication of a possible flow separation rapidly quelled by the inflection in the sign of the background flow.

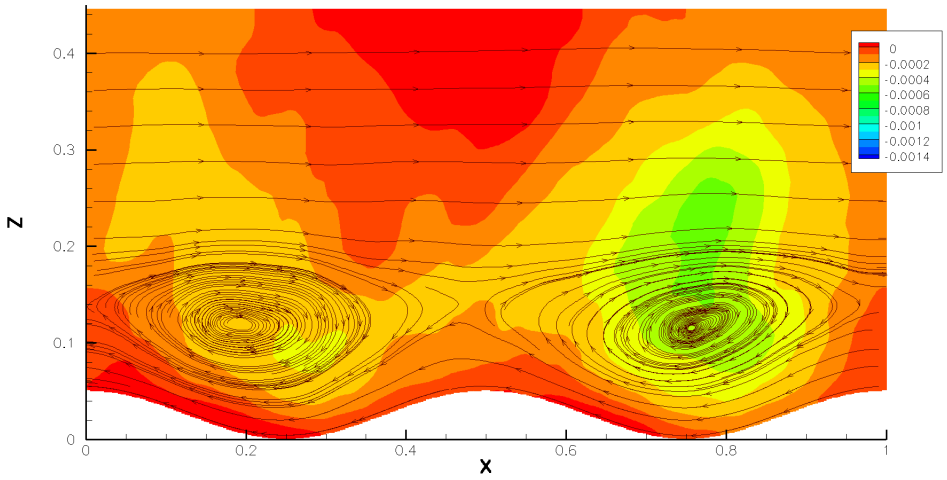

Figure 5.22 : A blowup of the average pressure field and streamlines for Re210 at t=3 (phase average, 10 cycles). Notice that pressure scale is different from the figure above. The vortex characteristics and its relation with the pressure field become clear in this figure. The vortex center is located at almost two and a half times the ripples' height from the bottom (z=0). The vortices' vertical dimension is about 4 times α_{wall} and half the wavelength of the ripples lengthwise. Observe the well defined, almost closed streamlines and the two saddle points located above the crests.

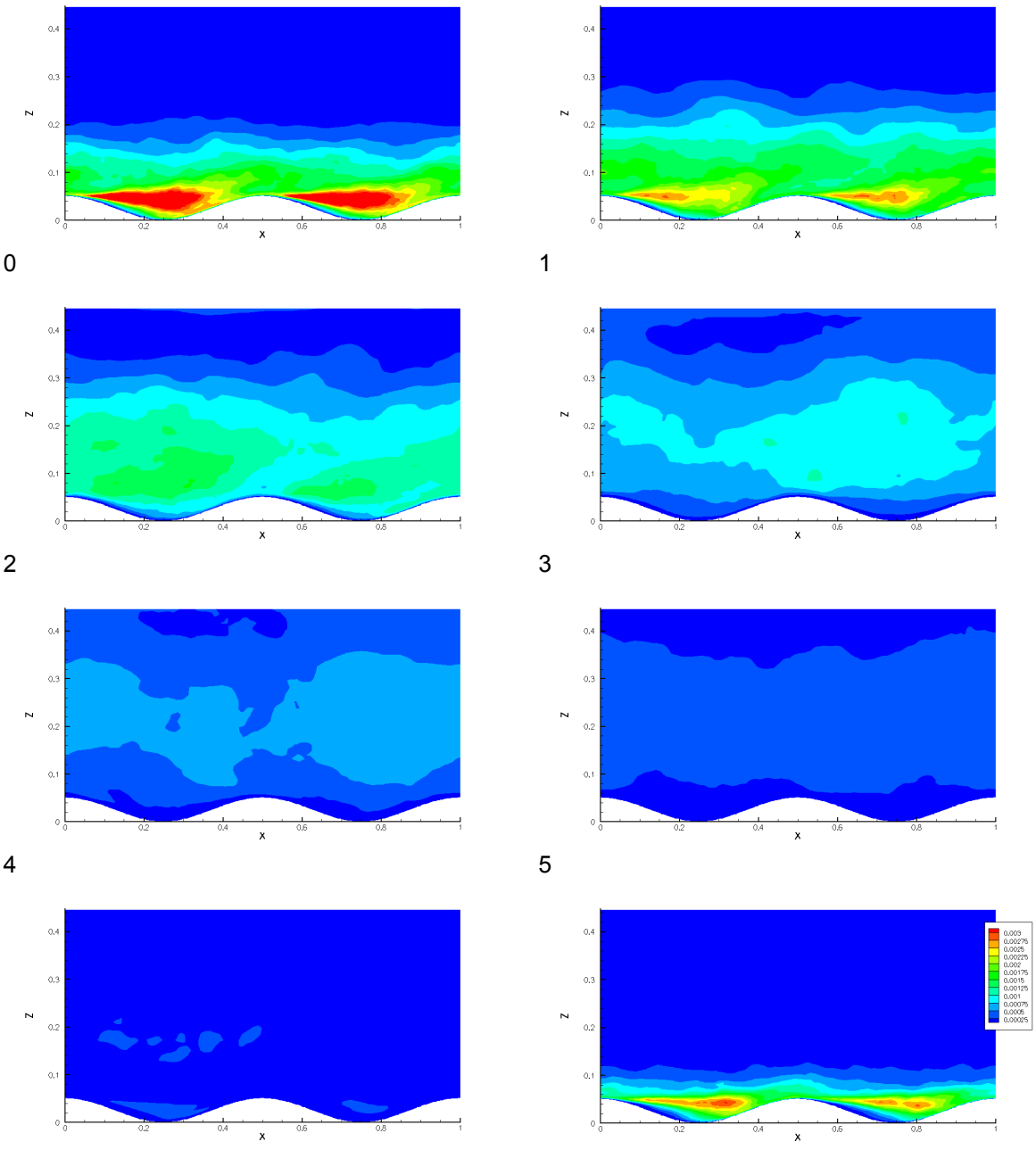

Figure 5.23 : Re_210 Cross-channel averaged TKE (phase average, 10 cycles; range is from 0 -blue- to 0.0018 m^2s^{-2} -red).

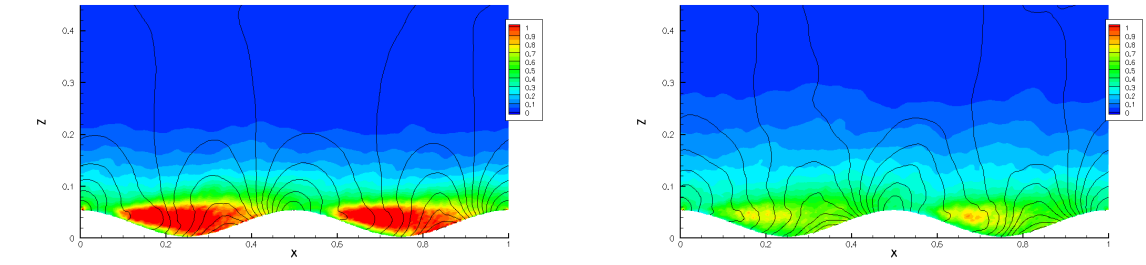

0

1

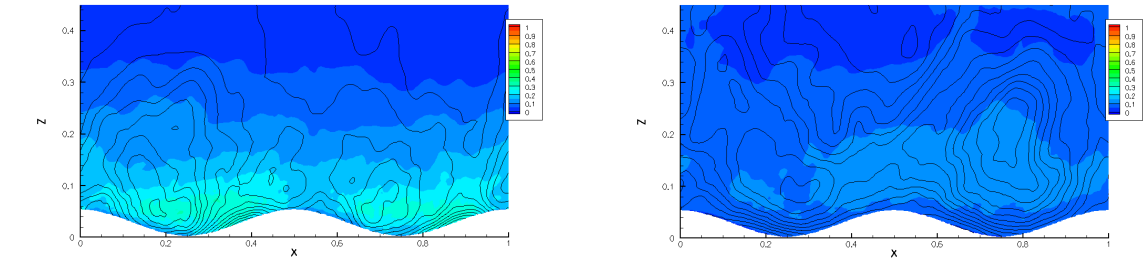

2

3

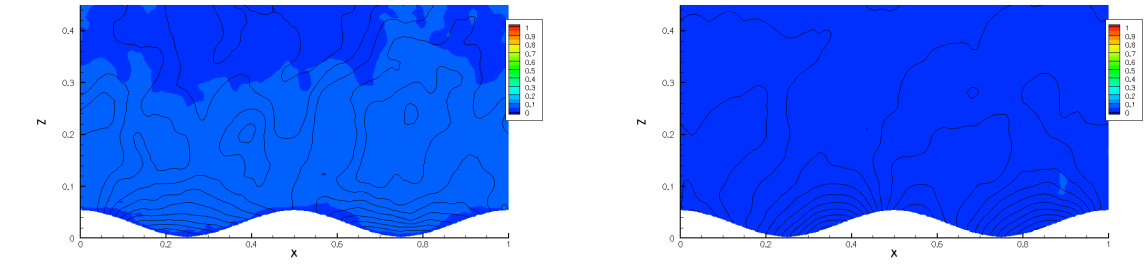

4

5

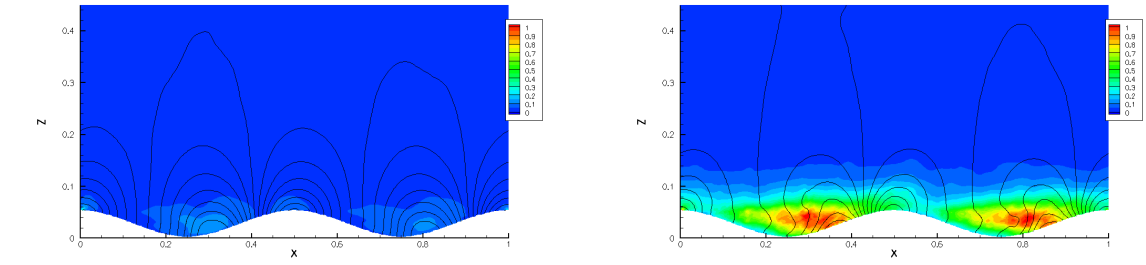

6

7

Figure 5.24 : Re 210 Cross-channel averaged cross pressure gradient (phase average, 10 cycles; in color, range is 0 -blue- to 1 -red- Pam^{-1})

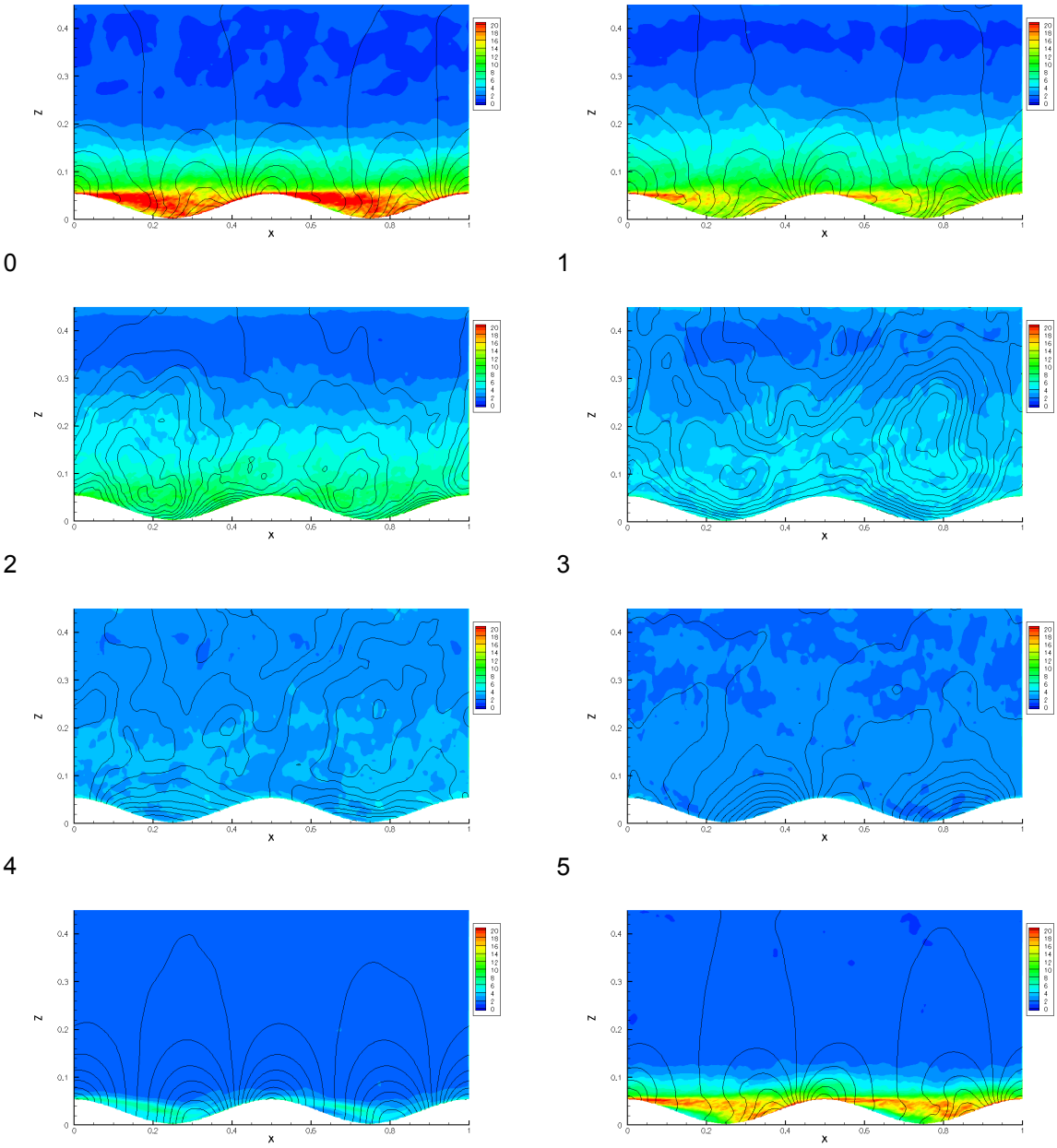

Figure 5.25 : Re 210 Cross-channel averaged vorticity magnitude (phase average, 10 cycles; in color, range is 0 -blue- to 20 -red- s^{-1})

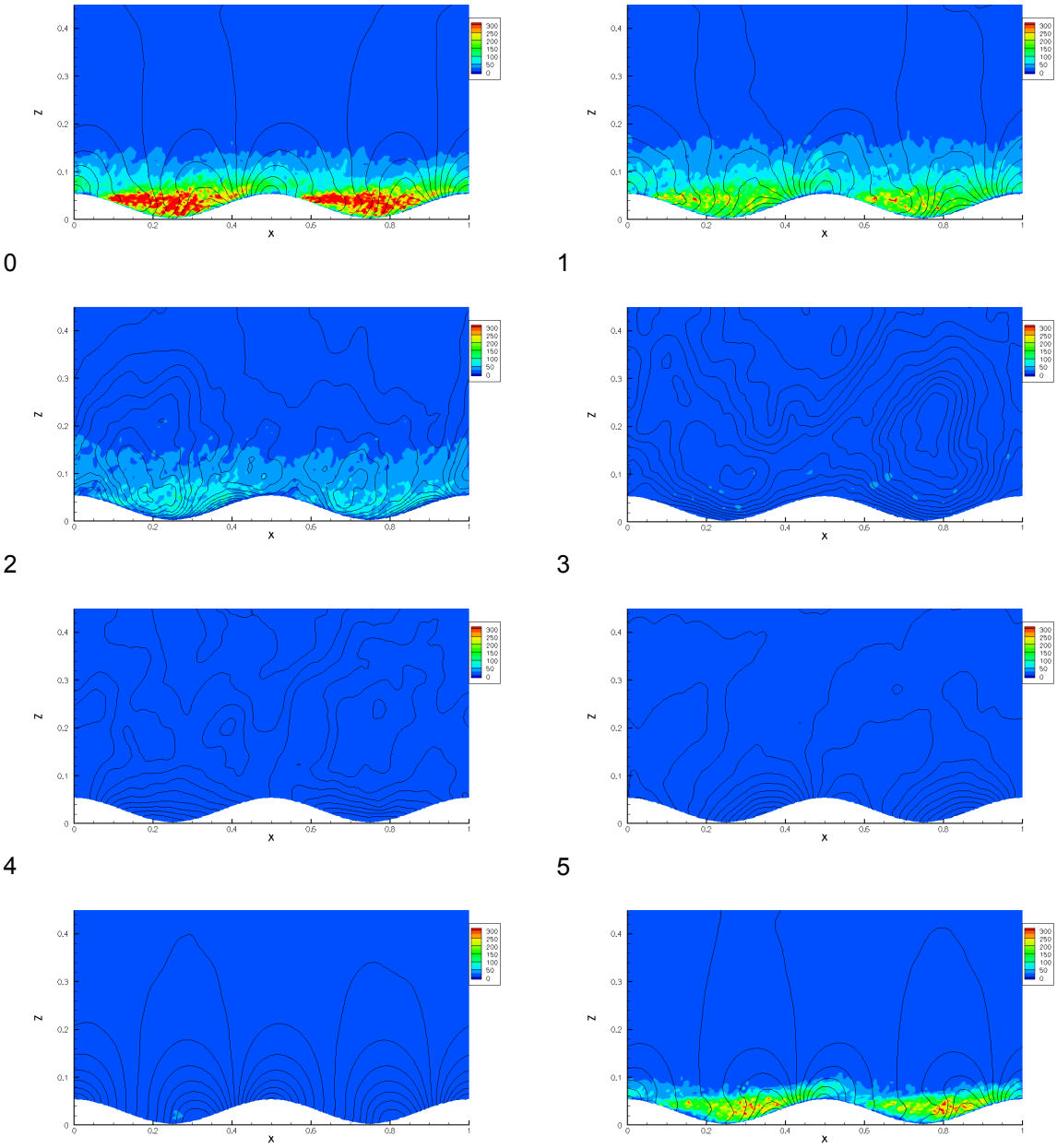

Figure 5.26 : Re 210 Cross-channel averaged Q contours (phase average, 10 cycles; in color, range is 0 -blue- to 400 -red- s^{-1})

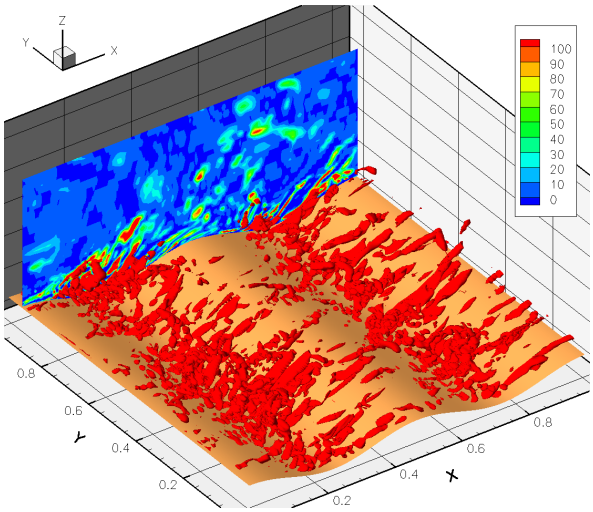

0.0417

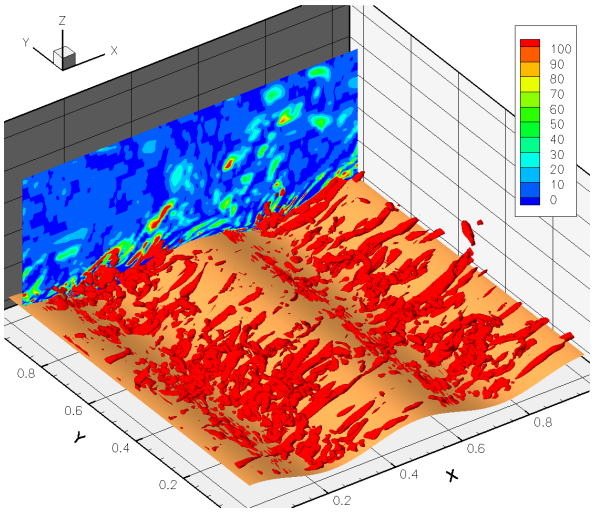

0.0833

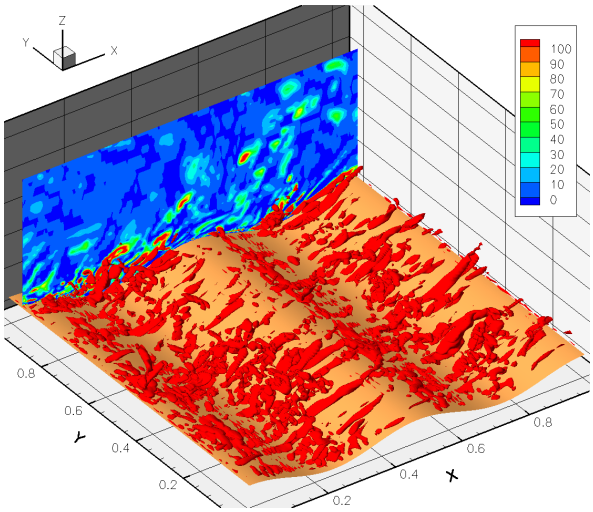

0.125

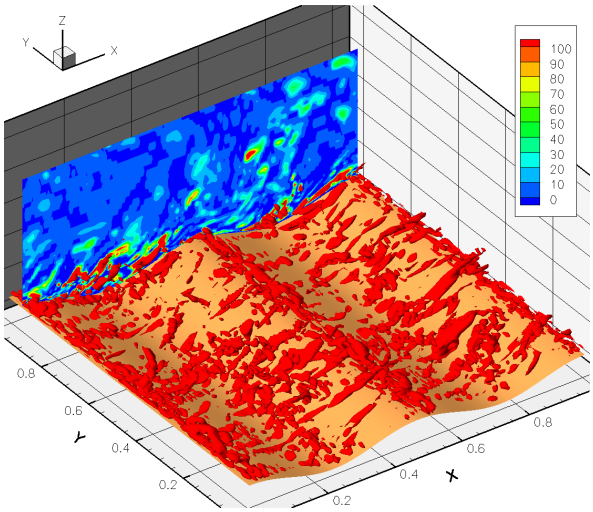

0.167

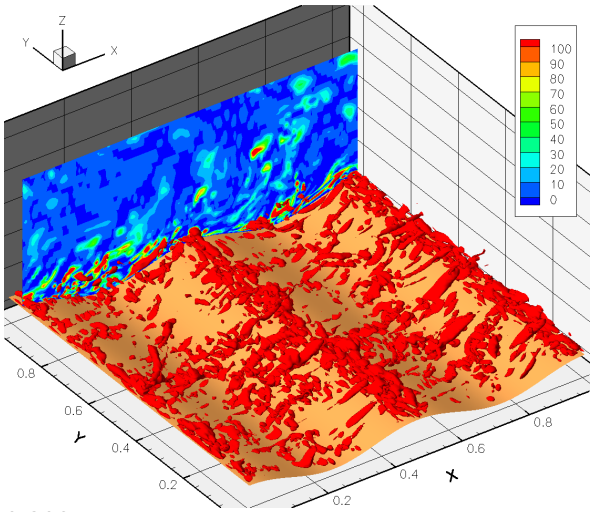

0.208

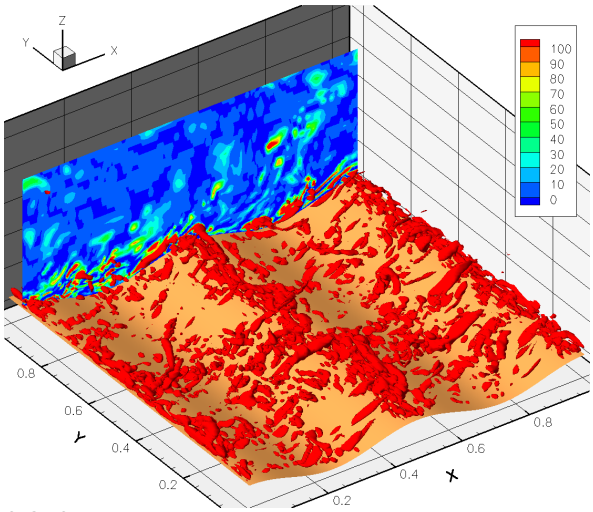

0.250

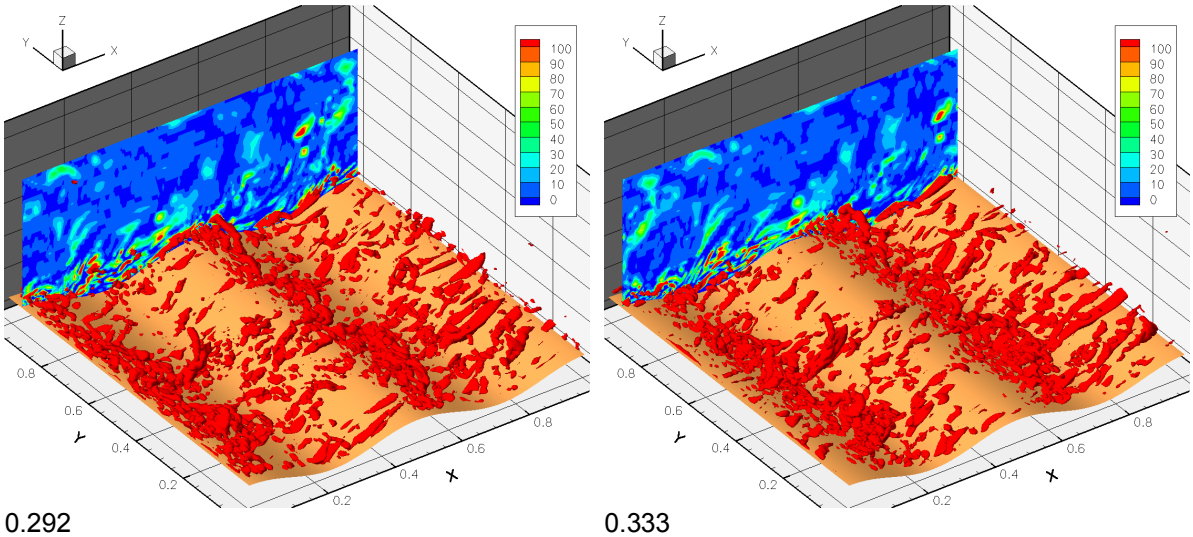

Figure 5.27: Evolution of coherent structures with time: Re 42, Q isosurface (non-averaged data, Q=150 s^{-2}). See text for further details.

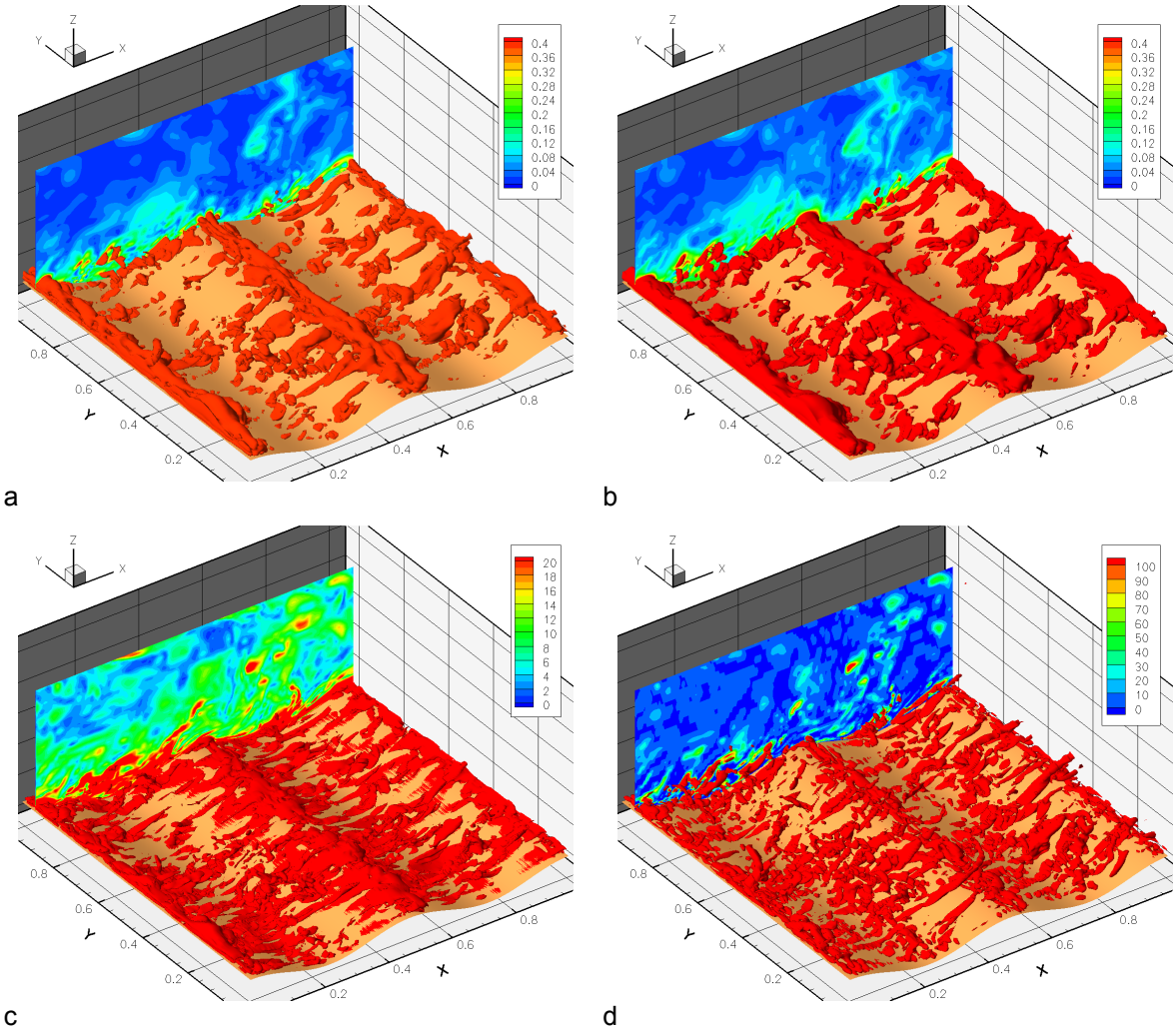

Figure 5.28: Comparison between different methods for Re 42 (non-averaged data, phase t=0.167 s). a) Cross pressure gradient, 0.04 Pam^{-1} isosurface. b) Pressure gradient magnitude, 0.045 Pam^{-1} isosurface. c) Vorticity magnitude, 50 s^{-1} isosurface. d) Q values, 200 s^{-2} isosurface. See text for further details.

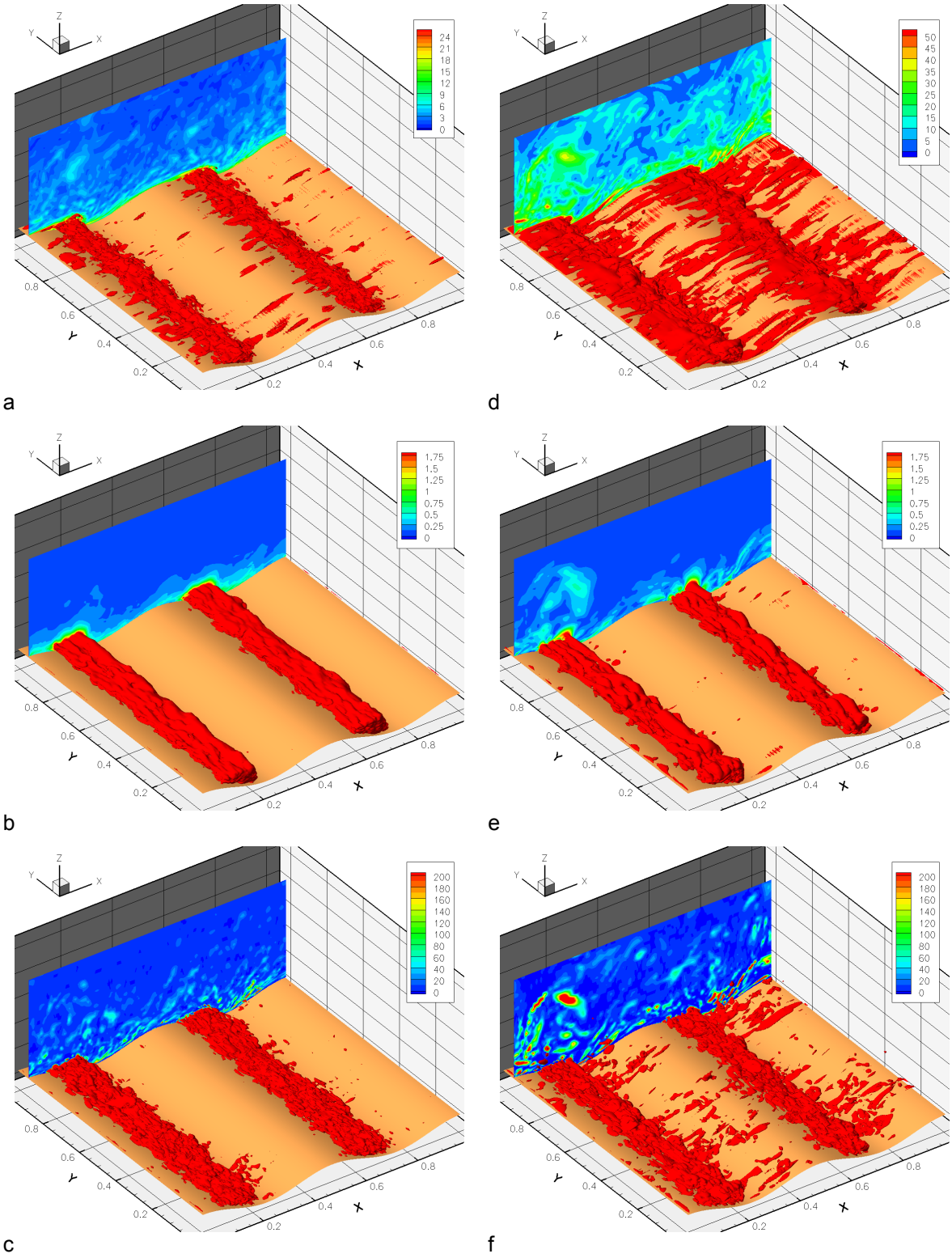

Figure 5.29: Comparison between the averaged and instantaneous three-dimensional distribution, Re 150. a) Phase-averaged Vorticity Magnitude (10 cycles, 30 s^{-1} isosurface). b) Phase-averaged Cross

Pressure Gradient (10 cycles, 2 Pam^{-1} isosurface). c) Phase-averaged Q (10 cycles, 450 s^{-2} isosurface) d) Non-averaged Vorticity Magnitude (85 s^{-1} isosurface). e) Non-averaged Cross Pressure Gradient (1 cycle, 2 Pam^{-1} isosurface). f) Non-averaged Q (1 cycles, 550 s^{-2} isosurface). See main text for further details.

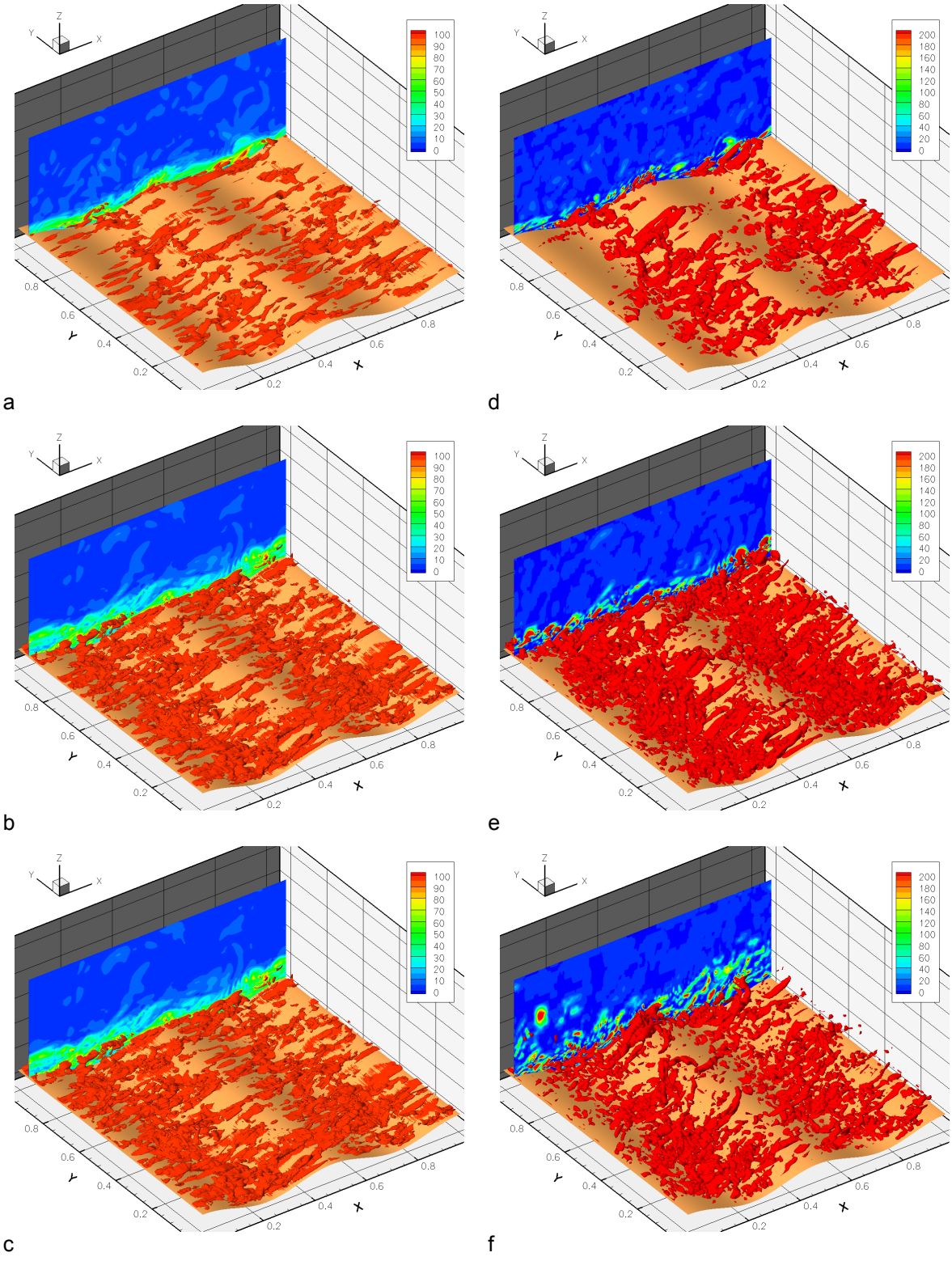

Figure 5.30: Coherent structures' field evolution as described by the vorticity and Q isosurfaces, Re 210. a-c) Vorticity magnitude isosurfaces (non-averaged data, 100 s^{-1} isosurface); phase t=2, 3 and 4 s

respectively. d-f) Q isosurfaces (non-averaged data, 550 s^{-2} isosurface); phase t=2, 3 and 4 s respectively. See main text for further details.

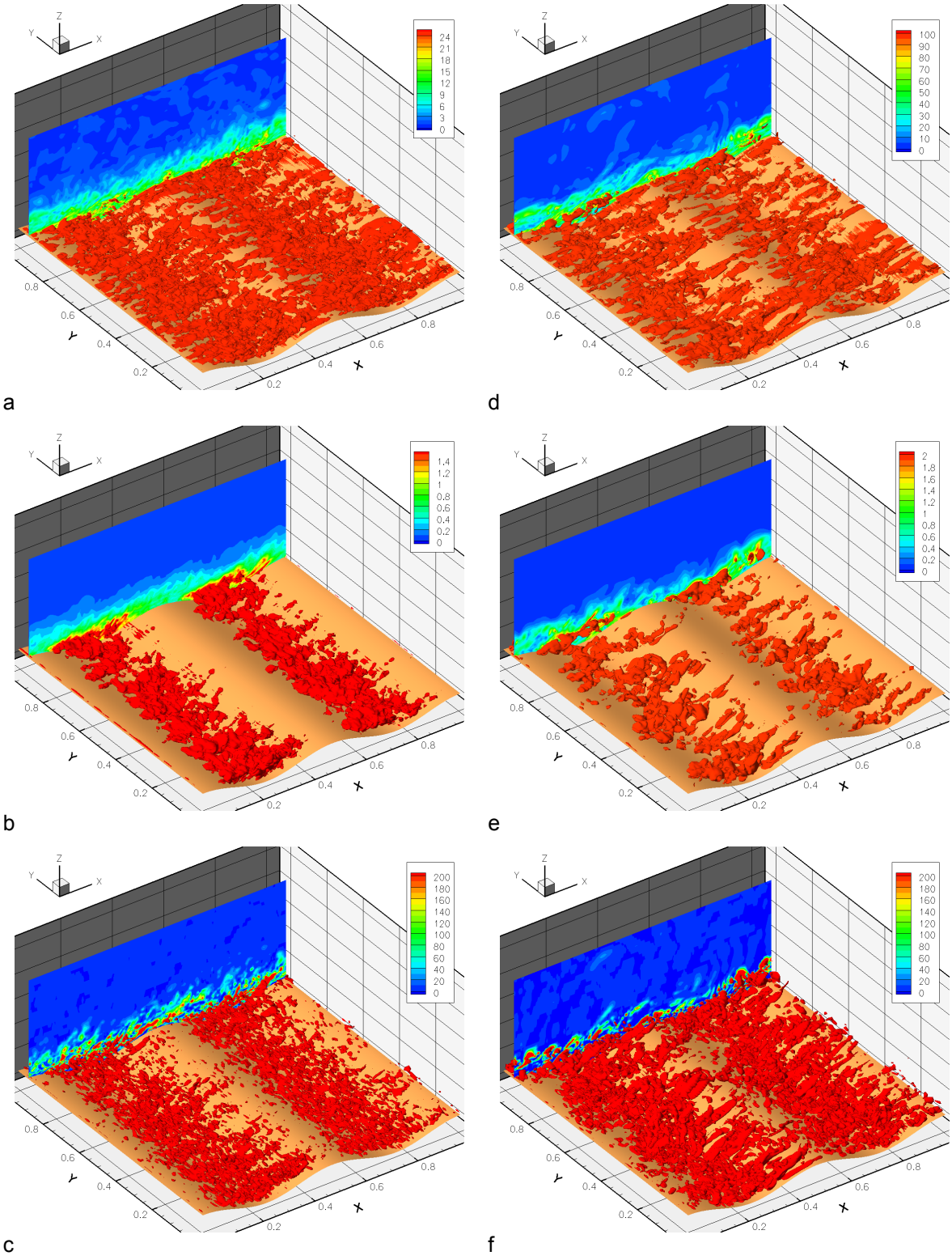

Figure 5.31: Phase-averaged and instantaneous distribution of coherent structures described by several

methods, Re 210, phase t=3 s. a) Averaged vorticity magnitude isosurfaces (10 cycles, $|\boldsymbol{\omega}|=25\,s^{-1}$). b) Averaged pressure gradient magnitude (10 cycles, $|\nabla p|=1.75\,Pa\,m^{-1}$). c) Averaged Q (10 cycles, Q = 550 s^{-2}). d) Non-averaged vorticity magnitude isosurfaces ($|\boldsymbol{\omega}|=60\,s^{-1}$) . e) Non-averaged pressure gradient magnitude isosurfaces ($|\nabla p|=2\,Pa\,m^{-1}$). c) Non-averaged Q isosurfaces (Q = 550 s^{-2}).

REFERENCES

Anonymous, 2003 "Tecplot® user's manual", Amtec Engineering, Inc., Bellevue, Washington, 628 pages

Aris, R., 1962, “Vectors, tensors, and the basic equations of fluid mechanics”, Dover Publications Inc., New York, 286 pages

Balaras, E. et al, 2001, “Self-similar states in turbulent mixing layers”, J. Fluid Mech., vol. 446, pp. 1-24

Banks, D.C. and Singer, B. A. undated “Vortex tubes in turbulent flows: identification, representation, reconstruction” U.M. 14 pages

Barr, B.C. et al 2004 “Numerical simulation of turbulent, oscillatory flow over sand ripples”, J. Geoph. Res., vol. 109, C09009, 19 pages

Belcher, S.E. and Hunt, J.C.R. 1998 “Turbulent flow over hills and waves”, Ann. Rev. Fluid Mech., vol. 30, 507-538

Blackman, R.B. and Tukey, J.W. 1959 "The measurement of power spectra", Dover Publications Inc., New York, 190 pages.

Blondeaux, P. et al 2004 “Coherent structures in an oscillatory separated flow: numerical experiments”,J. Fluid Mech., vol. 518, pp. 215-229

Cantwell, B.J. 1981 “Organized motion in turbulent flow”, Ann. Rev. Fluid Mech., vol. 13, pp. 457-515

Carlier, J. and Stanislas, M. 2005 "Experimental study of eddy structures in a turbulent boundary layer using particle image velocimetry", J. Fluid Mech., vol. 535, pp. 143-188

Chang, Y.S. and Scotti, A. ,undated manuscript, “Numerical simulation of sediment particles released at the edge of the viscous sublayer in steady and oscillating turbulent boundary layers”, submitted to Phys. of Fluids

Chang, Y.S. and Scotti, A. , 2003 “Entrainment and suspension of sediments into a turbulent flow over ripples”, J. of Turb., vol. 4:1, pp. 1 - 22

Chang,Y.S. and Scotti, A. 2004 “Modeling unsteady turbulent flow over ripples: RANS versus LES” , JGR, vol. 109, C09012

Chen, H. et al 2003 "Extended Boltzmann kinetic equation for turbulent flows", Science, vol. 301, pp. 633-636

Chernyshenko, S.I. and Baig, M.F. 2005 “The mechanisms of streak formation in near-wall turbulence”,J. Fluid Mech., vol. 544, pp. 99-131

Chong, M.S. et al, date unknown, “Invariants of the velocity gradient tensor in eddying motion and turbulence”, unpublished manuscript, 2 pages.

Delery, J.M. 2001 “Robert Legendre and Henri Werle: Toward the elucidation of three-dimensional separation”, Ann. Rev. Fluid Mech., vol. 33, pp. 129-154

Dronkers, J. 2005 "Dynamics of coastal systems", World Scientific, New Jersey, 519 pages

Dubieff, Y. and Delcayre, F. 2000 “On coherent-vortex identification in turbulence”, Journ. Turb., vol. 1, pp. 1-22

Guo, D. et al 2004 “Flow feature extraction in oceanographic visualization” Proc. Comp. Graph. Int., 1530-1052/04, 12 pages

Haller, G. 2005 “An objective definition of a vortex”,J. Fluid Mech., vol. 525, pp. 1-26

Hanes, D.M. et al 2001 "Wave-formed sand ripples at Duck, North Carolina", J. Geoph. Res., vol. 106, C10, pp. 22575-22592

Henn, D.S. and Sykes, R.I., 1999, “LES of flow over wavy surfaces”, Journ. Fluid. Mech., vol. 383, pp. 75-112

Holmes, P. et al 1996 "Turbulence, coherent structures, dynamical systems and symmetry", Cambridge University Press, Cambridge, 420 pages.

Jeong, J. and Hussain, F. 1995 “On the identification of a vortex”, J. Fluid Mech., vol.285, pp. 69-94

Jiang, M. et al undated “Geometric verification of swirling features in flow fields”, U.M., 8 pages

Jimenez, J. et al 1988 "Ejection mechanisms in the sublayer of a turbulent channel", Phys. Fluids, vol.31, pp. 1311-1313.

Kim, J. 1985 "Turbulence structures associated with the bursting event", Phys. Fluids, vol.28, pp. 52-58.

Kundu, P.K. and Cohen, I.M. 1990 “Fluid mechanics”, Academic Press, San Diego, 730 pages

Marani, P.C. 2003 "Leonardo da Vinci", Harry N. Abrams, Inc., New York, 384 pages.

Marchioli, C. et al 2006 “Mechanisms for deposition and resuspension of heavy particles in turbulent flow over wavy interfaces”, Phys. Fluids, vol. 18, 025102

Moffatt, H.K. 1992 “Helicity in laminar and turbulent flow”, Ann. Rev. Fluid Mech., vol. 24, pp. 281-312

Nakagawa, S. and Hanratty, T.J. 2003 “Influence of a wavy boundary on turbulence. I. Highly rough surface”, Exp. Fluids, vol. 35, pp. 422-436

Nakagawa, S. and Hanratty, T.J. 2003 “Influence of a wavy boundary on turbulence. II. Intermediate roughened and hydraulically smooth surfaces”, Exp. Fluids, vol. 35, pp. 437-447

Natrajan, V. K. and Christensen, K. T. 2006 “The role of coherent structures in subgrid-scale energy transfer within the log layer of turbulence”,Phys. Fluids, vol.18, 065104-14 pages.

Piomelli, U. et al 2001 “LES of turbulent flows, from desktop to supercomputer”, VECPAR 2000, pp. 551-577

Reed, H.L. and Saric, W.S. 1989 "Stability of three-dimensional boundary layers", Ann. Rev. Fluid Mech., vol. 21, pp. 235-284

Robinson, S.K. 1991 "Coherent motions in the turbulent boundary layer", Ann. Rev. Fluid Mech., vol. 23, pp. 601-639

Roth, M. and Peikert, M. 1988 "A higher-order method for finding vortex core lines", Proceedings of the IEEE Visualization, pp. 143-150

Scotti, A. and Piomelli, U. 2001 “Numerical simulation of pulsating turbulent channel flow”, Phys. Fluids, vol.13, num. 5, 1367-1384

Scotti, A. 2007 Personal Communication.

Stegmaier, S. et al 2005 “Opening the can of worms: an exploration tool for vortical flows”, Proceedings of IEEE Visualization 2005 Conference, pp. 463-470

Stokes, G.G. 1901, “On the effect of internal friction of fluids on the motion of pendulums” in “Mathematical and Physical Papers by Sir George Gabriel Stokes”, vol. 3, Cambridge University Press, London, 423 pages.

Swearingen, J.D. and Blackwelder, R.F. 1987 "The growth and breakdown of streamwise vortices in the presence of a wall", J. Fluid Mech., vol.182, pp. 255-290

Tseng, Y-H. and Ferziger, J.H. 2004 “LES of turbulent wavy boundary flow – illustration of vortex dynamics”, J. of Turb., vol. 5, 23 pages.

Tufo, H.M. et al 1999 “Numerical simulation and immersive visualization of hairpin vortices”, Proceedings of the ACM/IEEE SC99 Conference, 15 pages.